

UNIVERSIDAD DE VALPARAÍSO

PHD THESIS

---

Probing the source structure in lensed  
AGNs

---

Author:

Alejandra MELO MELO

Supervisor:

Verónica MOTTA CIFUENTES

*A thesis submitted in fulfilment of the requirements  
for the degree of Ph.D. in Astrophysics*

*in the*

INSTITUTO DE FÍSICA Y ASTRONOMÍA

April 2022



©2022, Alejandra Melo Melo

Se autoriza la reproducción total o parcial, con fines académicos, por cualquier medio o procedimiento, incluyendo la cita bibliográfica del documento.

# Acknowledgements

*One, remember to look up at the stars and not down at your feet. Two, never give up work. Work gives you meaning and purpose and life is empty without it. Three, if you are lucky enough to find love, remember it is there and don't throw it away.*  
- Stephen Hawking

Quiero agradecer en primer lugar a mi supervisora, la Dr. Verónica Motta. Sin ella, ni su ayuda, consejos y motivación en todos estos años no hubiese podido llegar hasta este punto.

También agradecer a los académicos que me enseñaron las herramientas para el mundo del astrofísico. En especial quiero hacer mención a Julián Mejía-Restrepo, Roberto Assef, y Evencio Mediavilla. Me acompañaron durante años y me ayudaron en mi formación. Agradezco también a parte de mi comité que me ayudó en mejorar mi tesis escrita, a Timo Anguita y Eduardo Ibar.

A mi familia que han estado conmigo desde el inicio, en las buenas y en las malas, y que me aguantaron mis mañanas, mis noches de estudio y mis fines de semana de trabajo.

A mis amigos, los de siempre, los que me acompañaron desde el inicio y los que llegaron en el camino. No los nombraré, pero todos ustedes saben quienes son. Gracias por ser mi familia porteña, por las noches de salidas, aguantarme que siempre cantara Bohemian Rhapsody en los karaokes, las tardes en la playa, mis noches de bajón con Tame Impala e Imagine Dragons, y por darle felicidad a mis días.

Finalmente, agradezco a quienes financiaron este trabajo, becas de doctorado CONICYT (ANID) PFCHA/Doctorado Nacional/2017 folio 21171499, gastos operacionales (Folio : 24190202) y a PUENTE, UVA20993 del Instituto de Física y Astronomía de la Universidad de Valparaíso.

Nos volveremos a encontrar en algún lugar del mundo (:

# Contents

Declaration of Authorship	i
Acknowledgements	ii
Contents	iii
Abstract	v
Abbreviations	vi
<b>1 Introduction</b>	<b>1</b>
1.1 Active Galactic Nuclei	2
1.1.1 Supermassive black hole	5
1.1.2 SMBH and host galaxy co-evolution	7
1.2 Gravitational lensing	9
1.2.1 Lens equation	10
1.2.2 Lens Models	14
1.2.2.1 Singular isothermal sphere (SIS)	14
1.2.2.2 Singular isothermal ellipsoid (SIE)	14
1.2.3 Magnification	15
1.2.4 Critical and caustic curves	16
1.2.5 Time delay	18
1.2.6 Microlensing	19
1.3 Supermassive black hole mass	21
1.4 Objectives	25
<b>2 Observation and data reduction</b>	<b>27</b>
2.1 Sample selection	27
2.2 Spectroscopic data	34
2.2.1 X-shooter data	34
2.2.1.1 One-dimensional extraction	38
2.2.1.2 Flux loss and luminosity estimations	40
2.2.2 LUCIFER data	41
2.2.3 MMIRS data	44
<b>3 Methods</b>	<b>45</b>
3.1 Gravitational lens model	45
3.2 Black hole mass (MBH)	47

3.2.1	Emission line fitting and luminosity measurement . . . . .	48
3.3	Microlensing analysis . . . . .	49
3.4	Accretion disk size estimation . . . . .	52
3.4.1	Chromatic microlensing . . . . .	52
<b>4</b>	<b>Results</b>	<b>55</b>
4.1	First black hole mass estimation for the quadruple lensed system WGD2038-4008	55
4.1.1	Line profiles comparison . . . . .	56
4.1.2	Line width estimation . . . . .	57
4.1.3	Microlensing analysis . . . . .	57
4.1.4	Luminosity and $M_{\text{BH}}$ measurement . . . . .	60
4.1.5	Conclusions . . . . .	61
4.2	Black Hole masses using $H\alpha$ and $H\beta$ lines of gravitational lensing quasars . .	64
4.2.1	$M_{\text{BH}}$ measurement . . . . .	66
4.2.2	Discussion . . . . .	70
4.2.3	Conclusion . . . . .	72
4.3	Black hole mass estimation using different emission lines for three double lensed quasars . . . . .	73
4.3.1	Data and line profiles . . . . .	74
4.3.1.1	LBQS1333+0113 . . . . .	74
4.3.1.2	Q1355-2257 . . . . .	76
4.3.1.3	QJ0158-4325 . . . . .	77
4.3.2	Microlensing Analysis . . . . .	81
4.3.3	Black hole mass measurement . . . . .	86
4.3.4	Accretion disk size estimation . . . . .	92
4.3.5	Conclusions . . . . .	94
<b>5</b>	<b>Conclusion</b>	<b>95</b>
5.0.1	Future work . . . . .	96
<b>A</b>	<b>Emission lines fitting parameters</b>	<b>97</b>
<b>B</b>	<b>X-shooter spectra</b>	<b>99</b>
<b>C</b>	<b>Probability density functions</b>	<b>101</b>
	<b>List of Figures</b>	<b>101</b>
	<b>List of Tables</b>	<b>107</b>
	<b>Bibliography</b>	<b>108</b>

---

Accurate determination of supermassive black hole masses are crucial to correctly understand the connection between supermassive black holes and their host galaxies, specially with the correlation that exists between the supermassive black hole mass and some physical parameters of the host galaxy. This connection is relatively well determined in the local universe over 4 orders of magnitude. However, at high redshifts ( $z > 1$ ), due to flux limitation it is challenging to determine the physical parameters of the faintest systems. Fortunately, gravitational lensed quasars are highly magnified, and thus offers the opportunity to study a fainter population that otherwise is not accessible.

In this work, I study the inner region of the lensed quasars. The mass of the black hole is determined using the single-epoch method for 15 lens systems using the Balmer lines ( $H\alpha$  and  $H\beta$ ). In addition, I present supermassive black hole mass for MgII and CIV, and compare them with the previous masses and also with the literature. For the first time the black hole mass was obtained for WGD2038-4008 (Melo et al. 2021) and QJ0158-4325 (Melo et al. in prep I). The luminosity range obtained for all the sample was  $44.1 \leq \log_{10}(L_{bol}/L_{sun}) \leq 47.6$ , which is in agreement with the correlation of  $L_{bol}$  vs  $M_{BH}$  of lensed and non-lensed AGNs.

In addition, chromatic microlensing was detected in three systems, which offered an alternative technique to measure the accretion disk size. Our estimations does not agree with the one obtained using the single epoch method.

Finally, I conclude that the new black hole masses reach a fainter and low-luminosity region in the black hole mass - luminosity plane.

---

# Abbreviations

<b>AGN</b>	Active galactic nuclei
<b>BLR</b>	Broad line region
$M_{BH}$	Black hole mass
<b>SMBH</b>	Supermassive black hole
<b>BEL</b>	Broad emission line
<b>NLR</b>	Narrow line region
<b>FWHM</b>	Full width at half maximum
<b>RM</b>	Reverberation mapping
<b>SE</b>	Single epoch
<b>ADC</b>	Atmospheric dispersion corrector
<b>OB</b>	Observing block
<b>PCA</b>	Principal component analysis
<b>S/N</b>	Signal-to-noise ratio
<b>LRT</b>	Low resolution templates
<b>SED</b>	Spectral energy distribution

# Chapter 1

## Introduction

Gravitational lensing is a powerful tool to study many astrophysical phenomena, from exoplanets, galaxies, dark matter and the structure of an active galactic nuclei (Treu et al. 2015, Suyu et al. 2018, Sluse et al. 2019). Active galactic nuclei (AGN) is a compact region in a center of a galaxy that has higher luminosity than a normal galaxy and emits in all the electromagnetic spectrum (Rees 1984, Eigenbrod 2011). Gravitational lensing acts as a natural telescope, allowing us to make progress in the study of the most far away and luminous objects in the Universe. The high flux magnification induced by gravitational lensing allows us to obtain spectra for sources that would be very time consuming to obtain, and to observe and study the inner structure of AGNs (e.g. Kochanek 2004, Wambsganss 2006, Sluse et al. 2012, Motta et al. 2012). It can help us to measure the black hole mass ( $M_{BH}$ ) of distant objects and study the coevolution between the growth of a supermassive black hole (SMBH) and its host galaxy (e.g. Ferrarese & Merritt 2000, Gültekin et al. 2009, Kormendy & Ho 2013, and therein).

In this chapter I will describe the structure of AGNs and their coevolution with its host galaxy. I will introduce a brief summary of the theory of gravitational lensing and some important parameters that will be used in the following chapters. In the next section I will define the microlensing effect and how it affects the  $M_{BH}$  measurement. Finally, I will detail the motivation and goals of this PhD thesis.

## 1.1 Active Galactic Nuclei

The study of Active Galactic Nuclei (hereafter AGNs) started at the beginning of the 20th century, when [Fath 1909](#) took observations of a “spiral nebulae” that showed emission and absorption lines. Three decades later, [Seyfert](#) started to investigate these objects and in [1943](#) published a paper showing optical observation of six galaxies with broad emission lines (BELs; emission lines that have widths of thousands of kilometers per second), also narrow emission lines, and in some cases both (see as an example [figure 1.1](#)), which now are called Seyfert galaxies. These emission lines are at present used extensively to identify AGNs (e.g. [Baldwin et al. 1981](#)). On the other hand, with the development of radio astronomy, bright radio sources were discovered (called radio galaxies), such as Cygnus A ([Baade & Minkowski 1954](#)), with point-like structure and optical spectra similar to the sources that [Seyfert](#) observed (e.g. [Bolton & Stanley 1948](#), [Hanbury Brown et al. 1952](#), [Matthews & Sandage 1963](#)), that have since then been classified as quasi-stellar radio sources (quasars). The discovery that quasars have a “fuzzy nebulae” around them just like the sources of [Seyfert](#)’s, suggest that these are at the centers of distant galaxies ([Matthews et al. 1964](#)). In [1963](#) [Schmidt](#) measured the redshift of the quasar 3C 273 and realized that it has a nuclear region 100 times brighter optically than the luminous galaxies identified with radio sources so far. Today, it is recognized that quasars and Seyfert are both the same phenomenon known as AGNs. Since then, the study of AGN has grown exponentially, specially with the discovery that they are powerful X-ray emitters (e.g. [Haardt & Maraschi 1991](#), [Colbert & Mushotzky 1999](#), [Ho 1999](#), [Fabbiano 2006](#), [Ho 2008](#)), unraveling a new frontier in the field of AGN research. The idea that there is matter accreting into the SMBH to explain the energy source and radiation was proposed in the 1960s (e.g. [Salpeter 1964](#), [Lynden-Bell 1969](#)), and two decades later [Rees 1984](#) suggested some physical processes and models that could explain how black holes might generate the power of AGNs, which have since then been under study (e.g. [Blandford & Rees 1992](#), [Kormendy & Richstone 1995](#), [Haehnelt et al. 1998](#), [Richstone et al. 1998](#), [Kormendy & Gebhardt 2001](#), and therein). The theory of the thin accretion disk by [Shakura & Sunyaev 1973](#) provided the basic working model for the inward accretion around the SMBH in an AGN that we still use today.

Many classes of active galaxies (galaxy hosting an AGN) has been identified, such as radio galaxies, quasars, blazars and Seyfert galaxies ([Urry 2004](#)). Since the beginning, many have tried to understand the nature of the difference that exists in the morphology of the AGNs,

---

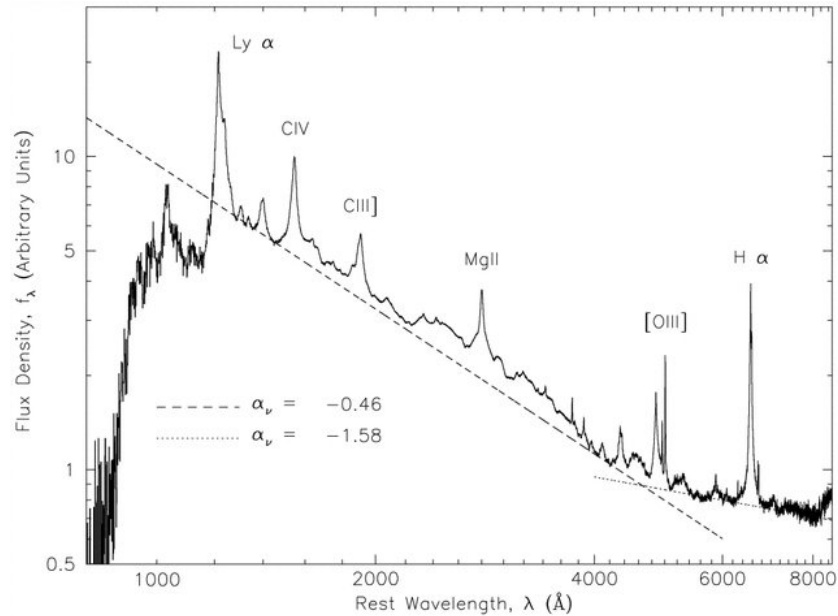


FIGURE 1.1: Composite quasar spectrum from [Vanden Berk et al. 2001](#). It shows the characteristic broad and narrow emission lines of quasars.

first in the radio band ([Fanaroff & Riley 1974](#)). But the difference was also noticed in the optical spectra of AGNs, that result in the broad and narrow lines classification we still use today ([Osterbrock 1977](#)). The idea that the different types of AGNs could be unified in one single model was proposed from optical spectropolarimetric observations (e.g. [Antonucci & Miller 1985](#)), which result in the model called the Unified Model of an AGN ([Antonucci 1993](#), [Urry & Padovani 1995](#)). The model includes (see Figure 1.2; [Netzer 2015](#)):

- a central SMBH: the primary energy source with mass range between  $10^6 < M_\odot < 10^9$  and ranges from  $10^{10} - 10^{15}$  cm (light-seconds to light-days) ([Eigenbrod 2011](#)).
- an accretion disk: optically thick and geometrically thin rotating disk where matter is accreted onto the SMBH ([Eigenbrod 2011](#)). Its high intrinsic luminosity arises from the thermal emission (with the innermost regions being the hottest) produced by the high accretion rate of material ( $1-10 M_\odot$ ) into the SMBH ([Carroll & Ostlie 2006](#)), responsible for the continuum emission in the spectra. The first image of a black hole and the accretion disk was published in 2019 by the [Event Horizon Telescope Collaboration et al.](#). The image showed a bright ring with a dark center, which is the black hole's shadow.
- High density dust clouds of dust-free gas (Broad Line Region, hence BLR) where the broad ( $\text{FWHM} > 1000 \text{ km s}^{-1}$ ) and optical/UV lines are produced by means of Doppler

broadening (see Fig. 1.1). Reverberation mapping (RM; a method where the BLR size is estimated measuring the time delay between the variation in the continuum of an AGN and the BLR response on the change of the incident flux) studies have shown that the inner radius of this region scales with luminosity and is around 10 – 100 light days (Kaspi et al. 2005).

- a optically and geometrically thick structure called the torus that extends from  $\sim 0.1$ -10 parsecs from the SMBH. The different types of AGNs can be explained by the view we have into them, and the torus can help differentiate between different classes (it can block the view of the continuum source and the BLR), making it one of the main focuses in the Unified Model (Antonucci 1993, Eigenbrod 2011),
- low density and velocity ionized gas called the Narrow Line Region (NLR), which extends from the outside of the torus to hundreds of parsecs from the SMBH. This region is where the narrow ( $\text{FWHM} < 1000 \text{ km s}^{-1}$ ) permitted and forbidden (like [OIII]5007, [NII]6550,6585, [SII]4072,6718,6732) emission lines originate (Fig. 1.1).
- a central radio jet that spans at high velocity (often exceed  $1000 \text{ km s}^{-1}$ , Sturm et al. 2011, Zakamska et al. 2016) on both directions from the SMBH, perpendicular from the accretion disk. The energetic outflows and turbulences expands from  $\geq 0.1$  to  $> 10$  kpc (e.g. Liu et al. 2013, Ciccone et al. 2018, Davies et al. 2020).

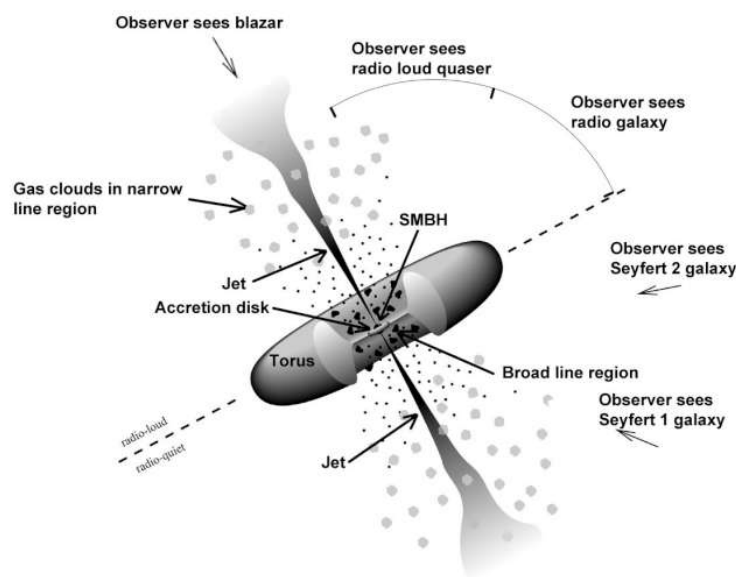


FIGURE 1.2: Scheme of an AGN adapted from Urry & Padovani 1995

The AGN unification model can explain the different classification of the observed AGN depending on the viewing angle (see Fig. 1.2). A very simplified classification is based on the radio-loud or radio-quiet, and the width of the emission lines (see [Urry & Padovani 1995](#)). Using their optical emission lines as a guide, they can be classified as broad line AGNs (type 1 AGNs) with broad emission lines (BELs), or as narrow-line AGNs (type 2 AGNs) with only narrow emission lines (NELs). This model can explain why the narrow emission lines (permitted and forbidden) are observed in most AGNs while the broad lines are not. The NELs are emitted from a larger spatial scale and can be observed at any orientation, while the BELs originate from smaller scales and, depending on the observer's orientation, they could be hidden by the obscuring torus. The quasars, of type 1 AGN, are among the brightest objects identified that present prominent broad and narrow lines in their spectra and time-variable continuum flux ([Schmidt 1963](#)). The variability in the continuum emission shows over a broad range of temporal frequencies, and the time scale can range from hours to years (e.g. [Arévalo et al. 2009](#), [Lira et al. 2011](#), [Edelson et al. 2015](#)). The variability in the inner regions of the AGNs are from the intrinsic emission from the central engine (i.e. UVB/optical radiation from the accretion disk; [Shakura & Sunyaev 1973](#), [Morgan et al. 2010](#)) and the X-ray emission from the hot corona (e.g. [Haardt & Maraschi 1991](#), [Sou et al. 2022](#)).

### 1.1.1 Supermassive black hole

After the discovery of quasars, it was suggested that SMBH may be used to describe their energy outputs ([Salpeter 1964](#), [Lynden-Bell 1969](#)), since no mechanism explained it. The work of accretion presented by [Shakura & Sunyaev 1973](#) and also [Shields 1978](#), produced spectra similar to those of quasars, confirming the mechanism of accretion into the SMBH for the observed energy outputs.

Even though astronomers have a pretty good idea of how most of the supermassive black holes form, it is still a difficult question to answer because of the large distance between us and their emission, which is difficult to disentangle with the emission of the host galaxy. A process is needed to be able to collapse huge amount of mass into their own gravity and form a black hole. Since the discussion of possible evolutionary tracks made by [Begelman & Rees 1978](#) in the formation of SMBH, many routes has been proposed: from the collapse of a large gas cloud ([Loeb & Rasio 1994](#)), or the collapse of early stars ([Volonteri & Rees 2005](#)). Even though there are unanswered questions surrounding the origin of the SMBHs, the research

---

into their observed properties can help us comprehend their evolution and, hopefully, their formation. The gravity of a black hole is so strong that even the light cannot escape from it, and the main property that we can study is its mass. Therefore, estimating the mass of the SMBH that is fueling an AGN is an indirect observational evidence for its existence and for investigating their origin (see [Peterson 2014](#)).

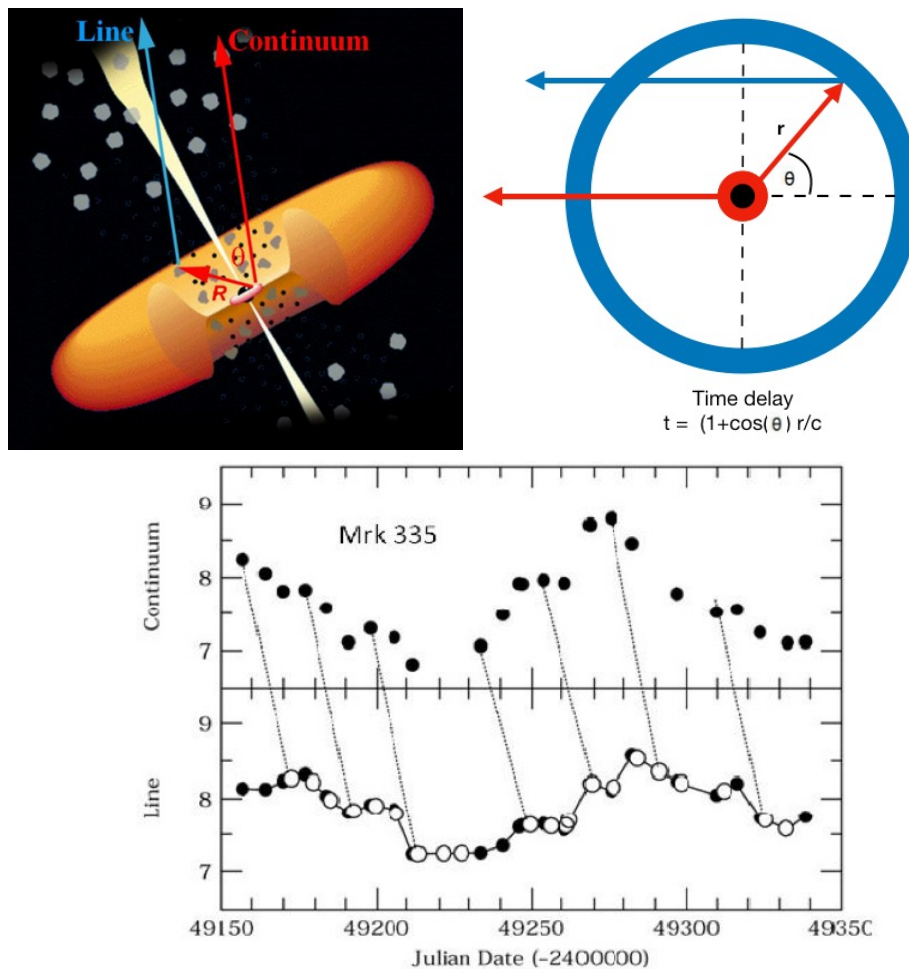


FIGURE 1.3: Representations of the reverberation mapping. Upper left: Scheme based on the AGN model of [Urry & Padovani 1995](#). The accretion disk emits the continuum radiation and the response in the BLR shown as emission lines. Upper right: The accretion disk is in red and the BLR is in blue. The figure shows the time delay between light which reaches us directly from the central continuum source (the red arrow) and the light which is emitted due to recombination in the BLR (the blue arrow). Lower image: Continuum and emission-line light curves for Mrk 335 from [Peterson 2001](#).

There are two main methods for estimating the  $M_{BH}$  that can be divided as direct and indirect. For nearby objects, the direct method derives the mass through the gravitational influence that the black hole has with the dynamics of stars and gas surrounding the SMBH. This requires stellar and gas dynamic modelling (e.g. [Kormendy & Richstone 1995](#), [Tremaine et al. 2002](#), [Davies et al. 2006](#), [Onken et al. 2007](#), [Hicks & Malkan 2008](#)). We need to rely

on indirect methods when the further away an objects is. It relies on the calibrations of the more accurate and direct methods, using their observables to scale the  $M_{BH}$ .

For type 1 AGNs, a direct method to obtain the  $M_{BH}$  is assuming that the BLR is in virial equilibrium as  $M_{BH} \sim R_{BLR}(\Delta v)^2/G$ , where  $R_{BLR}$  is the distance from the BLR to the SMBH,  $\Delta v$  is the Keplerian velocity and  $G$  is the gravitational constant. The width of the line reveals the gravitational potential at that radius, so the linewidth of an emission line can be used as a proxy to obtain the velocity and  $R_{BLR}$  can be estimated using the reverberation mapping technique (RM, e.g. [Blandford & McKee 1982](#), [Peterson 1993](#), [Peterson et al. 2004](#)). This measures the time delay between the continuum emission variation, that arises from the accretion disk around the BH, and the response of the emission lines in the BLR (see [fig. 1.3](#)). This time delay provides an estimate of the distance between the accretion disk and the BLR by means of the speed of light. Reliable  $M_{BH}$  has been measured using the RM method for  $\sim 65$  type 1 AGNs at low redshift ( $z < 0.3$ ) and with limited luminosity  $\lambda L_{\lambda}(5100\text{\AA}) < 10^{46}$  erg/sec ([Kaspi et al. 2000, 2005](#), [Bentz et al. 2009, 2013](#)) and just  $\sim 60$  high luminosity and high redshift ( $z \geq 0.3$ ) sources (e.g. [Kaspi et al. 2007](#), [Shen et al. 2016](#), [Grier et al. 2017](#), [Lira et al. 2018](#), [Hoormann et al. 2019](#), [Grier et al. 2019](#), [Kaspi et al. 2021](#)). Long systematic monitoring (in order of months to years) of objects is needed to adequately measure the  $R_{BLR}$ . Furthermore, the line response to continuum variation increases with the AGN luminosity and redshift due to cosmological time dilatation ([MacLeod et al. 2010](#)). The RM of high-redshift AGNs is quite challenging, and it must span a period of a decade or more with long-term observing facilities ([Kaspi et al. 2021](#)). In addition, due to the faintness of quasars, large telescope collecting areas are needed.

### 1.1.2 SMBH and host galaxy co-evolution

As  $M_{BH}$  estimates were available, it was discovered that they correlated with some properties of the host galaxy. It was found that the directly measured  $M_{BH}$  for the local AGNs followed the  $M_{BH}$  and stellar velocity dispersion relation of quiescent galaxies (non-AGN), i.e., the  $M_{BH} - \sigma_*$  relation (e.g. [Sahu et al. 2019](#), [Gebhardt et al. 2000](#), [Ferrarese et al. 2001](#)). This scaling relation suggested a coevolution of black holes and galaxies (e.g. [Ferrarese & Merritt 2000](#), [Gebhardt et al. 2000](#), [Häring & Rix 2004](#), [McConnell & Ma 2013](#)), motivating empirical efforts to constrain the origin of this scaling relations and their evolution ([Bower et al. 2006](#), [Croton et al. 2006](#), [Treu et al. 2007](#), [Woo et al. 2008](#), [Bennert et al. 2011](#), [Woo et al. 2015](#),

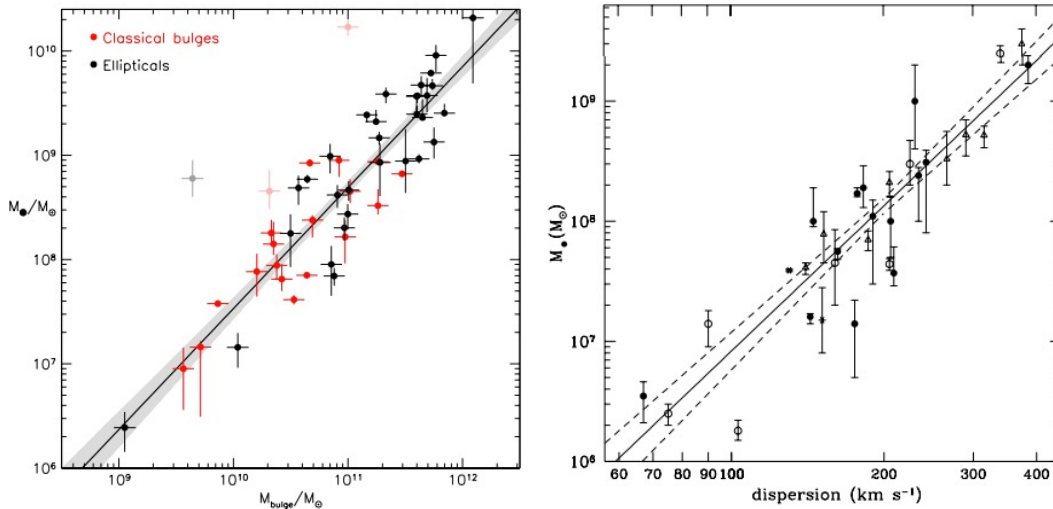


FIGURE 1.4:  $M_{BH}$  correlation with host galaxy parameters. Left:  $M_{BH}$  vs mass of the bulge from [Kormendy & Ho 2013](#). The authors distinguish classical bulges, but they are indistinguishable from elliptical galaxies, except that they are embedded in disks ([Renzini 1999](#)). Right:  $M_{BH}$  vs velocity dispersion from [Tremaine et al. 2002](#).

[DeGraf et al. 2015](#), [Batiste et al. 2017](#)). Galaxies hosting an AGN also follows the  $M_{BH} - \sigma_*$  relation (e.g. [Woo et al. 2010](#), [Park et al. 2012](#), [Woo et al. 2013](#), [Matsuoka et al. 2013](#), [Grier et al. 2013](#), [Bongiorno et al. 2014](#), [Park et al. 2015](#), [Bennert et al. 2015](#), [Ding et al. 2017a](#)), demonstrating that, present-day galaxies have a similar scaling relation as AGNs. In general, physical parameters of the SMBH seem to correlate well with the mass of the bulge, i.e.  $M_{BH} - M_{stellar}$  relation (e.g. [Kormendy & Richstone 1995](#), [Magorrian et al. 1998](#), [Gültekin et al. 2009](#), [Kormendy & Ho 2013](#), [Schulze & Wisotzki 2010](#)), luminosity, i.e.  $M_{BH} - L$  relation ([Marconi & Hunt 2003](#), [Lauer et al. 2007](#), [Graham 2007](#), [Kormendy & Bender 2009](#)) and velocity dispersion ([Ferrarese & Merritt 2000](#), [Tremaine et al. 2002](#)) of the host galaxy (see Fig. 1.4). The existence of this tight correlations are considered a result of the relation between the SMBH growth and galaxy evolution and the origin is still an open question ([Ferrarese & Ford 2005](#), [Kormendy & Ho 2013](#), [Ding et al. 2017a](#))

Moreover, it is accepted that the growth of AGNs and the star-formations history have a very similar evolutionary behaviour over cosmic time (see e.g. [Madau et al. 1996](#), [Ueda et al. 2003](#), [Hopkins et al. 2007](#), [Aird et al. 2015](#)), and that there is a connection between the nuclear activity and star formation. The nature of the coevolution is debated with two main scenarios. Some propose to be a result of galaxy mergers (e.g. [Di Matteo et al. 2005](#), [Hopkins et al. 2008](#)), while others to be SMBH feedback mechanisms that couple the black hole growth with that of the host galaxy (e.g. [Silk & Rees 1998](#), [Fabian 1999](#), [King 2003](#), [King & Pounds 2015](#)).

By measuring the reliable black hole mass for a sample of high-redshift quasars, it could help us understand this co-evolution between the SMBH and its host galaxy. To reach into these high-redshift quasars, we can take advantage of gravitational lenses.

## 1.2 Gravitational lensing

Gravitational lensing occurs when a gravitational field around a massive object deflects the light from a distant source, that can produce what is called “strong lensing”, i.e. the deflection (by galaxies or cluster of galaxies) is strong enough to produce multiple images of the distant source (e.g. left image of figure 1.5; [Schneider et al. 1992](#), [Treu 2010](#)). The first observation of the deflection of light was in May 1919, during a total solar eclipse ([Eddington 1919](#), [Dyson et al. 1920](#)), when the light deflection by the Sun’s gravitational field was confirmed. They compared in the same location the photographed positions of the stars during the total solar eclipse with those of the same stars photographed in July 1919, when the sun was far from that region in the sky. This confirmed the predictions of [Einstein’s](#) theory of general relativity: that gravity bends light. The first gravitational lens discovered was in 1979, when two quasars were discovered very close together with the same distance and spectra. This was the first double system Q0957+561 ([Walsh et al. 1979](#)). It was followed by the discovery of the first quadruple lensed quasar PG1115+080 in 1980 ([Weymann et al. 1980](#)), and the first gravitational lens that showed an Einstein ring (MG1131+0456; [Hewitt et al. 1988](#)).

Since then, the discovery of gravitational lenses QSOs has grown exponentially thanks to surveys searching for these systems. The first ongoing project CfA-Arizona Space Telescope LEns Survey: CASTLES ([Falco et al. 2001](#)), began in the late 1990s to catalog and discover new gravitational lenses<sup>1</sup>. CASTLES has ~100 lensing galaxies in its catalogue. More recently, the number has doubled by the STRong lensing Insights into the Dark Energy Survey (STRIDES; [Treu et al. 2015](#)), finding gravitational lensed quasars in the Dark Energy Survey ([Anguita et al. 2018](#), [Treu et al. 2018](#), [Lemon et al. 2020](#)), *Gaia* ([Lemon et al. 2018, 2019](#)), among others. Nowadays, more than 200 lensed quasars have been discovered (see the Gravitational Lensed Quasar Database<sup>2</sup>), specially with the help of new identification

---

<sup>1</sup><https://lweb.cfa.harvard.edu/castles/>

<sup>2</sup><https://research.ast.cam.ac.uk/lensedquasars/index.html>

techniques, such as machine learning, in large-area sky surveys (e.g. [Agnello et al. 2018](#), [Anguita et al. 2018](#), [Krone-Martins et al. 2019](#), [Lemon et al. 2020](#)).

Strong lensing magnifies the light from a distant source, increasing their observed flux and spatial resolution, allowing the study of objects that would otherwise be inaccessible. Lensed quasars have numerous advantages, including access to the high redshift Universe (e.g. [Wambsganss 1998](#), [Claeskens & Surdej 2002](#), [Courbin et al. 2002](#), [Bartelmann 2010](#)), study their inner structure of the AGN (e.g. [Pooley et al. 2007](#), [Bate et al. 2008](#), [Minezaki et al. 2009](#), [Dai et al. 2010](#), [Blackburne et al. 2011](#), [Mediavilla et al. 2011](#), [Mosquera et al. 2011](#), [Motta et al. 2012](#), [Sluse et al. 2012](#), [Guerras et al. 2013](#), [Hainline et al. 2013](#), [Jiménez-Vicente et al. 2014](#), [Rojas et al. 2014](#), [Muñoz et al. 2016](#), [Motta et al. 2017](#), [Fian et al. 2018](#), [Morgan et al. 2018](#), [Cornachione et al. 2020](#), [Mediavilla et al. 2020](#), [Rojas et al. 2020](#), [Chan et al. 2021](#), [Fian et al. 2021](#), [Hutsemékers & Sluse 2021](#), [Paic et al. 2022](#)), determine the time delay (a time lag that separates the light arrival of multiple images) and obtain cosmological information (e.g. [Kochanek 2004](#), [Kochanek & Schechter 2004](#), [Wambsganss et al. 2004](#), [Treu et al. 2013](#), [Bonvin et al. 2017](#), [Suyu et al. 2017](#)), the Hubble constant (e.g. [Falco et al. 1997](#), [Bonvin et al. 2017](#), [Courbin et al. 2018](#), [Suyu et al. 2018](#), [Birrer et al. 2019](#), [Bonvin et al. 2019](#), [Chen et al. 2019](#), [Millon et al. 2020a](#), [Rusu et al. 2020](#), [Shajib et al. 2020](#)), study the dark matter and luminous components of a lens galaxy (e.g. [Kochanek et al. 2001](#), [Oguri et al. 2002](#), [Jiménez-Vicente et al. 2015](#), [Jiménez-Vicente & Mediavilla 2019](#), [Nierenberg et al. 2020](#)), cosmological constraints (e.g. [Schneider et al. 1992](#), [Birrer & Treu 2021](#), [Nadler et al. 2021](#), [Abbott et al. 2022](#)), among others.

### 1.2.1 Lens equation

To derive the lens equation, it is assumed that the distances between the source, the lens, and the observer are usually much larger than the size of the lens galaxy, and that the light deflection occurs in a plane (known as the *thin lens approximation*). Figure 1.5 shows a scheme where an observer sees the light from a source (blue circle) at redshift  $z_s$  (or angular diameter distance  $D_s$ ) that is deflected by a lens (black circle) at redshift  $z_l$  corresponding to an angular diameter distance  $D_d$ , and cross the lens plane at a distance  $\xi$  (impact parameter).  $D_{ds}$  is the angular diameter distance between the lens and the source. The optical axis, indicated by the black line, is defined by the observed and the lens, and perpendicular to this axis we define the lens and source planes. Considering small angles, the dimensional

---

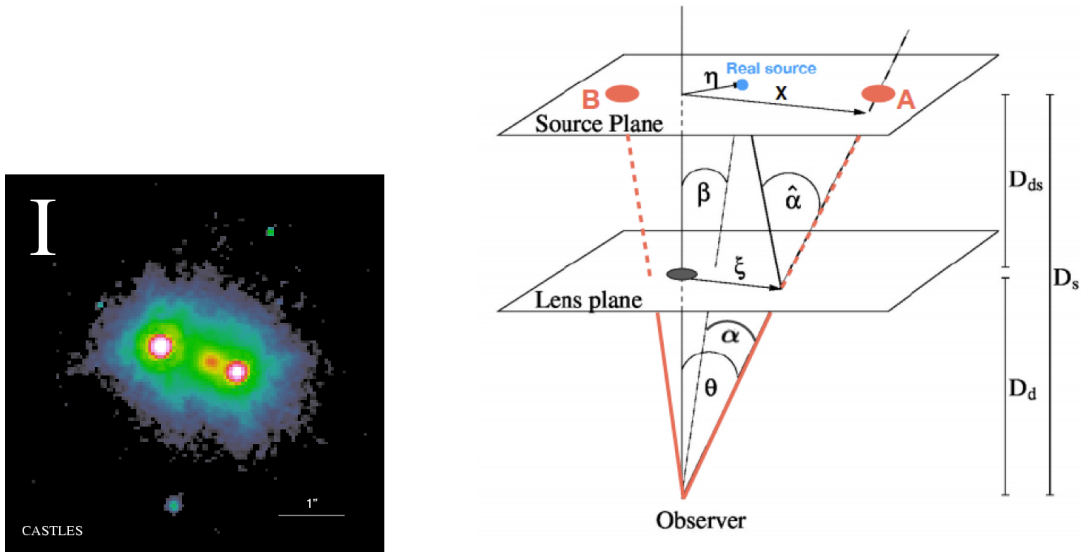


FIGURE 1.5: Gravitational lensing examples. Left: Double lensed quasar QJ0158-4325 in filter i from CASTLES. Right: Modified scheme of a gravitational lensing configuration taken from [Schneider 2006](#).

angular position of the images with respect to the optical axis (in angular coordinates) is  $\theta = \xi/D_d$ . The real dimensional angular position of the source is  $\beta = \eta/D_s$ , where  $\eta$  is the true position of the source in the source plane.

General relativity ([Einstein 1905](#)) predicts that a light ray from a source that passes at a minimum distance  $\xi$  of an spherical object of mass  $M$  (black circle in fig. 1.5 right), is going to be deflected  $\hat{\alpha}$ :

$$\hat{\alpha}(\xi) = \frac{4GM(\xi)}{c^2\xi}, \quad (1.1)$$

where  $M(\xi)$  is the mass inside a radius  $\xi$ ,  $G$  is the gravitational constant, and  $c$  the light velocity. The condition for the ray to reach the observer is going to be related as:

$$\theta D_s = \beta D_s + \hat{\alpha} D_{ds} \quad (1.2)$$

or,

$$\theta = \beta + \hat{\alpha} \frac{D_{ds}}{D_s} \quad (1.3)$$

Defining the reduced deflection angle  $\alpha(\theta)$ , that is related to the mass distribution of the deflector, as  $\alpha(\theta) \equiv \hat{\alpha}(D_d\theta)D_{ds}/D_s$ , equation 1.3 can be written as the *lens equation*:

$$\beta = \theta - \alpha(\theta) \quad (1.4)$$

This equation relates the true position of the source ( $\beta$ ) to its lensed image positions ( $\theta$ ).

The reduced deflection angle can also be written as:

$$\alpha(\theta) = \frac{1}{\pi} \int_{\mathbf{R}^2} d^2\theta' \kappa(\theta') \frac{\theta - \theta'}{|\theta - \theta'|^2}, \quad (1.5)$$

where  $\kappa$  is the normalized surface mass density (or convergence):

$$\kappa(\theta) = \frac{\Sigma(D_d\theta)}{\Sigma_{crit}}, \quad (1.6)$$

with

$$\Sigma_{crit} = \frac{c^2}{4G\pi} \frac{D_s}{D_d D_{ds}}, \quad (1.7)$$

where  $\Sigma_{crit}$  is the critical surface mass density, if  $\Sigma \geq \Sigma_{crit}$  ( $\kappa > 1$ ), then multiple images of the source can be obtained.

If we consider a circularly symmetric lens with an arbitrary mass profile, we can reduce the light deflection to a one-dimensional problem. Thus, using eq. 1.4 along with eq. 1.1 and the reduced deflection angle, the lens equation will be:

$$\beta = \theta - \frac{D_{ds}}{D_s} \frac{4GM(\xi)}{c^2\xi}, \quad (1.8)$$

applying  $\xi = \theta D_d$ , eq. 1.8 becomes:

$$\beta(\theta) = \theta - \frac{D_{ds}}{D_d D_s} \frac{4GM(\theta)}{c^2\theta}. \quad (1.9)$$

For a perfectly aligned source ( $\beta = 0$ ) the lensed images correspond to a symmetric image (known as the Einstein ring) and is found by setting  $\beta = 0$  in eq. 1.9 and solving for  $\theta$ :

$$\theta_E = \sqrt{\frac{4GM(\theta)}{c^2} \frac{D_{ds}}{D_d D_s}}, \quad (1.10)$$

where  $\theta_E$  is the Einstein radius, used as a reference to the angular scale in a lens system, and  $M(\theta)$  the mass enclosed at some angular radius  $\theta$ .

The lens equation (eq. 1.9) can be written using the Einstein radius as:

$$\beta = \theta - \frac{\theta_E^2}{\theta}. \quad (1.11)$$

If  $\beta < \theta_E$ , it will have two solutions, and the source images will appear at the positions:

$$\theta_{1,2} = \beta \pm \theta_E. \quad (1.12)$$

As mentioned before, in the case that  $\beta = 0$  and a perfect alignment exist between the source, lens and the observer,  $\theta = \theta_E$  and an Einstein ring will be formed.

On the other hand, the angular diameter distances ( $D_{ds}$ ,  $D_d$  and  $D_s$ ) in equation 1.10 depend on the cosmological model. To calculate them, we first need to use a dimensionless function (following [Hogg 1999](#)):

$$E(z) = \sqrt{\Omega_m(1+z)^3 + \Omega_k(1+z)^2 + \Omega_\Lambda} \quad (1.13)$$

where  $z$  is the redshift of the source, the parameters are the matter density ( $\Omega_m$ ), curvature ( $\Omega_k$ ) and energy parameters ( $\Omega_\Lambda$ ) respectively ([Peebles 1993](#)). According to the  $\Lambda$ CDM ( $\Lambda$  cold dark matter),  $\Omega_m \approx 0.7$ ,  $\Omega_k \approx 0$  and  $\Omega_\Lambda \approx 0.3$ . The total line-of-sight comoving distance  $D_C$  is obtained by integrating these contributions:

$$D_C = D_H \int_0^z \frac{dz'}{E(z')} \quad (1.14)$$

where  $D_H$  (Hubble distance) is defined by  $D_H \equiv c/H_0 = 3000 \text{ h}^{-1} \text{ Mpc} = 9.26 \times 10^{25} \text{ h}^{-1} \text{ m}$ . The comoving distance between two sources separated in the sky by an angle and the transverse comoving distance  $D_M$  are related to the line of sight of the comoving distance ( $D_C$ ). Since we are considering  $\Omega_k \approx 0$ , then  $D_M = D_C$ .

Finally, the angular diameter distance is related to the transverse comoving distance:

$$D_A = \frac{D_M}{1+z} \quad (1.15)$$

In the case of gravitational lenses, we also need to obtain  $D_{ds}$ , thus we consider an angular diameter between two objects at redshift  $z_1$  and  $z_2$ :

$$D_{A12} = \frac{1}{1+z_2} \left[ D_{M2} \sqrt{1 + \Omega_k \frac{D_{M1}^2}{D_H^2}} - D_{M1} \sqrt{1 + \Omega_k \frac{D_{M2}^2}{D_H^2}} \right] \quad (1.16)$$

### 1.2.2 Lens Models

Since the position and shape of the source and the matter distribution of the lens are unknown in equation 1.4, a mass distribution must be assumed to reproduce the positions of the images. To do this, one first chooses a mass distribution and, through the lens mapping, one reproduces the observed positions of the images from a fit of the model parameters and also finds the position of the source. In this section I will describe two parametric models that are commonly used (Schneider et al. 1992, and references therein) for the mass distribution of the lens.

#### 1.2.2.1 Singular isothermal sphere (SIS)

The singular isothermal sphere is the simplest parameterization of the spatial distribution of matter. The density distribution is described as (Schneider et al. 1992):

$$\rho(r) = \frac{\sigma_v^2}{2\pi G} \frac{1}{r^2}, \quad (1.17)$$

where  $\sigma_v$  is the one-dimensional velocity dispersion of stars in the galaxy,  $G$  the gravitational constant and  $r$  the radius. The surface mass density (or projected mass along the line of sight onto the lens plane  $\Sigma(r) = \int \rho(r) dz$ ) is:

$$\Sigma(\xi) = \frac{\sigma_v^2}{2G} \frac{1}{\xi}, \quad (1.18)$$

where  $\xi$  the impact parameter that enclosed the matter distribution. Although at  $\xi = 0$   $\Sigma \rightarrow \infty$ , for large values of  $\xi$  it resembles well the matter distribution of galaxies.

#### 1.2.2.2 Singular isothermal ellipsoid (SIE)

This model (Kormann et al. 1994) considers an elliptical gravitational potential for the galaxy. The density distribution will be:

$$\rho(r) = \frac{\sigma_v^2}{2\pi G r_e^2}, \quad (1.19)$$

$r_e$  is  $r_e = r_x + r_y/q$ , and  $q$  is the projected axis ratio. The surface mass density of the SIE is:

$$\Sigma(\xi) = \frac{\sqrt{f} \sigma_v^2}{2G} \frac{1}{\sqrt{\xi_1^2 + f^2 \xi_2^2}}, \quad (1.20)$$

The symmetric model is obtained in the limiting case when  $f \rightarrow 1$ .

### 1.2.3 Magnification

In addition of the deflection of the light that causes multiple images, gravitational lensing can magnify and distort the images of the source. As a simple example, let's consider a

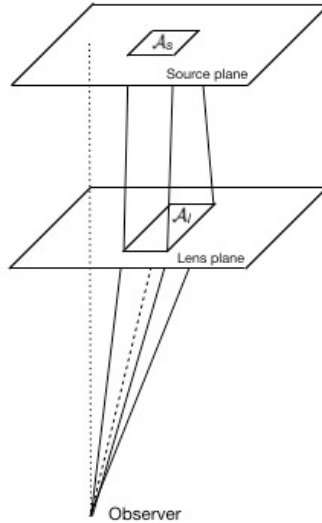


FIGURE 1.6: Distortion of a solid angle subtended by a source from [Schneider 2006](#).

scheme of this distortion in Figure 1.6. An observer sees the source as a solid angle that is distorted and magnified in the lens plane by a gravitational potential. According to Liouville's theorem, and considering that the light that comes from a source will not suffer emission or absorption in its path towards the observer, the surface brightness is conserved. Considering that the flux is obtained as the product between the surface brightness ( $I$ ) and the solid angle ( $F = \int d\Omega I$ ), the magnification is defined as:

$$\text{Magnification} = \frac{\text{Observed flux}}{\text{Intrinsic flux}} = \frac{I d\Omega_{\text{observed}}}{I d\Omega_{\text{intrinsic}}}$$

Considering the same notation as in Figure 1.5, we can rewrite the magnification ( $\mu$ ) as:

$$\mu = \frac{\theta d\theta}{\beta d\beta} \quad (1.21)$$

The distortion of the images can also be expressed by the Jacobian matrix of the lens equation:

$$\mathcal{A} = \frac{\partial \boldsymbol{\beta}}{\partial \boldsymbol{\theta}} = \begin{pmatrix} 1 - \kappa - \gamma_1 & -\gamma_2 \\ -\gamma_2 & 1 - \kappa + \gamma_1 \end{pmatrix}, \quad (1.22)$$

where  $\kappa$  is the convergence (equation 1.6), and  $\gamma_{1,2}$  the shear. The shear describes the properties of the tidal gravitational field and  $(\gamma_1, \gamma_2)$  are the components of the shear. In other words, the convergence magnify the image and the shear distort it. Figure 1.7 can gives us an example of this perturbations: in the presence of  $\kappa$  and  $\gamma$ , a circular source becomes an ellipse with mayor and minor axis of  $1 - \kappa - \gamma$  and  $1 - \kappa + \gamma$  respectively. The determinant of the Jacobi matrix can give us the magnification:

$$\mu = (\det \mathcal{A})^{-1} = \frac{1}{(1 - \kappa)^2 - \gamma^2}, \quad (1.23)$$

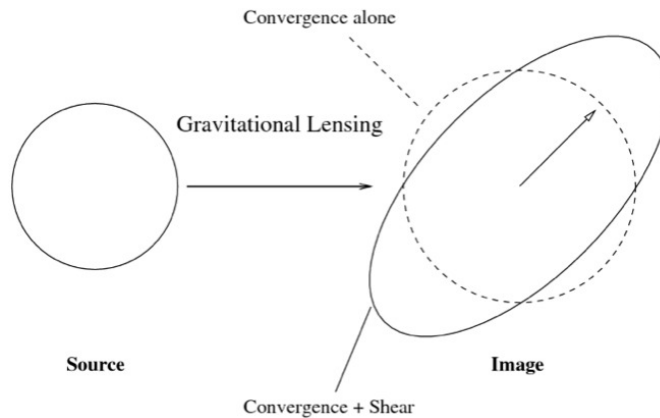


FIGURE 1.7: Figure from [Narayan & Bartelmann 1996](#) showing the effect that the convergence and shear have in a circular source.

#### 1.2.4 Critical and caustic curves

The critical and caustic curves are a key characteristic of the lens and allow us to understand qualitatively the geometry of the lens mapping. The magnification can have infinite values in some locations when  $\det \mathcal{A}=0$  (see eq. 1.23). The locations where the magnification is infinite are called the *critical curves* in the lens plane and the corresponding curves in the source plane are called *caustics* (see fig. 1.8). Although in theory the mag. could be infinit, in practice the images will be highly magnified when the source is near a caustic. Secondly, when

the source crosses the caustic, the number of images will change (Narayan & Bartelmann 1996).

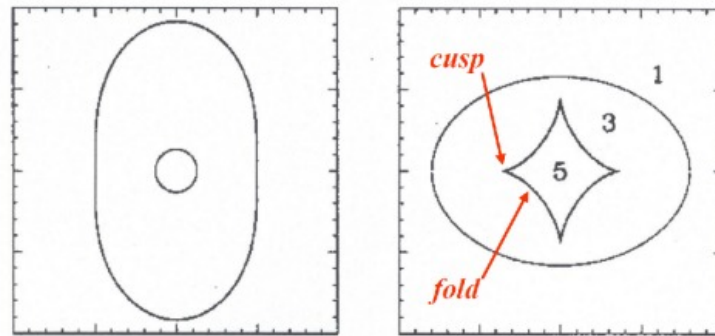


FIGURE 1.8: *Critical* (left) and *caustic* (right) curves for an elliptical lens. The numbers represent the regions in the source plane that correspond to 1, 3 or 5 images, respectively (Image from Wambsganss 1998).

An example is shown in figure 1.9 where the mass distribution is ellipse. The four smooth curves of the diamond *caustic* are called *folds* and the place where they join are the *cusp*. Different images configurations of gravitational lenses are formed depending on the relative position of the source with respect to the *caustic* curves. The multiple colors correspond to the different images configurations that are formed depending on the relative position of the source with respect to the *caustic* curves. When the source approaches the caustic, then the number of images increases and it will also be more distorted (Eigenbrod 2011). When a source is in the middle of the *caustic*, four aligned images are observed, known as the "Einstein cross" (red color in figure 1.9).

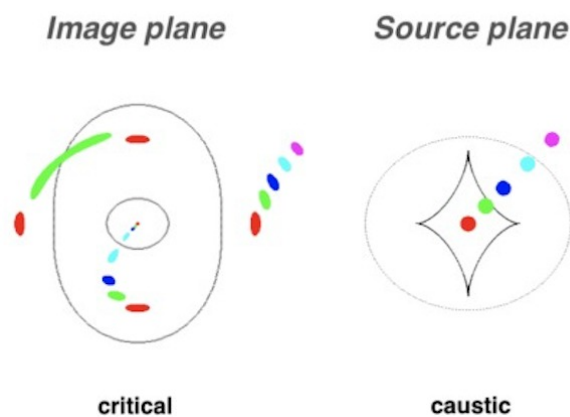


FIGURE 1.9: Strong lensing configuration for different alignments between a source and an elliptical lens. Image shows two configurations The different colors represent the source images and its respective images formed. Image from Zalesky & Ebeling 2020, credits from Narayan & Bartelmann 1996.

### 1.2.5 Time delay

Light rays from a source that are gravitationally lensed can arrive at different times along different paths to the observer. This time difference between the images is called a *time delay*, and the total time delay can be due to two reasons. The first one is due to geometrical time delay, in which the light rays take different paths as they are deflected by the lensing galaxy, that will result in different time travel. The second one is the gravitational time delay, which is an effect of general relativity called the Shapiro effect (Shapiro 1964). This effect is influenced by the gravitational field potential of the deflector and cause spacetime dilation, as consequence, a light ray that passes near this massive object will be slow down and will take a longer time to travel. The two contributions of time delay can be added together to derive an expression for the total time delay:

$$\Delta t(\boldsymbol{\theta}, \boldsymbol{\beta}) = \Delta t_{geom} + \Delta t_{grav} = \frac{1 + z_d}{c} \frac{D_d D_s}{D_{ds}} \left( \frac{1}{2} (\boldsymbol{\theta} - \boldsymbol{\beta})^2 - \psi(\boldsymbol{\theta}) \right), \quad (1.24)$$

where  $z_d$  is the redshift of the deflector, and  $D_d$ ,  $D_s$  and  $D_{ds}$  are the distances observer-deflector, observer-source, and deflector-source, respectively, and  $\psi(\boldsymbol{\theta})$  is the lens potential given by:

$$\psi(\boldsymbol{\theta}) = \frac{1}{\pi} \int_{R^2} d^2 \boldsymbol{\theta}' \kappa(\boldsymbol{\theta}') \ln |\boldsymbol{\theta} - \boldsymbol{\theta}'|. \quad (1.25)$$

Rewriting Equation 1.24 using the *time-delay distance* ( $D_{\Delta t}$ ) and the lens mass distribution:

$$\Delta t = \frac{D_{\Delta t}}{c} \Delta \phi \quad (1.26)$$

where  $c$  is the speed of light and  $\Delta \phi$  is the Fermat potential:

$$\Delta \phi = \frac{1}{2} (\boldsymbol{\theta} - \boldsymbol{\beta})^2 - \psi(\boldsymbol{\theta}), \quad (1.27)$$

which represent the transit time along all possible paths, not necessarily geodesic, between the source and the observer (Schneider et al. 1992, Perlick 2000, Petters et al. 2001, Frittelli et al. 2002).

The time-delay distance can be measured obtaining the time delay from light curves and modeling the lens mass distribution Refsdal 1964:

$$D_{\Delta t} \equiv (1 + z_d) \frac{D_d D_s}{D_{ds}}, \quad (1.28)$$

The time delay can be obtained by the photometric monitoring of point-like images (e.g. Fassnacht et al. 2002, Kochanek et al. 2006, Courbin et al. 2011, Eulaers et al. 2013, Tewes et al. 2013, Bonvin et al. 2017, Courbin et al. 2018, Bonvin et al. 2019, Millon et al. 2020a). For a variable source, like an AGN (e.g., Schechter et al. 1997, Fassnacht et al. 1999, Kochanek et al. 2006, Courbin et al. 2011), this changing in flux will be observed in each one of the images but with a time delay (Suyu et al. 2017). The light curves, or the variation in the light received over a period of time, will show us if intrinsic variation exists between the images (see fig. 1.10), and hence obtain the time difference between the images.

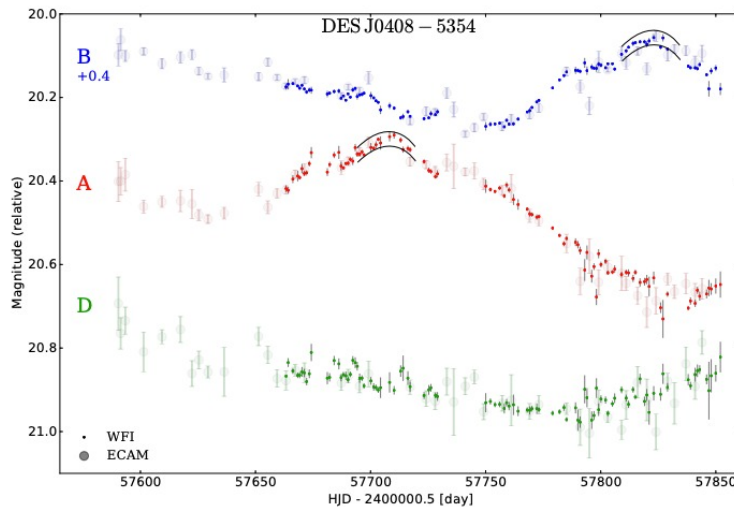


FIGURE 1.10: Light curves for DESJ0408-5354 presented in Courbin et al. 2018. The variability is observed in image A and B.

In addition, the time-delay distance is inversely proportional to the Hubble constant  $D_{\Delta t} \propto 1/H_0$ . Several groups have been using lensed quasars for measuring  $H_0$ . The COSMOGRAIL e.g., Bonvin et al. 2017, Courbin et al. 2011, Eigenbrod et al. 2005) has been an ongoing project to measure time delays of gravitational lenses, and in the last years those time delays were used to measure  $H_0$  (H0 Lenses in COSMOGRAIL’s Wellspring: HOLICOW; Suyu et al. 2017).

### 1.2.6 Microlensing

Just like galaxies, small compact objects (i.e. stars) in the lens galaxy can act as small lenses and introduce flux variations in the quasar images (the so-called microlensing effect, Chang & Refsdal 1979, Wambsganss 2006, and references therein). It produces “microimages” (see fig. 1.11) in which the angular separation is in the order of micro-arcseconds and

cannot be resolved with current telescopes. The “microimages” produce strong changes in the brightness of the lensed image of the quasar. This effect is transitory and it can have different duration depending on the relative motions among the source, the microlenses and the observer (see [Eigenbrod 2011](#), [Wambsganss 2006](#)).

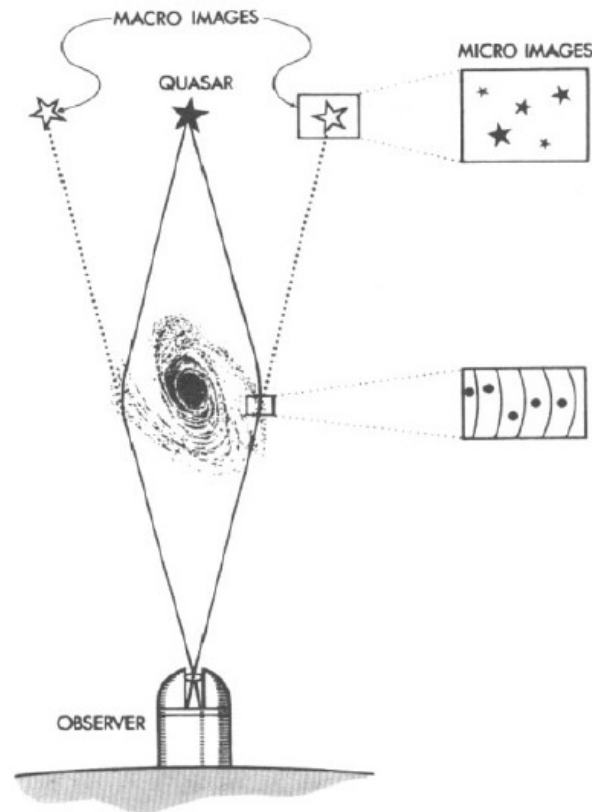


FIGURE 1.11: Microlensing effect due to gravitational lensing by individual stars. The image show the macromodel that split into microimages. Figure from [Refsdal & Surdej 1994](#).

Quasar microlensing can be detected by: observing light curves, analyzing the spectra and analyzing the BELs. The variations in the spectra or light curves of lensed quasars due to microlensing can be helpful in studying the inner structure of an AGN and constrain the sizes of the emission regions (e.g. [Abajas et al. 2002](#), [Popović et al. 2003](#), [Dai et al. 2004](#), [Popović & Chartas 2005](#), [Sluse et al. 2007](#), [Blackburne et al. 2011](#), [Donnarumma et al. 2011](#), [Mediavilla et al. 2011](#), [Chartas et al. 2012](#), [Motta et al. 2012](#), [Fian et al. 2016](#), [Krawczynski & Chartas 2017](#), [Fian et al. 2018](#)). In addition, spectra from different wavelength bands have been used to study microlensing using the magnitude difference between the continuum and the core of the emission line (e.g. [Mediavilla et al. 2009, 2011](#), [Motta et al. 2012](#)). The accretion disk and BLR can be affected by microlensing, but the NLR is insensitive to microlensing (it is in a farther out region from the black hole) and can be used as the baseline ([Abajas et al. 2002](#)).

Microlensing in the BLR is possible if its size is comparable to the Einstein radius of a star (Nemiroff 1988, Schneider & Wambsganss 1990). The effects of microlensing in the BLR have already been investigated theoretically (e.g. Nemiroff 1988, Schneider & Wambsganss 1990, Hutsemekers et al. 1994, Popović et al. 2001, Abajas et al. 2002, 2007, Simić & Popović 2014), and observed as symmetric and asymmetric profiles distortions in low and high ionization lines (Richards et al. 2004a, Chartas et al. 2002, Dai et al. 2003, Chartas et al. 2004, Wayth et al. 2005, Sluse et al. 2007, 2011, O’Dowd et al. 2011, Motta et al. 2012, Guerras et al. 2013, Braibant et al. 2014, 2016). In addition, the BLR size has been estimated and are compatible with the RM measurements (Wayth et al. 2005, Sluse et al. 2011, Guerras et al. 2013, Sluse et al. 2015).

Furthermore, microlensing can produce chromatic microlensing. Since microlensing is sensitive to the angular size of the source, if the size of the region that is emitting varies with wavelength, then the micro-magnification should be wavelength dependent (Mediavilla et al. 2011), and chromatic microlensing is expected (e.g. Wambsganss & Paczynski 1991, Mosquera et al. 2009, Rojas et al. 2014, Motta et al. 2017, Rojas et al. 2020). This effect should be stronger for shorter wavelengths and as the wavelength increases, it should not be seen. The systems that shows this effect in the microlensing analysis, could have the accretion disk size measured (e.g. Mediavilla et al. 2011, Motta et al. 2012, Rojas et al. 2014, 2020).

### 1.3 Supermassive black hole mass

Section 1.1.2 confirmed that physical parameters of the SMBH is correlated with those of the host galaxy. This means, that precise measurement of the  $M_{BH}$  is key in the understanding of the coevolution between the SMBH growth and their host galaxy (see Ferrarese & Ford 2005, Kormendy & Ho 2013).

Different methods exist to measure the  $M_{BH}$  in AGNs: RM method (e.g., Blandford & McKee 1982, Peterson 1993, Netzer & Peterson 1997, Kaspi et al. 2000, Peterson et al. 2004, Bentz et al. 2009, Mejía-Restrepo et al. 2016, Shen et al. 2016, 2019); the single-epoch method (e.g., Vestergaard 2002, McLure & Jarvis 2002, McLure & Dunlop 2004, Greene & Ho 2005, Vestergaard & Osmer 2009, Greene et al. 2010, Shen et al. 2011, Shen & Liu 2012, Trakhtenbrot & Netzer 2012); 2D velocity maps (e.g. Grier et al. 2013); polarization in broad emission lines (e.g. Savić et al. 2018); dynamical BH mass (e.g., Davies et al. 2006, Onken

---

et al. 2007, Hicks & Malkan 2008); AD fitting (e.g., Malkan 1983, Laor 1990, Ghisellini et al. 2010, Calderone et al. 2013, Campitiello et al. 2019); microlensing in QSOs (e.g. Irwin et al. 1989, Richards et al. 2004a, Dai et al. 2010, Mosquera & Kochanek 2011, Sluse et al. 2011, Guerras et al. 2013), and a recent method based on gravitational redshifts of FeIII lines in QSOs (Mediavilla et al. 2018, 2019). Each of them have uncertainties linked to their models, features of the systems and the quality of the data (e.g. McLure & Jarvis 2002, Vestergaard & Peterson 2006a, Marconi et al. 2008, Calderone et al. 2013, Campitiello et al. 2020). The RM method is the most accurate technique based on direct measurements and is related to the BLR (see section 1.1.1).

Almost all the RM studies have focused on the low-redshift AGNs with optical luminosities  $\lambda L_{\lambda}(5100\text{\AA}) < 10^{46.5} \text{ erg s}^{-1}$  (Kaspi et al. 2021). Unfortunately, the time delay obtained from the RM technique increases with the source luminosity (MacLeod et al. 2010) and is enhanced by cosmological time dilation, making it difficult to apply this technique to high luminosity and high- $z$  objects. In addition, it is needed telescopes with large collecting areas since quasars are faint, and they show very low amplitude variations ( $< 20\%$ ) in short timescales (Lira et al. 2018). Several early RM efforts for high-luminosity quasars failed to detect reverberation time lags due to the short duration of the projects (e.g. Welsh et al. 2000, Trevese et al. 2006, Kaspi et al. 2007, Saturni et al. 2016).

One remarkable finding of the RM studies in local AGN is a tight correlation between the measured BLR size of the  $H\beta$  emitting region and the optical continuum luminosity (Figure 1.12) measured at restframe 5100 Å (R-L relation, Bentz et al. 2006, Zu et al. 2011). This offers an alternative technique to estimate the size of the BLR based on the luminosity of the quasar and hence its SMBH mass (the single epoch (SE) method, e.g. Vestergaard 2004, Shen & Liu 2012, Mejía-Restrepo et al. 2016).

At low redshifts ( $z \leq 0.7$ ), SE black hole masses are typically estimated with  $H\alpha$  and  $H\beta$  BELs and the continuum luminosity at 5100 Å (see Bentz et al. 2013, and references therein). However, at higher redshifts these BELs are shifted to the infrared and most of the SMBH masses are estimated at rest-frame UV wavelengths using MgII and CIV BELs in quasars with  $1.5 \leq z \leq 2.5$ . The latter presents the several drawbacks: 1) these UV lines lack a local calibration due to the difficulty in obtaining UV RM measurements, 2) their indirect calibrations are restricted to high-luminosity objects (Mejía-Restrepo et al. 2016), 3) MgII may have a small but significant dependence on the Eddington ratio of the AGN and might

---

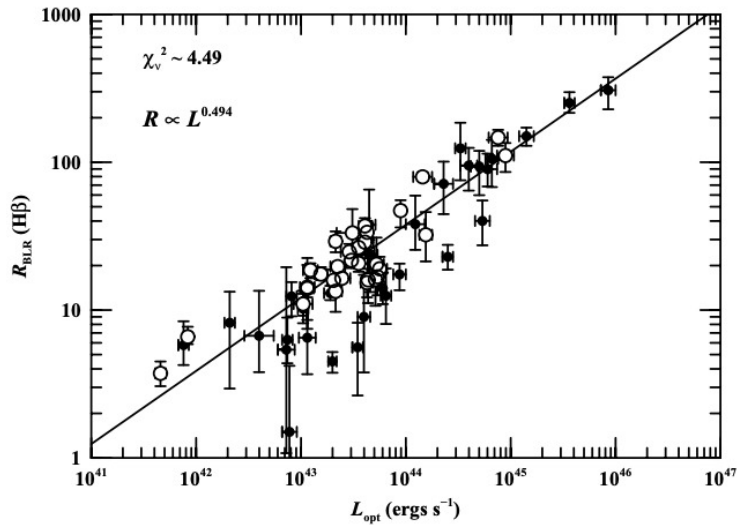


FIGURE 1.12: R-L relation for H $\beta$  from [Peterson 2010](#). The luminosity is at  $\lambda = 5100 \text{ \AA}$  and the BLR radius in light days.

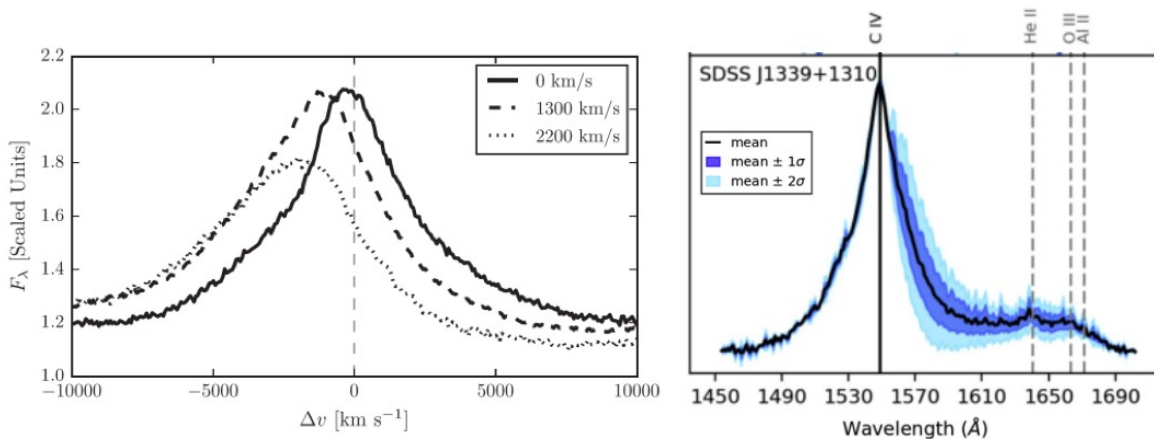


FIGURE 1.13: CIV BEL widths showing: (Right) the blue asymmetries (blueshifts) with the line centroid displaced to the blue, which are a clear signal of outflows originating in disc winds ([Coatman et al. 2016](#)) and (left) the presence of microlensing or variability in the wing (Figure adapted from [Fian et al. 2018](#))

not be reliable in objects with  $\text{FWHM}(\text{MgII}) \geq 6000 \text{ km/s}$  ([Marziani et al. 2013](#)), and 4) there are concerns regarding CIV because its width could be affected by wind flows from ejected disk material ([Mejía-Restrepo et al. 2018](#), [Assef et al. 2011](#), [Coatman et al. 2016](#)) and microlensing in the case of lensed QSOs ([Fian et al. 2018](#)) (Figure 1.13). In addition, CIV emission line is more asymmetric than the balmer lines and MII, and the width is not well correlated with those of H $\beta$  and MgII (e.g. [Baskin & Laor 2005](#), [Shen et al. 2008](#)).

However, microlensing could be easily detected by placing pairs of images of a lensed AGN in one slit and comparing their BEL's profiles (see for e.g. [Motta et al. 2017](#), [Fian et al. 2018](#)).

The Balmer lines are the most studied lines in RM, and since the R-L relation was originally measured for the  $H\beta$  at  $L_{5100}$  (e.g., [Kaspi et al. 2000](#), [Bentz et al. 2006](#)), it is reasonable to argue that the virial mass estimator based on the Balmer lines is the most reliable one. The width of the  $H\alpha$  emission line is well correlated with the broad of  $H\beta$ , and it could substitute in its absence (e.g. [Greene & Ho 2005](#).)

Recently, the SE method has been applied to investigate lensed AGNs. The high magnification allows us to obtain spectra for sources that would otherwise be extremely time consuming to obtain. Near-IR spectra observations of samples of lensed AGNs from CASTLES used  $H\alpha$  and  $H\beta$  and compared them with other lines, such as MgII, CIV and FeIII ([Greene et al. 2010](#), [Assef et al. 2011](#), [Mediavilla et al. 2018, 2019](#)). Just objects in the original CASTLES sample ( $\sim 100$ ) have  $M_{BH}$  measurements: 11 using  $H\alpha$  and/or  $H\beta$  lines (linked to the R-L relation) and 33 using CIV (more prone to microlensing) and MgII. Although these estimations are in agreement with the RM method, there are some differences at lower luminosities (Figure 1.14).

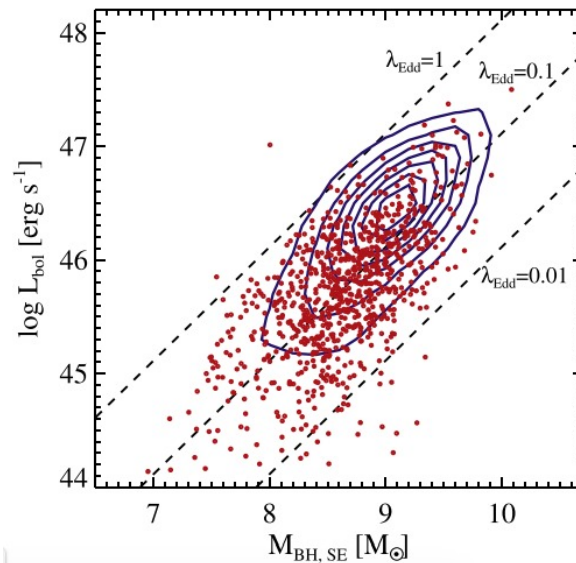


FIGURE 1.14: BH mass and luminosity plane from [Shen et al. 2019](#). The blue contours are for the SDSS-DR7 quasars and the red point the SDSS-RM sample. They use the single-epoch  $M_{BH}$ .

## 1.4 Objectives

One of the key ingredients in the galaxy formation and evolution is the understanding of the SMBH growth and their coevolution with their host galaxies. Specially with the tight correlation that exist between the  $M_{BH}$  and the velocity dispersion, luminosity and mass of the bulge of the host galaxy. Although the SMBH mass controls the properties of the AGN, their mass estimation remains uncertain.

The RM and SE method are the most used techniques to measure the masses of active SMBHs, but they have several drawbacks. RM method are limited to low redshift sources and luminosities  $< 10^{46.5}$  erg s<sup>-1</sup> due that the time delay from RM technique increases with luminosity. SE black hole masses are typically estimated in low redshift quasars using H $\alpha$  and H $\beta$  broad emission lines, but this lines are shifted into the NIR at higher redshifts. Due to this,  $M_{BH}$  were estimated in the optical using MgII and CIV lines, even though this lines may be affected by wind flows from ejected disk material and microlensing. In addition, high S/N spectra for high redshift systems are difficult to obtain. The Balmer lines remain the most reliable emission lines for measuring the  $M_{BH}$ .

In this thesis, I will calculate the  $M_{BH}$  for a sample of lensed quasars using the lensing effect (which magnifies the flux of distant AGNs):

First, I want to measure the  $M_{BH}$  using the SE method by fitting the H $\alpha$  and H $\beta$  BEL profile in lensed quasars. Several studies shows  $M_{BH}$  estimation (e.g. [Peng et al. 2006b](#), [Assef et al. 2011](#), [Sluse et al. 2012](#)), but they normally used MgII and CIV emission lines. [Greene et al. 2010](#) measured the  $M_{BH}$  using H $\alpha$  and/or H $\beta$  emission lines, but no further analysis using this lines has been made for lensed quasars. For those objects that has previous black hole mass, we can test the reliability of the CIV and MgII  $M_{BH}$  estimates by comparing them with the Balmer lines. As an additional science return, in those cases that microlensing is affecting the CIV and/or MgII BEL, upper limits for the emitting region could be obtained ([Fian et al. 2018](#)). New systems have been discovered in the last few years (e.g [Lemon et al. 2020](#)), that can help us with the increase of our sample.

Secondly, once the new data sample is in place, I will test the Bolometric luminosity vs  $M_{BH}$  relation for lensed AGNs and compare it with the non-lensed AGNs and the literature on lensed AGNs.

---

Thirdly, if chromatic microlensing is detected, a further analysis in the estimation of the accretion disk size will be performed. Several estimations of the accretion disk size have been published using the chromatic microlensing effect, and the size they have obtained is larger than the accretion disk size obtained by the SE method in AGNs. The size of the emitting region will be compared with the two methods and with the literature.

---

## Chapter 2

# Observation and data reduction

I present the data used in this thesis from three instruments: LUCIFER (large Binocular Telescope), MMIRS (Magellan 6.5m Clay telescope), and X-shooter (Very Large Telescope). The first two were already reduced by collaborators, while the X-shooter data are from my programs. In the first section, the sample selection of lensed quasars is described, followed by a detailed reduction of the X-shooter programs. Finally I summarized the reductions of the LUCIFER and MMIRS data.

### 2.1 Sample selection

The sample of lensed AGNs is now about  $\sim 220$  (according to the GLQ database<sup>1</sup>), of which 100 are from the CASTLES database and the rest from Inada et al. 2006, Jackson 2008, Oguri et al. 2008a,b, Inada et al. 2009, Kayo et al. 2010, Inada et al. 2014, Agnello et al. 2015, More et al. 2016, Rusu et al. 2016, Ostrovski et al. 2017, Schechter et al. 2017, Lemon et al. 2018, Lucey et al. 2018, Lemon et al. 2019, Shajib et al. 2019 and recently discovered by the STRong lensing Insights into the Dark Energy Survey (STRIDES; Anguita et al. 2018, Treu et al. 2018, Lemon et al. 2020) and the Dark Energy Survey (DES; Agnello et al. 2018, Spiniello et al. 2019). Selecting only those lenses with an image separation of  $\geq 0.6$  arcsec (for deblending purposes), a source redshift range of  $0.3 < z_s < 3.5$  (to make sure the Balmer lines are visible in the NIR) and the confirmed lenses from CASTLES (69), it leaves us with a sample of 159 targets (see table 2.1). From the confirmed lenses of the CASTLES database,

---

<sup>1</sup><https://research.ast.cam.ac.uk/lensedquasars/index.html>

we kept B1422+231 even though it didn't fulfill the previous requirement ( $z_s=3.62$ ), but it has previous  $M_{BH}$  measurement.

To select the systems for the X-shooter program, we first separated them by their coordinates into those that were just accessible from the southern hemisphere (83 systems). We then choose the ones with an image separation of  $\geq 1.0$  arcsec (to deblend each component) and look into their magnitudes. In order to obtain a S/N  $> 30$  in NIR (Balmer lines) and S/N  $> 15$  in UVB and VIS (MgII and CIV emission lines) we selected bright systems (F160W  $< 19.00$  mag). We prioritize those targets that had previous  $M_{BH}$  using MgII and CIV from the literature, so that we could compare them with the  $M_{BH}$  using the Balmer lines and also new quadruple lensed quasars. Of the 41 systems that fulfilled the criteria, we selected eight systems (Table 2.2), six are from CASTLES and two from [Shajib et al. 2019](#). WISE0259-1635 had already been observed using an X-shooter (Program ID: 0102.A-0335(A)), but we requested more time to reach the desire S/N in the BEL.

On the other hand, the MMIRS and LUCIFER data was given by private communication, and the criteria for those observations were that one (or both) of the Balmer lines were visible and that the S/N was above three (see table 2.5). This last criterion is reasonable because S/N $>3$  is enough to have reliable  $M_{BH}$  using H $\alpha$  broad emission line ([Mejía-Restrepo et al. 2016](#)). For eight systems of this sample (with the exception of WFI2026-4536 and HE0512-3329), the  $M_{BH}$  was previously measured using the MgII and/or CIV emission lines ([Assef et al. 2011](#), [Sluse et al. 2012](#)). This group of overlapping systems is important in order to compare previous results with the  $M_{BH}$  measured from the Balmer lines.

TABLE 2.1: Sample of gravitational lensed quasars following the selection process described in section 2.1. The redshift, separation and magnitude information is obtained from CASTLES webpage and/or GLQ database. The measured  $M_{BH}$  from the literature is shown along with the emission line used, luminosity, FWHM and reference.

Name	$z_s$	$z_l$	Sep. [""]	F160W <sup>a</sup> [mag]	Line	$M_{BH}$ <sup>b</sup> [ $M_{\odot}$ ]	$L_{ref}$ <sup>c</sup> [ $L_{\odot}$ ]	FWHM [km/s]	Ref. <sup>d</sup>
J0011-0845	1.7		1.89	$20.69 \pm 0.01^i$					
PSJ0028+0631	1.06		2.81	$18.98 \pm 0.01$					
J0047+2514	1.20		1.73	$20.74 \pm 0.02^i$					
Q0047-2808	3.60	0.48		$17.85 \pm 0.09$					
HE0047-1756	1.678	0.407	1.43	$15.33 \pm 0.02$	MgII	$8.86 \pm 0.23$	$45.32 \pm 0.70$	$4145 \pm 365$	4
					CIV	9.17	$46.07 \pm 0.3$	70	1
J0102+2445	2.085	0.272?	2.38	$19.21 \pm 0.01^i$					
DESJ0112-1650	0.99	0.54	1.38	$20.08 \pm 0.04^i$					
SDSSJ0114+0722	1.828	0.408	1.7	$20.88 \pm 0.07^i$					
DESJ0115-5244	1.64	-	1.20	$19.91 \pm 0.10^i$					
PSJ0123-0455	1.38		2.00	$19.87 \pm 0.01^i$					

TABLE 2.1: **Table 2.1 Continued:**

Name	$z_s$	$z_l$	Sep. [""]	F160W <sup>a</sup> [mag]	Line	$M_{BH}$ <sup>b</sup> [ $M_\odot$ ]	$L_{ref}$ <sup>c</sup> [ $L_\odot$ ]	FWHM [km/s]	Ref. <sup>d</sup>
PMNJ0134-0931	2.22	0.765	0.68	$15.25 \pm 0.03$					
J0140-1152	1.80	0.28	1.47	$18.87 \pm 0.01^i$					
Q0142-100	2.719	0.491	2.23	$15.28 \pm 0.02$	CIV	$9.51 \pm 0.33$	$46.42 \pm 0.7$	$4750 \pm 220$	4
					CIV	9.35	$46.85 \pm 0.3$	75	1
					CIV	$9.51 \pm 0.33$	$46.83 \pm 0.2$	$4750 \pm 220$	3
					H $\beta$	$8.94 \pm 0.3$	$46.27 \pm 0.2$	$2700 \pm 600$	3
					H $\alpha$	$9.33 \pm 0.23$	$46.27 \pm 0.2$	$3800 \pm 300$	3
					H $\beta$	$9.1 \pm 0.4$	$46.42 \pm$	$2700 \pm 600$	2
					H $\alpha$	$9.4 \pm 0.3$	$46.42 \pm 0.3$	$3800 \pm 300$	2
J0146-1133	1.44		1.68	$18.79 \pm 0.01^i$					
PSJ0147+4630	2.377	0.678	3.26	$18.3 \pm 0.1$					
DESJ0150-4041	1.85		2.81	$19.19 \pm 0.18$					
QJ0158-4325	1.29	0.317	1.22	$16.47 \pm 0.03$					
J0203+1612	2.18		2.73	$20.37 \pm 0.01^i$					
OGLEJ0218-7335	2.16		1.48	$19.61 \pm 0.02^i$					
J0228+3953	2.07		1.57	$19.9 \pm 0.03$					
HE0230-2130	2.162	0.523	2.05	$19.02 \pm 0.09^*$					
J0235-2433	1.44		2.04	$19.58 \pm 0.02^i$					
DESJ0245-0556	1.54		1.90	$19.27 \pm 0.05$					
SDSS0246-0825	1.689	0.723	1.10	$16.74 \pm 0.02$	MgII	$8.59 \pm 0.36$	$45.19 \pm 0.7$	$3700 \pm 670$	4
					CIV	$8.23 \pm 0.33$	44.53	$4400 \pm 220$	3
					H $\beta$	$8.00 \pm 0.31$	$44.59 \pm 0.2$	$2500 \pm 600$	3
					H $\alpha$	$8.08 \pm 0.23$	$44.59 \pm 0.2$	$2500 \pm 200$	3
J0246-1845	1.86		1.00	$18.39 \pm 0.01^i$					
SDSSJ0248+1913	2.44		1.76	$20.8 \pm 0.1$					
WISEJ0259-1635	2.16	0.905?	1.63	$18.48 \pm 0.03$					
J0259-2338	1.19		2.92	$19.66 \pm 0.02^i$					
DESJ0340-2545	1.68		6.81	$18.31 \pm 0.07$					
DESJ0405-3308	1.713		1.57	$19.43 \pm 0.07$					
DESJ0407-5006	1.515		1.72	$18.01 \pm 0.03^i$					
DESJ0407-1931	2.27	0.29	2.52	$20.23 \pm 0.06^i$					
DESJ0408-5354	2.375	0.597	4.29	$20.18 \pm 0.03$					
MG0414+0534	2.64	0.96	2.4	$15.54 \pm 0.01$	H $\beta$	9.26	$45.73 \pm 0.3$	4370	1
					H $\alpha$	$9.4 \pm 0.3$	$45.73 \pm 0.3$	$5300 \pm 300$	2
PSJ0417+3325	1.41		1.68	$19.41 \pm 0.01^i$					
HE0435-1223	1.693	0.454	2.54	$17.31 \pm 0.02$	MgII	$8.76 \pm 0.44$	$45.14 \pm 0.7$	$4930 \pm 195$	4
					CIV	8.7	$45.19 \pm$	4755	1
DESJ0501-4118	2.1		3.72	$18.61 \pm 0.01^i$					
HE0512-3329	1.57	0.93?	0.65	$15.81 \pm 0.02$					
DESJ0600-4649	2.21		2.38	$19.17 \pm 0.06^i$					
B0712+472	1.339	0.406	1.46	$20.46 \pm 0.04$	MgII	7.85	$42.74 \pm 0.3$	6698	1
ULASJ0743+2457	2.165	0.381	1.03	$16.88 \pm 0.05^k$					
SDSS0746+4403	1.998	0.513	1.08	$19.08 \pm 0.01^i$					
MG0751+2716	3.20	0.35	0.7	$18.87 \pm 0.16$					
SDSS0806+2006	1.540	0.573	1.49	$16.87 \pm 0.01$	MgII	$8.53 \pm 0.35$	45.9	$3370 \pm 430$	4
HS0810+2554	1.51		0.91	$14.20 \pm 0.02$	CIV	$7.00 \pm 0.33$	$44.44 \pm 0.2$	$3530 \pm 160$	3
					H $\beta$	$8.62 \pm 0.22$	$44.84 \pm 0.2$	$4400 \pm 60$	3
					H $\alpha$	$8.65 \pm 0.22$	$44.84 \pm 0.2$	$3800 \pm 0$	3

TABLE 2.1: **Table 2.1 Continued:**

Name	$z_s$	$z_l$	Sep. [""]	F160W <sup>a</sup> [mag]	Line	$M_{BH}$ <sup>b</sup> [ $M_\odot$ ]	$L_{ref}$ <sup>c</sup> [ $L_\odot$ ]	FWHM [km/s]	Ref. <sup>d</sup>
SDSSJ0819+5356	2.239	0.294	4.04	$16.39 \pm 0.14^k$					
ULASJ0820+0812	2.024	0.803	2.24	$17.21 \pm 0.03^k$					
SDSSJ0821+4542	2.066	0.349	1.35	$20.76 \pm 0.14^r$					
SDSSJ0832+0404	1.116	0.659	2.17	$16.5 \pm 0.06^k$					
PSJ0840+3550	1.77	0.26	2.74	$19.92 \pm 0.01^i$					
SDSS0903+5028	3.584	0.388	2.84	$17.01 \pm 0.01$					
SDSSJ0904+1512	1.826		1.07	$15.73 \pm 0.03^k$					
RXJ0911+0551	2.763	0.769	3.25	$17.59 \pm 0.02$	CIV	8.9	$45.57 \pm 0.3$	5115	1
SBS0909+523	1.378	0.830	1.11	$14.60 \pm 0.02$	MgII	9.59	$45.95 \pm 0.3$	8769	1
					CIV	$8.51 \pm 0.32$	$46.08 \pm$	$2360 \pm 80$	3
					H $\beta$	$9.29 \pm 0.23$	$46.31 \pm 0.2$	$3950 \pm 170$	3
					H $\alpha$	$9.15 \pm 0.24$	$46.31 \pm 0.2$	$3060 \pm 340$	3
					H $\beta$	$9.2 \pm 0.5$	$45.96 \pm 0.3$	$4100 \pm 1600$	2
					H $\alpha$	$9.0 \pm 0.3$	$45.96 \pm 0.3$	$3100 \pm 600$	2
SDSSJ0921+2854	1.41	0.445	1.89	$18.03 \pm 0.01^i$					
SDSS0924+0219	1.523	0.393	1.81	$17.96 \pm 0.02$	MgII	$7.93 \pm 0.34$	$43.98 \pm 0.7$	$3660 \pm 310$	4
					MgII	8.09	$44.35 \pm 0.3$	3514	1
J0941+0518	1.54	0.343	5.37	$18.66 \pm 0.01^i$					
PSJ0949+4208	1.27	0.508	2.60	$19.61 \pm 0.03^i$					
FBQ0951+2635	1.247	0.260	1.10	$15.62 \pm 0.03$	MgII	$9.21 \pm 0.26$	$45.83 \pm 0.7$	$5850 \pm 133$	4
					MgII	8.95	$45.90 \pm 0.3$	4320	1
					H $\beta$	$9.5 \pm 0.3$	$45.48 \pm 0.3$	$7600 \pm 800$	2
					H $\alpha$	$9.4 \pm 0.3$	$45.48 \pm 0.3$	$6300 \pm 400$	2
BRI0952-0115	4.5	0.632	0.99	$17.07 \pm 0.01$	CIV	$9.14 \pm 0.4$	$45.77 \pm 0.7$	$5210 \pm 1300$	4
					CIV	9.14	$46.00 \pm 0.3$	5186	1
Q0957+561	1.413	0.3562	6.17	$15.60 \pm 0.03$	CIV	9.3	$46.71 \pm 0.3$	4044	1
					MgII	9.48	$46.43 \pm 0.3$	5974	1
					CIV	$8.97 \pm 0.32$	$46.31 \pm 0.2$	$3470 \pm 80$	3
					H $\beta$	$8.86 \pm 0.33$	$45.79 \pm 0.2$	$3300 \pm 900$	3
					H $\alpha$	$8.87 \pm 0.23$	$45.79 \pm 0.2$	$3000 \pm 200$	3
					H $\beta$	$9.2 \pm 0.4$	$46.25 \pm 0.3$	$3300 \pm 900$	2
					H $\alpha$	$9.1 \pm 0.3$	$46.25 \pm 0.3$	$3000 \pm 200$	2
SDSS1001+5027	1.841	0.415	2.93	$17.32 \pm 0.01^i$					
J1004+1229	2.64	0.95	1.54	$15.88 \pm 0.02$	CIV	9.30	$46.41 \pm 0.3$	4869	1
					H $\beta$	$9.6 \pm 0.4$	$46.12 \pm 0.3$	$5900 \pm 1500$	2
					H $\alpha$	$9.3 \pm 0.3$	$46.12 \pm 0.3$	$3800 \pm 100$	2
SDSS1004+4112	1.74	0.68	14.72	$17.77 \pm 0.04$					
SDSS1011+0143	2.701	0.331	3.67	$23.79 \pm 0.01^B$					
LBQS1009-0252	2.74	0.871	1.54	$16.63 \pm 0.02$	CIV	9.04	$46.27 \pm 0.3$	3931	1
					MgII	8.93	$46.08 \pm 0.3$	3853	1
Q1017-207	2.55	1.088?	0.85	$15.66 \pm 0.03$	CIV	9.22	$46.42 \pm 0.3$	4413	1
SDSS1021+4913	1.72	0.451	1.16						
FSC10214+4724	2.286	0.9?	1.59	$20.40 \pm 0.11^*$					
SDSS1029+2623	2.199	0.584	22.54						
B1030+074	1.535	0.599	1.65	$18.07 \pm 0.03$	MgII	8.54	$44.82 \pm 0.3$	4860	1
SDSSJ1055+4628	1.249	0.388	1.15	$17.1 \pm 0.03^k$					
HE1104-1805	2.32	0.729	3.19	$15.91 \pm 0.01$	CIV	9.37	$46.18 \pm 0.3$	6068	1
					CIV	$9.32 \pm 0.32$	$46.15 \pm 0.2$	$5750 \pm 50$	3

TABLE 2.1: Table 2.1 Continued:

Name	$z_s$	$z_l$	Sep. [""]	F160W <sup>a</sup> [mag]	Line	$M_{BH}$ <sup>b</sup> [ $M_\odot$ ]	$L_{ref}$ <sup>c</sup> [ $L_\odot$ ]	FWHM [km/s]	Ref. <sup>d</sup>
PG1115+080	1.735	0.311	2.43	$15.71 \pm 0.02$	H $\beta$	$8.77 \pm 0.3$	$45.38 \pm 0.2$	$3800 \pm 900$	3
					H $\alpha$	$9.05 \pm 0.23$	$45.38 \pm 0.2$	$4700 \pm 200$	3
					CIV	8.96	$45.74 \pm 0.3$	4945	1
					MgII	9.09	$45.39 \pm 0.3$	6693	1
					CIV	$8.78 \pm 0.32$	$45.47 \pm 0.2$	$4670 \pm 130$	3
					H $\beta$	$8.66 \pm 0.23$	$44.93 \pm 0.2$	$4400 \pm 200$	3
					H $\alpha$	$8.68 \pm 0.22$	$44.93 \pm 0.2$	$4000 \pm 100$	3
					H $\beta$	$8.8 \pm 0.3$	$45.15 \pm 0.3$	$4400 \pm 200$	2
					H $\alpha$	$8.8 \pm 0.2$	$45.15 \pm 0.3$	$4000 \pm 100$	2
SDSSJ1128+2402	1.608		0.78	$18.48 \pm 0.02^i$					
RXJ1131-1231	0.658	0.295	3.23	$15.97 \pm 0.02$	MgII	$8.32 \pm 0.62$	$44.29 \pm 0.7$	$5630 \pm 165$	4
SDSS1138+0314	2.438	0.445	1.44	$17.96 \pm 0.02$	H $\beta$	$7.9 \pm 0.6$	45	$4545 \pm 255$	4
					H $\beta$	7.78	$43.95 \pm 0.3$	3318	1
					CIV	$7.69 \pm 0.33$	$44.82 \pm 0.7$	$1990 \pm 180$	4
					CIV	$7.71 \pm 0.33$	$44.83 \pm 0.2$	$1990 \pm 180$	3
					H $\beta$	$8.5 \pm 0.23$	$44.81 \pm 0.2$	$3930 \pm 300$	3
H $\alpha$	$8.22 \pm 0.22$	$44.81 \pm 0.2$	$2570 \pm 40$	3					
SDSS1155+6346	2.888	0.176	1.93	$16.94 \pm 0.02$					
B1152+200	1.019	0.438	1.56	$15.63 \pm 0.02$					
SDSS1206+4332	1.789	0.748	3.03						
SDSSJ1216+3529	2.013	0.55*	1.49	$16.82 \pm 0.03^k$					
SDSS1226-0006	1.123	0.517	1.26	$17.24 \pm 0.02$	MgII	$8.96 \pm 0.43$	$44.94 \pm 0.7$	$7840 \pm 550$	4
					MgII	$8.83 \pm 0.26$	$44.48 \pm 0.3$	8143	1
J1238+2846	2.355		2.43	$20.49 \pm 0.02^i$					
SDSSJ1254+1857	1.717	0.555	2.32	$21.98 \pm 0.18^r$					
SDSSJ1304+2001	2.175	0.4?	1.86	$18.05 \pm 0.01^i$					
2M1310-1714	1.975	0.293	5.74	$19.81^i$					
SDSSJ1313+5151	1.877	0.194	1.22	$14.62 \pm 0.02^k$					
SDSSJ1322+1052	1.717	0.55?	2.00	$16.22 \pm 0.06^k$					
SDSSJ1330+3800	2.254		1.44	$20.16 \pm 0.11^r$					
SDSSJ1332+0347	1.438	0.191	1.12	$19.28 \pm 0.03^i$					
SDSSJ1334+3315	2.426	0.557?	0.84	$17.67 \pm 0.06^k$					
SDSSJ1335+0118	1.570	0.440	1.62	$16.18 \pm 0.02$	MgII	$9.19 \pm 0.26$	$45.74 \pm 0.7$	$6110 \pm 205$	4
					MgII	9.19	$45.6 \pm 0.3$	6706	1
SDSSJ1339+1310	2.241	0.607	1.70	$18.28 \pm 0.01^i$					
SDSSJ1349+1227	1.722	0.65?	3.01	$17.14 \pm 0.01^i$					
SDSS1353+1138	1.624	0.25	1.39	$15.16 \pm 0.01$					
Q1355-2257	1.370	0.701	1.23	$15.91 \pm 0.02$	MgII	$9.04 \pm 0.34$	$45.69 \pm 0.7$	$5035 \pm 140$	4
B1359+154	3.235	0.9?	1.71	$24.01 \pm 0.05^*$					
SDSS1402+6321	0.48	0.20	1.35						
ULASJ1405+0959	1.81	0.66*	1.97	$18.71 \pm 0.01^i$					
SDSS1406+6126	2.135	0.27	1.99	$19.38 \pm 0.01^i$					
HST14113+5211	2.811	0.465	1.8	$25.59 \pm 0.14^*$					
H1413+117	2.56	0.94?	1.35	$15.83 \pm 0.04$	H $\beta$	$9.12 \pm 0.01$	$45.72 \pm 0.7$	$5170 \pm 250$	4
					CIV	$8.41 \pm 0.3$	45.61	2846	1
					CIV	$8.39 \pm 0.35$	$45.73 \pm 0.2$	$2540 \pm 370$	3
					H $\beta$	$9.39 \pm 0.33$	$45.63 \pm 0.2$	$6700 \pm 1900$	3
					H $\alpha$	$9.29 \pm 0.26$	$45.63 \pm 0.2$	$5300 \pm 800$	3

TABLE 2.1: Table 2.1 Continued:

Name	$z_s$	$z_l$	Sep. [""]	F160W <sup>a</sup> [mag]	Line	$M_{BH}$ <sup>b</sup> [ $M_\odot$ ]	$L_{ref}$ <sup>c</sup> [ $L_\odot$ ]	FWHM [km/s]	Ref. <sup>d</sup>
					H $\beta$	$9.5 \pm 0.3$	$45.67 \pm 0.3$	$6700 \pm 1900$	2
					H $\alpha$	$9.3 \pm 0.3$	$45.67 \pm 0.3$	$5300 \pm 800$	2
HST14176+5226	3.40	0.81	2.83	$24.85 \pm 0.13^*$					
B1422+231	3.62	0.339	1.28	$14.41 \pm 0.02$	CIV	9.68	$46.88 \pm 0.3$	5628	1
					MgII	9.34	$46.74 \pm 0.3$	4341	1
					CIV	$9.65 \pm 0.32$	$46.83 \pm 0.2$	$5560 \pm 20$	3
					H $\beta$	$9.72 \pm 0.38$	$46.42 \pm 0.2$	$6100 \pm 2200$	3
					H $\beta$	$9.9 \pm 0.4$	$46.65 \pm 0.3$	$6100 \pm 2200$	2
SDSSJ1455+1447	1.424	0.42*	1.75	$15.81 \pm 0.001^k$					
SDSSJ1458-0202	1.724		2.15	$21.5 \pm 0.02^i$					
PSJ1508+3844	1.68		1.70	$21.58 \pm 0.06^i$					
SDSSJ1515+1511	2.054	0.742	2.01	$16.01 \pm 0.01^k$					
J1515+3137	1.97		1.50	$19.67 \pm 0.02^i$					
J1518+4658	2.36		1.36	$19.46 \pm 0.03^i$					
SBS1520+530	1.86	0.761?	1.59	$17.58 \pm 0.02$	CIV	8.94	$45.64 \pm 0.3$	5141	1
SDSSJ1524+4409	1.21	0.320	1.80	$19.54 \pm 0.04^i$					
J1524+4801	1.70		2.22	$19.96 \pm 0.01^i$					
HST15433+5352	2.092	0.497	1.18						
J1537-3010	1.72		3.29	$19.79 \pm 0.05^i$					
MG1549+3047	1.17	0.11	1.7	$20.52 \pm 0.04$					
B1600+434	1.589	0.414	1.4	$20.66 \pm 0.03$	MgII	8.00	$44.23 \pm 0.3$	3575	1
PSJ1602+4526	2.16	0.426	2.7	$20.2 \pm 0.01^i$					
PSJ1606-2333	1.69		1.74	$19.5 \pm 0.1$					
B1608+656	1.39	0.630	2.27	$16.76 \pm 0.05$					
J1612+3920	1.68		2.74	$19.95 \pm 0.01^i$					
SDSSJ1620+1203	1.158	0.398	2.81	$17.02 \pm 0.01^k$					
J1627-0224	1.91		3.77	$19.11 \pm 0.01^i$					
FBQ1633+3134	1.518	0.684?	0.66	$16.85 \pm 0.01^*$					
PSJ1640+1045	1.7		2.21	$18.49 \pm 0.01^i$					
SDSSJ1650+4251	1.543	0.577?	1.18	$17.15 \pm 0.1^i$					
J1653+5155	1.165		1.63	$20.09 \pm 0.01^i$					
MG1654+1346	1.74	0.25	2.1	$19.12 \pm 0.02$					
PSJ1709+3828	1.38		1.66	$20.7 \pm 0.03^i$					
PSJ1721+8842	2.37	0.184	4.03	$19.14 \pm 0.03^i$					
PKS1830-211	2.51	0.886	0.99	$16.94 \pm 0.01$					
PSJ1831+5447	1.07		2.39	$19.22 \pm 0.02^i$					
PMNJ1838-3427	2.78	0.36?	0.99	$17.35 \pm 0.04$					
B1933+503	2.638	0.755	1.52	$17.11 \pm 0.00$					
B1938+666	2.059	0.881	1.02	$18.67 \pm 0.08$					
J1949+7732	1.63		1.59	$18.7 \pm 0.05^i$					
MG2016+112	3.27	1.004	2.56	$20.48 \pm 0.05$	CIV	7	44.56	25	1
WGD2021-4115	1.390	0.335	2.75	$18.73 \pm 0.01_i$					
WFI2026-4536	2.23	1.04?	1.34	$15.64 \pm 0.01$					
WFI2033-4723	1.662	0.661	2.53	$17.22 \pm 0.02$	MgII	$8.63 \pm 0.35$	$45.19 \pm 0.7$	$3960 \pm 465$	4
WGD2038-4008	0.777	0.230	2.87	$18.48 \pm 0.03$					
B2045+265	1.28	0.87	1.9	$19.77 \pm 0.02$	MgII	7.00	$41.49 \pm 0.3$	4979	1
PSJ2124+1632	1.28		3.01	$18.8 \pm 0.02^i$					
J2132+2603	2.26		1.77	$19.31 \pm 0.04^i$					

TABLE 2.1: **Table 2.1 Continued:**

Name	$z_s$	$z_l$	Sep. [""]	F160W <sup>a</sup> [mag]	Line	$M_{BH}$ <sup>b</sup> [ $M_\odot$ ]	$L_{ref}$ <sup>c</sup> [ $L_\odot$ ]	FWHM [km/s]	Ref. <sup>d</sup>
J2145+6345	1.56		2.07	$16.71 \pm 0.01^i$					
SDSSJ2146-0047	2.381	0.799	1.39	$19.92 \pm 0.16$					
HE2149-2745	2.033	0.603	1.70	$15.67 \pm 0.03$	CIV	$9.82 \pm 0.4$	$45.29 \pm 0.7$	$7470 \pm 1865$	4
					CIV	9.82	$46.67 \pm 0.3$	7520	1
DESJ2158-5812	1.747	0.41?	1.89	$18.57 \pm 0.04^i$					
CY2201-3201	3.9	0.32	0.83						
HS2209+1914	1.07		1.04	$14.37 \pm 0.02$					
A2213-2652	1.27		1.31	$14.68 \pm 0.3^k$					
Q2237+030	1.69	0.039	1.78	$14.96 \pm 0.06$	MgII	$8.68 \pm 0.36$	$45.79 \pm 0.7$	$2900 \pm 565$	4
					CIV	$8.63 \pm 0.32$	$45.92 \pm 0.7$	$3780 \pm 120$	4
					CIV	$8.67 \pm 0.33$	$45.53 \pm 0.2$	$3960 \pm 9.4$	3
					H $\beta$	$9.08 \pm 0.39$	$45.98 \pm 0.2$	$3800 \pm 1400$	3
					H $\alpha$	$9.38 \pm 0.25$	$45.98 \pm 0.2$	$4800 \pm 600$	3
J2250+2117	1.73		1.89	$18.13 \pm 0.02^i$					
WISE2304-2214	1.42	0.446?	2.19	$19.57 \pm 0.02^i$					
PSJ2305+3714	1.78		2.20	$17.34 \pm 0.01^i$					
PSJ2332-1852	1.49		1.97	$19.24 \pm 0.01^i$					
ULASJ2343-0050	0.787	0.3?	1.32	$20.6 \pm 0.01^r$					
WISEJ2344-3056	1.298	1.30?	2.18	$19 \pm 0.1$					
J2350+3654	2.085		3.31	$20.72 \pm 0.01^i$					

**Notes.** <sup>(a)</sup> Systems with \* are magnitudes from filter F814W. Those with  $i$ ,  $k$  and  $r$  from  $i$ ,  $k$  and  $r$  band respectively. <sup>(b)</sup>  $\log_{10}(M_{BH})$ . <sup>(c)</sup>  $\log_{10}(L_{ref})$ .  $L_{ref}$  = Luminosity ( $L_{1450}$ ,  $L_{3000}$ ,  $L_{5100}$ ,  $L_{5100}$ ) for CIV, MgII, H $\alpha$  and H $\beta$  respectively. <sup>(d)</sup> References of the  $M_{BH}$ : (1) [Peng et al. 2006b](#), (2) [Greene et al. 2010](#), (3) [Assef et al. 2011](#) and (4) [Sluse et al. 2012](#)

## 2.2 Spectroscopic data

The data used in this thesis comes from three instruments: X-shooter (mounted in the Very Large Telescope), LUCIFER (Large Binocular Telescope) and finally MMIRS (*Magellan* 6.5m Clay telescope). The name of the instrument LUCIFER was changed to LUCI in 2012, and MMIRS was used in the *Magellan* telescope from 2010 to 2015 and now is in use at the MMT 6.5-meter telescope on Mount Hopkins, Arizona.

### 2.2.1 X-shooter data

These data was obtained in the programs 103.B – 0566(A) and 106.21DC.001 (PI: A. Melo) using X-shooter spectrograph (Vernet et al. 2011) mounted at the 8.2 m UT2 at the Very Large Telescope (VLT), Paranal Observatory. X-shooter is a medium-resolution spectrograph that observes in a wide spectral range, from ultraviolet (UVB; 3000–5600 Å), through visible (VIS; 5500–10200 Å), and up to the near-infrared (NIR; 10200–24800 Å). In the first run, the UVB slit was  $1.0'' \times 11''$  (spectral resolution  $R = 5400$ ), while the VIS and NIR slits were  $1.2'' \times 11''$  ( $R = 6500$  and  $4300$ , respectively) with a readout mode (UVB and VIS) of 100k/1pt/hg and a nodding of  $3''$  per individual frame. The same configuration was made for the second run, but the UVB slit was  $1.3'' \times 11''$  (spectral resolution  $R = 4100$ ) and a nodding of  $6''$  per individual frame was employed. The atmospheric dispersion corrector (ADC) is used to avoid chromatic differential atmospheric refraction. The slit position was chosen to cover the two brightest source images, centered on the brightest one of the gravitational lensed quasar. Table 2.2 summarizes the main observational characteristics for both runs. In total eight systems were observed, four quadruples and four doubles.

We used the ESO pipeline `EsoReflex` (Freudling et al. 2013) workflow with the X-shooter pipeline version 3.5.0 to reduce each observing block (OB) without using nodding to subtract the sky emission. This method was employed instead of the standard model because the  $3''$  nodding used in the first program was comparable to the image separation, which caused a self-subtraction flux from the lensed quasar spectra. This problem was confirmed in the first system we reduced (WGD2038–4008). Due to this, the next steps in the reduction and extraction were slightly different for the three arms of the instrument. Even though the other systems do not have this problem, the same steps were followed.

---

System	Images	OB	Date	Position angle (degree)
WGD2038–4008	A-B	1	9-10 July 2019	126.8
		2	9-10 July 2019	
		3	10-11 July 2019	
B1152+200	A-B	1	20-21 Jan 2020	143.1
		2	20-21 Jan 2020	
LBQS1333+0113	A-B	1	27-28 Feb 2020	138.4
		2	28-29 Feb 2020	
QJ0158–4325	A-B	1	21-22 Aug 2019	70.9
		2	19-20 Sep 2019	
Q1355–2257	A-B	1	28-29 Feb 2020	-106.4
		2	6-7 Apr 2021	
RXJ1131–1231	A-B	1	23-24 May 2019	1.7
		2	08-09 June 2019	
HE0230–2130	A2-B	1	12-13 Dec 2020	17.7
		2	20-21 Dec 2020	
		3	08-09 Feb 2021	
WISE0259–1635	A-C	1	15-16 Jan 2021	111.7
WISE0259–1635	B-D	1	18-19 Jan 2021	17.4
		2	06-07 Feb 2021	

TABLE 2.2: Summary of X-shooter observations for proposals 103.B – 0566(A) and 106.21DC.001.

Once the frames were corrected by cosmetics (flat field, dark current, wavelength calibration, among others), we proceeded to subtract the sky emission in the NIR arm. We designed a sky emission correction for each individual frame based on principal component analysis (PCA, [Deeming 1964](#), [Bujarrabal et al. 1981](#), [Francis & Wills 1999](#)), a method normally employed in multi-dimensional analysis. PCA uses a basis of eigenvectors that are constructed to describe the data (e.g., by maximizing the variance of the projected data). This method is usually applied to reduce the number of parameters describing a data set by computing the principal components to change the representation of the data. The number of components for the reconstruction was chosen to minimize the standard deviation of the residuals between the spectrum and all sky models (using a different number of components).

The procedure to obtain the best representation of the underlying sky emission in each frame consists of the following steps. First, we masked the outliers (such as bad pixels) applying  $\sigma$ -clipping ( $\sigma=5$  with three iterations), replacing them with an estimated value obtained from a bicubic interpolation using the surrounding pixels. Then, we calculated the median for each wavelength bin to get a rough approximation of the sky emission as a function of the wavelength. We note that this value is only used to identify the targeted spectra (quasar lensed images A and B, as well as the lens galaxy). We subtracted this rough sky

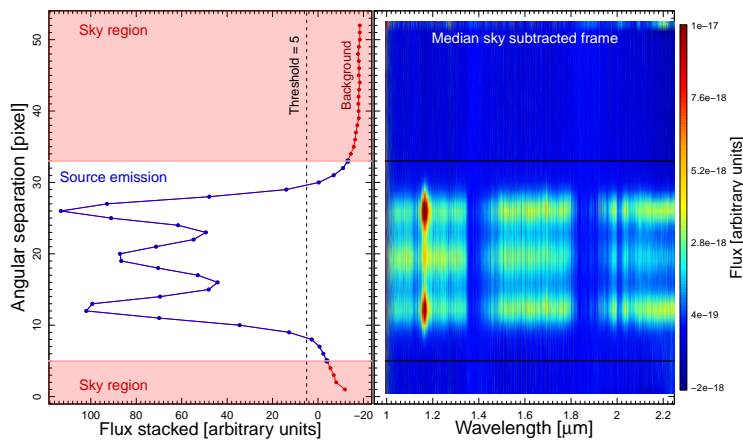


FIGURE 2.1: Two-dimensional spectra for WGD2038-4008. *Left*: Collapsed frame along the wavelength axis after the subtraction of the sky median. The pink shaded zone represent the sky region (see text). *Right*: NIR frame after sky subtraction.

median from each frame and collapsed the remaining 2D spectra along the wavelength (see Figure 2.1 right and left, respectively) to select an uncontaminated spatial region for the sky emission. A threshold equal to 3 pixels, above and below the dispersion of the median, above the background (see Figure 2.1, left) is applied to choose the region to be employed as the PCA-basis (normalized to the unit). The PCA eigenvector basis is obtained by constructing a model of the sky emission in the selected spatial region. This 2D sky model is then subtracted from the frame.

Flux calibration is done by using the equation given in the X-shooter Pipeline User Manual<sup>2</sup>:

$$I [\text{erg/s/cm}^2/\text{\AA}] = \frac{I[\text{ADU/pixel}[\text{\AA}]] \times \text{Response}[\text{erg/e}^-/\text{cm}^2] \times 10^{(0.4 \cdot \text{airmass} \cdot \text{ext})}}{\text{gain}[\text{ADU/e}^-] \times \text{Exptime}[\text{s}] \times \text{bin\_size}} \quad (2.1)$$

where  $I$  is the FITS file, the *ext* comes from the atmospheric extinction tables provided by the pipeline, and the *gain*, *Exptime*, *bin\_size* and *airmass* from the header of the FITS files. The *response* is obtained from the end-products of the X-shooter pipeline from a standard star observed the same night as the target.

After the sky modeling, subtraction and flux calibration, we employed *molecfit* (Smette et al. 2015, Kausch et al. 2015) in each frame of the NIR to correct by telluric absorptions. *Molecfit* is a software based on fitting synthetic transmission spectra to astronomical data

<sup>2</sup><https://ftp.eso.org/pub/dfs/pipelines/instruments/xshooter/xshoo-pipeline-manual-3.5.3.pdf>

so that we can correct the data for atmospheric absorption features. In order to prepare our data and run `Molecfit`, the target spectra for each frame were median-combined into a single spectrum in order to increase the signal and decrease the noise. The spatial region occupied by the targets was previously calculated during the PCA sky emission estimation, and corresponds to the source emission region in Figure 2.1. `Molecfit` follows a plan of six steps (`Molecfit User Manual`<sup>3</sup>):

- Scaling of the continuum.
- Wavelength and resolution fit.
- Rescaling of the continuum.
- Fitting of the molecules.
- Joint continuum, wavelength, and resolution fit.
- Fit of all components (molecules, continuum, wavelength, and resolution).

For the parameters setup and the fitting of the molecules, I used the values given in [Kausch et al. 2015](#) (Table 3 and 4), who applied `molecfit` to X-shooter spectra. The best fit was applied to each frame row by row.

Once the frames were corrected by sky emission and telluric absorption, they were median combined and the uncertainties estimated as the median absolute deviation. All the parameters required for the stacking (e.g., dithering, pixel scale) were obtained from the header of each frame, modified by the X-shooter workflow. Figure 2.2 shows the result of the final 2D spectrum (top panel) compared to that obtained as end-product from the ESO pipeline (bottom panel). The bottom image shows the self-subtraction flux from the lensed quasar spectra due to the small nodding (3 arcsec) of the program.

In contrast to the NIR, the VIS observations are not dominated by the sky brightness. Therefore, instead of the PCA analysis, we used the median of each sky region as the best representation of the sky brightness, obtained in the same way as for the NIR (i.e., selecting a region free of source emission to compute the sky brightness value). The flux calibration, telluric correction, and combination of frames are done in the same way as for the NIR arm.

---

<sup>3</sup>[https://ftp.eso.org/pub/dfs/pipelines/skytools/molecfit/VLT-MAN-ESO-19550-5772\\_Molecfit\\_User\\_Manual.pdf](https://ftp.eso.org/pub/dfs/pipelines/skytools/molecfit/VLT-MAN-ESO-19550-5772_Molecfit_User_Manual.pdf)

---

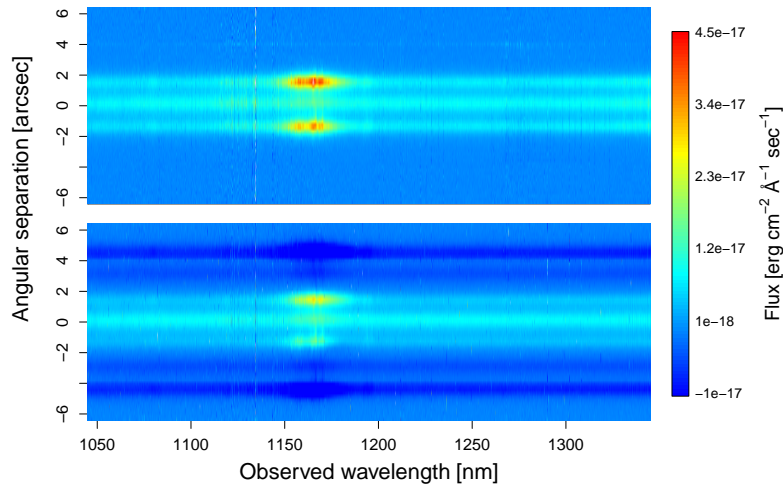


FIGURE 2.2: Final 2D NIR spectrum for WGD2038-4008 using the PCA sky extraction described in Sect. ?? (top) compared to the one using ESO pipeline reduction (bottom). Both spectra are flux calibrated and telluric corrected.

Even though the UVB arm does not require sky subtraction, we used the same procedure as the VIS arm to be consistent with the reduction.

### 2.2.1.1 One-dimensional extraction

To obtain uncontaminated spectra between the quasar images and the lens galaxy, I proceeded as follows. First, I collapsed the 2D reduced spectrum along the wavelength axis in a high signal-to-noise (S/N) region, for example around an emission line region ( $H\alpha$  in the NIR, OIII in VIS, and MgII in the UVB arm, it depends on the redshift of the lensed quasar). In the case of the VIS and UVB arms, I selected bins of 20 pixels ( $4 \text{ \AA}$ ) to increase the S/N of the sources. I masked the outliers (persistent bad pixels, poor sky subtraction, and/or low S/N regions) to obtain the best-fit parameters as a function of the wavelength. The spatial contribution of each component was estimated by simultaneously fitting two Gaussian profiles as seen in Figure 2.3 (three if the lensed galaxy was observed in the collapsed 2D reduced spectrum). If three Gaussians were needed, the distances between image  $A$  and  $B$  and between image  $A$  and the lens galaxy projection onto the  $AB$  segment (the distances were obtained from the astrometry in CASTLES and from [Shajib et al. 2019](#)) were used to fix the position of the Gaussian centers for  $B$  and the lens galaxy, respectively. Assuming  $A$  and  $B$  are point sources, we can consider that they have the same FWHM and standard deviation parameter ( $\sigma$ ). A variable  $\sigma_l$  (larger than  $\sigma$ , due to extended emission) is used for

the lensing galaxy if its present. The  $\sigma_l$  will vary due to the extended or faintness of the lens galaxy in each arm. The free parameters are the amplitudes, image  $A$  center,  $\sigma$  for the point sources, and  $\sigma_l$  for the lens galaxy. The  $\sigma$  and  $\sigma_l$  used for each system are presented in Table 2.3. The best-fit estimated values and their respective uncertainties are applied to construct a probability function for the spatial distribution of each target (quasar images and lens galaxy if present), allowing us to identify the probability that a given spatial pixel belongs to one of the targets. A probability density function is a function that tell us a relative likelihood that a value of a variable could be close o that sample. An example is shown in figure 2.4, where one pixel of the 2D reduced spectrum of WGD2038-4008 (upper image in figure 2.4) is shown along with the Gaussians that are used for the extraction. The bottom image shows the probability function that one pixel would could have in the regions where the Gaussian are. I used error propagation for each free parameter to estimate the related uncertainties in each final uncontaminated spectrum.

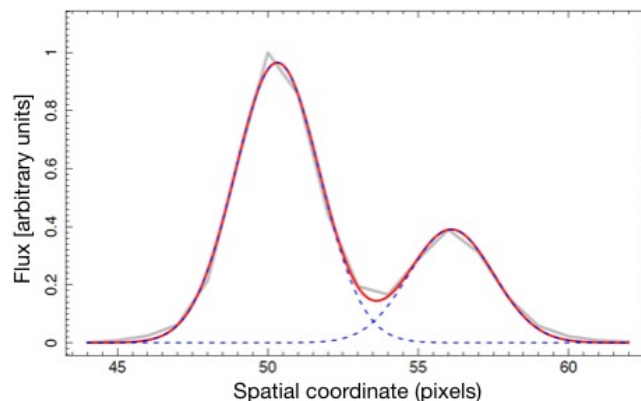


FIGURE 2.3: Gaussian fit (red line) in the collapsed 2D reduced spectrum along the wavelength axis (grey line) of the system Q1355-2257 in the NIR arm. The dashed blue line represents the two Gaussian functions for the two images of the system. No lensing galaxy is present in this case.

System	UVB		VIS		NIR	
	$\sigma$	$\sigma_l$	$\sigma$	$\sigma_l$	$\sigma$	$\sigma_l$
WGD2038-4008	2.9	3.1	2.4	3.9	1.6	-
LBQS1333+0113	2.4	-	2.3	-	1.3	-
QJ0158-4325	2.77	-	2.43	-	1.7	-
Q1355-2257	2.31	-	2.14	-	1.4	-

TABLE 2.3: Best fit for the standard deviation parameter used in each system for the extraction of the images and lensing galaxy (if it is present).

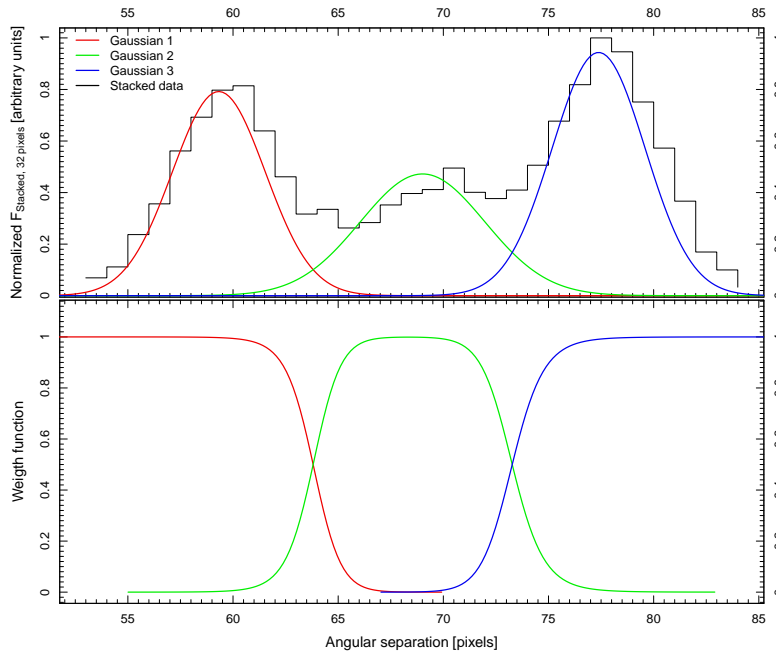


FIGURE 2.4: One pixel of the reduced 2D spectrum of the the Gaussian fitting in WGD2038-4008 (upper image), along with its probability function (bottom image).

TABLE 2.4: Estimated percentage of the flux loss for the systems in each arm.

System	UVB arm (%)	VIS arm (%)	NIR arm (%)
WGD2038-3008	30.5	14.9	19.74
QJ0158-4325	27	11	15
Q1355-2257	19	7	8
LBQS1333+0113	20	9	6

### 2.2.1.2 Flux loss and luminosity estimations

Considering the seeing variation along the wavelength range and the selected slit width in both runs, we need to estimate the percentage of flux loss that each system will have (see Figure 2.5). I estimated the broadening of the spectra profile due to the instrumental dispersion at different wavelengths by fitting a Gaussian function for each wavelength bin of the telluric standard star of each system. This value is employed to calculate the percentage of flux entering the slit by simulating the system as a sum of the Gaussian functions and sigma obtained from the header and integrating it within the slit using the seeing delivered in the header. The percentage of flux lost for each system can be seen in Table 2.4 and it is included as an extra flux error in all our analyses.

I corrected the spectra for galactic reddening using `IrsaDust`<sup>4</sup> in Python language. Using the

<sup>4</sup><https://irsa.ipac.caltech.edu/applications/DUST/>

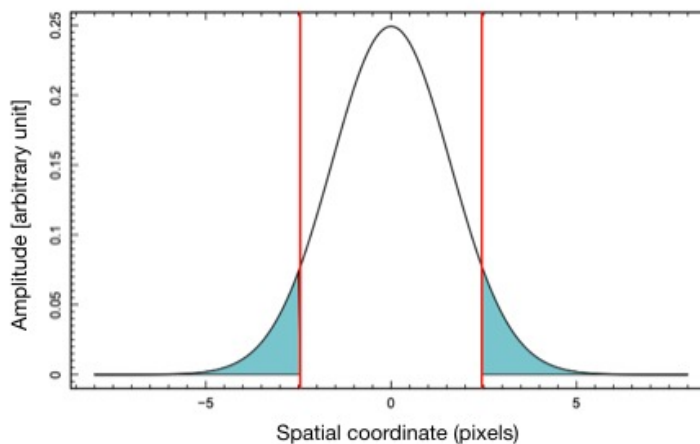


FIGURE 2.5: Example of flux loss in a Gaussian Function of  $\sigma = 1.6$  pixels. The red lines is the NIR slit width and in blue the flux loss due to this sigma.

Right Ascension and Declination of the lensed quasar, the function fetches the Galactic dust reddening for the line of sight and returns the extinction table.

To convert from flux to luminosity I used the equation that is related to the luminosity distance  $d_L$  assuming a flat  $\Lambda$  cold dark matter cosmology with:  $\Omega_\Lambda = 0.7$ ,  $\Omega_M = 0.3$  and  $H_0 = 70 \text{ kms}^{-1} \text{ Mpc}^{-1}$  (throughout this thesis I will assume this cosmological parameters)

$$F = \frac{L}{4\pi d_L^2(1+z)} \quad (2.2)$$

The final spectra of each system can be seen in appendix B.

### 2.2.2 LUCIFER data

Reduced and extracted spectra was provided by R. Assef (private communication) to obtain the  $M_{BH}$  for the systems: HE0047-1756, HE0435-1223, SDSS0924+0219 and Q1017-207. The systems were observed with the Large Binocular Telescope (LBT) using the Near Infrared Spectroscopic Utility with Camera and Integral Field Unit for Extragalactic Research (LUCIFER; Seifert et al. 2003), a near-infrared spectrograph with an spectral range of  $0.85\text{--}2.5 \mu\text{m}$  the 24th and 25th of November of 2012. The systems were observed in the longslit mode using the gratings 200\_H+K (with a resolving power of 1881 at H and 2573 at K) and 210\_ZJHK (resolving power of 6877, 8460, 7838 and 6687 at z, J, H and K respectively) with a  $0.5''$  wide slit. The camera used was N1.8 that had a pixel scale of  $0.25''/\text{pix}$ . The seeing estimated is in average  $\sim 0''.8$ . Table 2.5 summarizes the main observational characteristics

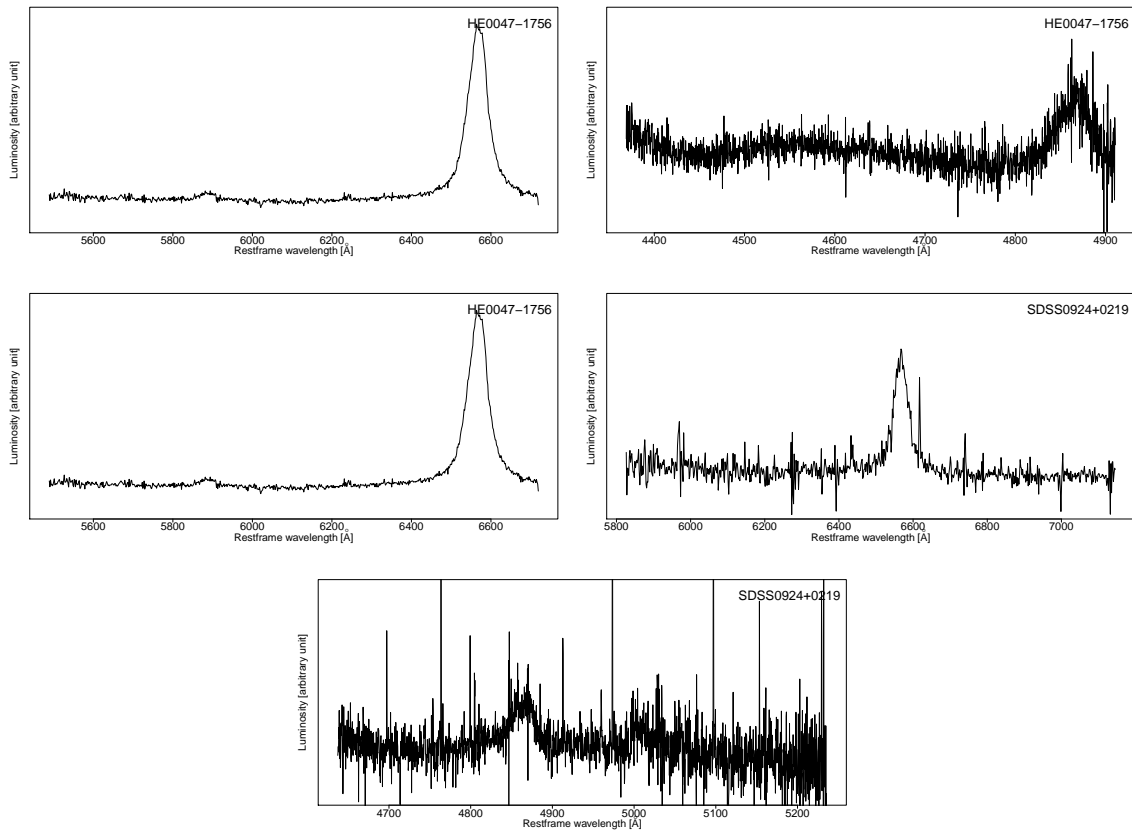


FIGURE 2.6: Spectra of the three lensed quasars observed with LUCIFER instrument.

for the observing runs, image(s) observed of the lensed quasars and the orientation of the slit. Figure 2.6 shows the spectra for the lensed systems observed with LUCIFER.

Data reduction was performed using IRAF packages along with IDL task `xtellcor_general` from Vacca et al. (2003) for the telluric absorption correction. The detailed reduction is described in Assef et al. 2011, but I will mention the most general steps. For each exposure, a two-dimensional wavelength calibration was performed using the sky emission lines and a combined median sky frame was built. This sky frame was used to remove the sky before extracting the spectra. After correcting for the telluric absorptions using `xtellcor_general`, the flux calibration was made covolving the spectrum with the F160W filter curve from HST and matching it to the de-magnified absolute magnitude of the quasar obtained from the CASTLE website (Assef et al. 2011). The flux to luminosity conversion was made following section 2.2.1.2, using the luminosity distance and the redshift for each system. Finally, the de-magnification was made using the magnifications presented in section 3.1.

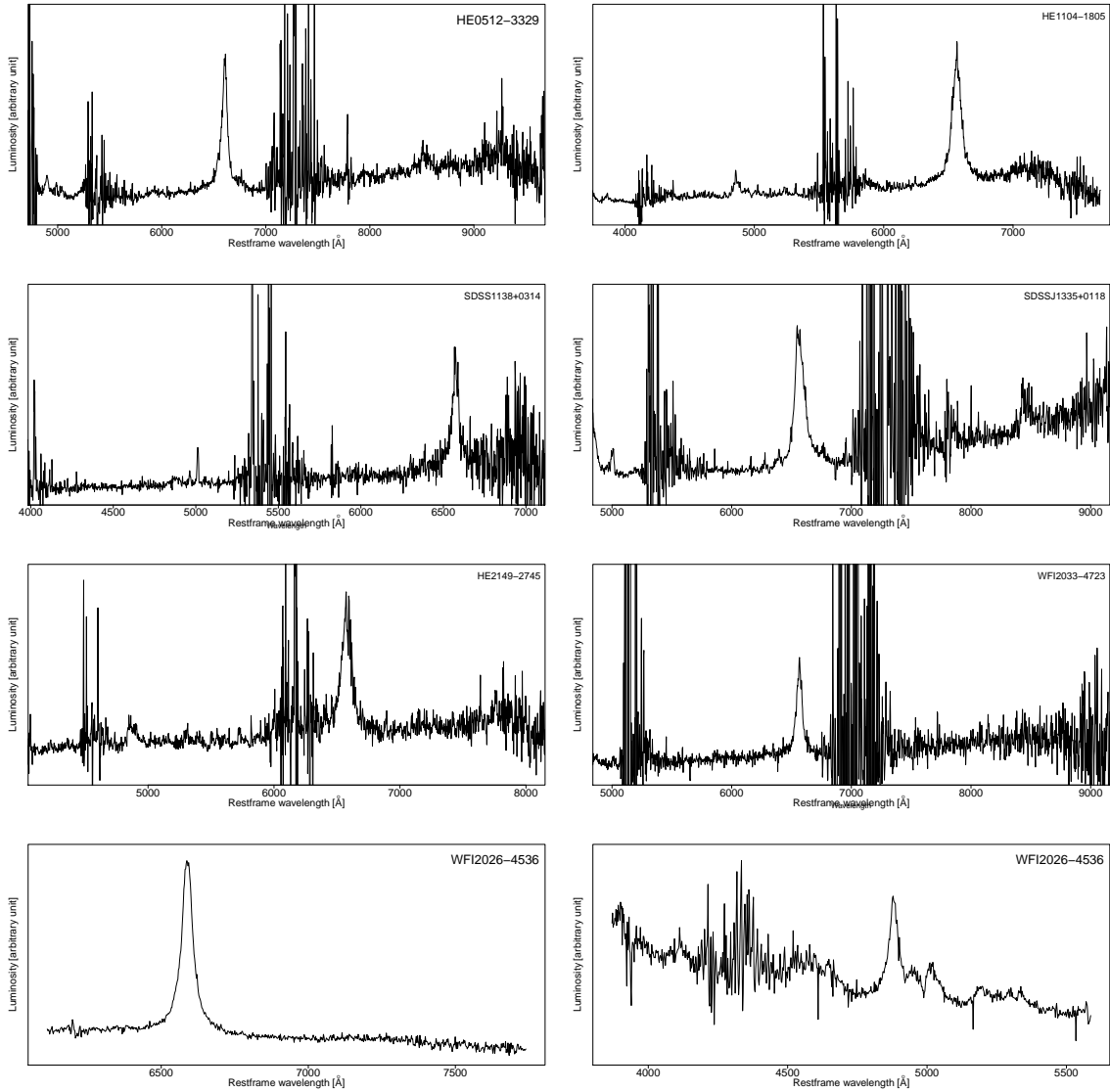


FIGURE 2.7: Spectra of the seven lensed quasars observed with MMIRS instrument.

TABLE 2.5: Observations of LUCIFER and MMIRS data.

Object	Date (dd-mm-YYYY)	Date (MJD)	Exp. time (s)	Image(s)	S/N	Filter	Inst.
HE0047-1756	25-11-2012	56 256	120	A	17.97	HKspec	LUCIFER
HE0047-1756	25-11-2012	56 256	120	A	3.49	J	LUCIFER
HE0435-1223	27-11-2012	56 258	120	A	7.07	HKspec	LUCIFER
HE0512-3329	06-04-2012	56 024	180-300?	A-B	10.42	HK	MMIRS
SDSS0924+0219	24-11-2012	56 255	120	A	5.11	HKspec	LUCIFER
SDSS0924+0219	24-11-2012	56 255	600	A	4.05	J	LUCIFER
HE1104-1805	07-04-2012	56 025	180-300?	A-B	11.97	HK	MMIRS
SDSS1138+0314	06-04-2012	56 024	180-300?	A-B	4.02	HK	MMIRS
SDSSJ1335+0118	07-04-2012	56 025	180-300?	A-B	8.36	HK	MMIRS
WFI2026-4536	06-11-2012	56 238	180	A-B	12.72	HK	MMIRS
WFI2033-4723	06-04-2012	56 024	180-300?	C-A2	5.84	HK	MMIRS
HE2149-2745	06-04-2012	56 024	180-300?	A-B	12.83	HK	MMIRS

### 2.2.3 MMIRS data

Seven lensed systems were observed using MMT and Magellan Infrared Spectrograph (MMIRS; [McLeod et al. 2012](#)), a near-IR imager and multi-object spectrograph mounted in the *Magellan* 6.5m Clay telescope in Chile. MMIRS data (provided by E. Falco, private communication) were observed on 2012 April 6 and 7 using the long-slit data in HK band at the wavelength range 1.25-2.4  $\mu\text{m}$ . Two images of the lensed quasar were positioned in a slit of 0.8'' wide with a pixel scale of 0.2012 arcsec/pix<sup>5</sup>. The observations were taken with nodding to correct for the thermal emission from the sky background.

Data reductions were carried out with the data reduction pipeline [Chilingarian et al. 2015](#) and IRAF tasks. The code `mmfixall`, provided by the MMIRS instrument scientific team, was used to collapse the information contained in the multi-extension files. The remaining procedure was performed in IRAF and consisted on dark correction, sky subtraction, 1D spectra extraction, wavelength calibration and telluric correction. The 1D spectra was extracted using the `apall` task with apertures of  $\pm 3 - 4$  pixels. Flux calibration was carried out using `xtellcor_general` for telluric lines absorption corrections and then converted to luminosity (section 2.2.1.2).

---

<sup>5</sup><https://lweb.cfa.harvard.edu/mmti/mmirs/instrstats.html>

---

# Chapter 3

## Methods

In this chapter I present the methods used to obtain the magnification values, the  $M_{BH}$  estimation and the accretion disk size.

### 3.1 Gravitational lens model

To resolve the lens equation we must assume a mass distribution to reproduce the position of the images. To do this, there are different softwares to model a gravitational lens system: `Lensmodel` (Keeton 2001, Keeton & Zabludoff 2004), `LENSTRONOMY` (Birrer & Amara 2018, Birrer et al. 2021), `GLEE` (Suyu & Halkola 2010, Suyu et al. 2012), `AutoLens` (Nightingale et al. 2018), `LENSED` (Tessore et al. 2016), `visilens` (Spilker et al. 2016), among others. They can be divided as *forward* or *reverse*. In the *forward* the images are predicted based on a known lensing mass and source, while the *reverse* use the observed images to reconstruct a model of the mass density (Lefor et al. 2013) and find the position of the source. In general, the *reverse* method is used, and it follows the same steps in each software but using different methods. I will describe the gravitational lens modeling made by Keeton 2001. This software was chosen since it uses the most simplest model and it satisfies my need to obtain the convergence ( $\kappa$ ) and shear ( $\gamma$ ) needed to demagnify the spectra.

`Lensmodel` requires a cosmological model setup for the simulations (cosmological parameters input  $\Omega_m \approx 0.7$  and  $\Omega_\Lambda \approx 0.3$ ). The input parameters are the redshift of the source ( $z_s$ ) and the lens ( $z_l$ ), the position and fluxes of the images along with their uncertainties. The flux uncertainty was chosen to be 20% due to the possible existence of microlensing effect

System	$\mu_A$	$\mu_B$	$\mu_C$	$\mu_D$	Distribution	Software	Reference
WGD2038-4008	$2.27 \pm 0.21$	$2.71 \pm 0.32$	2.04	0.93	SIE + $\gamma$	Lenstronomy	<a href="#">Shajib et al. 2019</a>
LBQS1333+0113	3.77	0.87	-	-	SIS	Lensmodel	<a href="#">Sluse et al. 2012</a>
QJ0158-4325	25.27	12.31	-	-	SIS		<a href="#">Bhatiani et al. 2019</a>
Q1355-2257	2.50	0.85			SIS	Lensmodel	<a href="#">Sluse et al. 2012</a>
RXJ1131-1231	-	11.6	-	-	SIE + $\gamma$	Lensmodel	<a href="#">Sluse et al. 2012</a>
WISE0259-1635	5.82	3.46	3.57	3.41	SIE + $\gamma$	Lenstronomy	<a href="#">Shajib et al. 2019</a>
HE0047-1756	13.78	3.10	-	-	SIS	Lensmodel	<a href="#">Sluse et al. 2012</a>
HE0435-1223		6.46		4.21	SIE + $\gamma$	Lensmodel	<a href="#">Sluse et al. 2012</a>
SDSS0924+0219	26.2	-	-	-	SIS	Lensmodel	<a href="#">Keeton et al. 2006</a>
HE1104-1805	16.2	2.3	-	-	SIE + $\gamma$	Lensmodel	<a href="#">Assef et al. 2011</a>
SDSS1138+0214		4.53	6.24		SIE + $\gamma$	Lensmodel	<a href="#">Sluse et al. 2012</a>
SDSSJ1335+0118	3.77	0.87	-	-	SIS	Lensmodel	<a href="#">Sluse et al. 2012</a>
WFI2026-4536	14.20	12.5	-	-	SIE + $\gamma$	Lensmodel	<a href="#">Bate et al. 2018</a>
WFI2033-4723		3.13	4.11		SIE + $\gamma$	Lensmodel	<a href="#">Sluse et al. 2012</a>
HE2149-2745	2.71	0.66	-	-	SIS	Lensmodel	<a href="#">Sluse et al. 2012</a>

TABLE 3.1: Magnification values used for demagnifying the luminosity of each image. Errors are added if it exists in the lens model.

(e.g., [Bogdanov & Cherepashchuk 2004](#), [Motta et al. 2012](#)). The quasar positions and fluxes can be obtained from the astrometry and photometry of CASTLES. The systems can be modeled using a SIS, SIE, or SIE +  $\gamma$  lens mass distributions, and are defined through the parameters: RA and DEC coordinates of the center of the lens, mass scale, ellipticity and its position angle, the external shear and angle of the external shear (see [Keeton 2001](#)).

The output file contains the best fit for the model together with the chi square value, the positions, the flux of the source, and finally  $\kappa$  and  $\gamma$ . The goodness  $\chi^2$  of a model will be:

$$\chi_{lens}^2 = \sum_i \frac{||\Theta_i - \Theta_{0,i}||^2}{\delta_{\Theta_i}^2}, \quad (3.1)$$

where  $\Theta_i$  is the model-predicted positions of the  $i$ th images,  $\Theta_{0,i}$  the observed position and  $\delta_{\Theta_i}^2$  their observed positional uncertainty. Finally, to obtain the magnification factor ( $\mu$ ) we use the equation ([Narayan & Bartelmann 1996](#)):

$$\mu = \frac{1}{(1 - \kappa)^2 - \gamma^2}. \quad (3.2)$$

Table 3.1 shows the magnification of each image of the systems used in this thesis with the software and model the authors used.

### 3.2 Black hole mass (MBH)

The black hole mass is estimated by using the SE method (e.g., [McLure & Dunlop 2004](#), [Shen et al. 2008](#), [Trakhtenbrot & Netzer 2012](#)), which combines the Doppler line width of the broad emission line and the monochromatic luminosity to obtain a proxy for  $M_{BH}$ . If we assume that the emitting gas in the BLR is virialized, then

$$M_{BH} = f R_{BLR} (\Delta v)^2 G^{-1}, \quad (3.3)$$

where  $G$  is the gravitational constant,  $R_{BLR}$  is the BLR size,  $\Delta v$  is the velocity of the line emitting gas in the BLR, and  $f$  is the virial factor that depends on the unknown structure, kinematics, inclination, and distribution of the BLR ([Peterson et al. 2004](#) and references therein). The BLR size comes from the RM and from the known correlation between the AGN luminosity and the size of the BEL,  $R_{BLR} \sim (\lambda L_\lambda)^\alpha$  (mentioned in section 1.3), allowing us to estimate  $M_{BH}$  as:

$$\begin{aligned} \log(M_{BH}) &= \log(K) + \alpha \log\left(\frac{\lambda L_\lambda}{10^{44} \text{ erg/s}}\right) \\ &+ 2.0 \log\left(\frac{FWHM}{1000 \text{ km/s}}\right), \end{aligned} \quad (3.4)$$

where  $K = G^{-1}f$ ,  $\lambda L_\lambda$  is the monochromatic luminosity and  $FWHM$  is the full width at half maximum of the broad emission line. The literature shows different values for the parameters  $K$  and  $\alpha$  ([McLure & Dunlop 2004](#), [Vestergaard & Peterson 2006b](#), [Vestergaard & Osmer 2009](#), [Shen et al. 2011](#)), although we use those estimated by [Mejía-Restrepo et al. 2016](#) because they were estimated using a similar setup to our observations, thus minimizing the systematic effects. In particular, the sample of [Mejía-Restrepo et al. 2016](#) contains several emission lines for each object; in addition, all the lines for a single object were observed simultaneously. The values for the parameters used for the emission lines ( $H\alpha$ ,  $H\beta$ ,  $MgII$  and  $CIV$ ) at their respective luminosities ( $L_{5100}$ ,  $L_{5100}$ ,  $L_{3000}$  and  $L_{1450}$ ) are

$$(\log K, \alpha)_{H\alpha} = (6.845, 0.650),$$

$$(\log K, \alpha)_{H\beta} = (6.740, 0.650),$$


---

$$(\log K, \alpha)_{MgII} = (6.925, 0.609).$$

$$(\log K, \alpha)_{CIV} = (6.353, 0.599).$$

In addition to the usual uncertainties related to the SE method (FWHM, luminosity, and  $f$  parameter estimations), the observed source luminosity also needs to be corrected for the lensing magnification, which were obtained for each system from a lens model (section 3.1).

### 3.2.1 Emission line fitting and luminosity measurement

After demagnifying the spectra, and removing the continuum and the iron template (following [Mejía-Restrepo et al. 2016](#)), I modeled each emission line profile and estimated the BEL FWHM. I used Gaussian functions to represent the broad and narrow components of each emission line (see Appendix A) and masked those regions affected by absorptions (e.g. WGD2038-4008<sup>1</sup>). In the H $\alpha$  region four extra Gaussian components were added for the [N II] and [S II] narrow-line region (NLR) doublets. In the H $\beta$  region we considered two extra Gaussians for the [O III] NLR doublet and one for the He II broad emission line and for the Mg II region two narrow and two broad components. The FWHM used for the  $M_{BH}$  measurement was obtained by adding the Gaussians of a line (i.e., the resulting profile is the combined Gaussians representing the broad line components) and then numerically calculated it. The uncertainties were obtained using error propagation and a Monte Carlo simulation of 1000 random resamplings, assuming a Gaussian distribution for the flux uncertainty at each pixel. The best line fit is shown in red (e.g. Figure 4.3 for WGD2038-4008).

The monochromatic luminosity was measured using continuum windows on each side of the emission line ([4670 : 4730 , 5080 : 5120] Å for H $\beta$ , [6150 : 6250 , 6800 : 6900] Å for H $\alpha$ , [2650 : 2670 , 3030 : 3070] Å for Mg II, [1680 : 1720 , 1960 : 2020] Å for C III and [1420 : 1460 , 1680 : 1720] Å for C IV)<sup>2</sup>. These spectral windows were selected for the low (or even null) emission line contamination levels, and were used to interpolate the region of interest following a single power-law function.

For the low S/N spectra that some systems have and for the UVB arm of the WGD2038-4008 (due that the ADC did not work) we used an AGN spectral energy distribution (SED)

<sup>1</sup>We should point out that we also considered other line profile fittings: i) Gaussian fitting without masking regions, ii) the addition of Gaussian profiles for the absorption features. Although both methods provide FWHM that are consistent with our results, the first one yields larger residuals and the last one introduces overfitting.

<sup>2</sup>These are the common windows used, but it could vary for each system if telluric absorptions are near these regions.

template from [Assef et al. 2010](#) (low resolution templates or LRT). The SED is modeled by a linear combination of three spectral templates: one similar to an spiral galaxy, another similar to an elliptical galaxy, the third one similar to an irregular galaxy, plus an AGN contribution. The brightest image (image A) was used to fit the SED for each system with the unmagnified quasar magnitudes (see table 3.1 for the magnification). The magnitudes were obtained from the Hubble Space Telescope (HST) data in the V (F555W), I (F814W) and H (F160W) broad bands obtained by the CfA-Arizona Space Telescope LEns Survey (CASTLES<sup>3</sup>; [Falco et al. 2001](#)). In addition, data from GAIA DR2 (<https://research.ast.cam.ac.uk/lensedquasars/>) and some other filters from different observations were used in the fitting of the SED. I chose magnitudes that were close in time to avoid differences due to microlensing or intrinsic variation of the AGN. Before the fitting, the magnitudes were converted to flux using the equation  $F_{\nu}[Jy] = (F_{\nu 0} \times 10^{-m/2.5})/M$ , where  $F_{\nu 0}$  is the zero point of the filter (normally in Vega magnitude) obtained from the Filter Profile Service (<http://svo2.cab.inta-csic.es/svo/theory/fps3/>),  $m$  is the apparent magnitude and  $M$  is the magnification of the image. A SED example using LRT can be seen in Figure 3.1. The final result of the fitting provides the monochromatic luminosity at the wavelength required for the  $M_{BH}$  mass. The errors were obtained using a Monte Carlo method. I repeated the sampling along the photometric uncertainties 1.000 times and the SED fitting and parameters are recalculated. The best SED obtained was the one that had lower  $\chi^2$ , and with the 1.000 generated parameters I created histograms for each of them to obtain their distribution properties.

### 3.3 Microlensing analysis

Microlensing can induce flux variations in the quasar images due to lensing from stars in the lensed galaxy halo (e.g., [Chang & Refsdal 1979](#), [Schneider 2006](#)). The flux variation by microlensing in one or more images is sensitive to the angular size of the source, meaning that the magnification will be larger for a smaller emitting region (See section 1.2.6).

In this situation, I could study the inner structure of the lensed systems from the SE images of different observations, where the accretion disk and BLR can be affected differently by microlensing and could affect the wings of the profile in broad emission lines ([Popović et al.](#)

---

<sup>3</sup><https://lweb.cfa.harvard.edu/castles/>

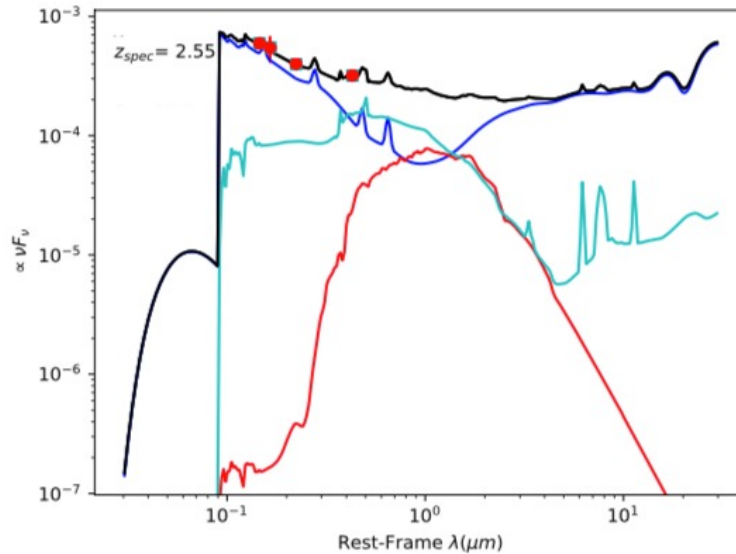


FIGURE 3.1: rest frame wavelength vs flux SED for the system Q1017-207. The lines represent the contribution of the AGN (blue), elliptical galaxy (red) and irregular galaxy (cyan). The best fitting combination is represented by the black line.

2001, Abajas et al. 2002, Lewis & Iбата 2004). On the contrary, the NLR is insensitive to microlensing and can be used as the baseline for no microlensing (Abajas et al. 2002).

To investigate whether microlensing is present, I used the magnitude difference between the emission line core and the continuum (see Moustakas & Metcalf 2003, Mediavilla et al. 2009, 2011, Motta et al. 2012, Guerras et al. 2013, Motta et al. 2017, Rojas et al. 2020). A quasar's emission lines come from several components (see sec. 1.1), meaning that they are produced over a large distance from the central continuum (e.g. Sulentic et al. 2000). The line core is dominated by the NLR, while the wings are dominated by the BLR emission. Following Mediavilla et al. 2009 (e.g. also Blackburne et al. 2011, Mediavilla et al. 2011, Motta et al. 2012, Rojas et al. 2014, and therein), the method we used is based on integrating small regions (from several to tenths of Angstroms) in the core and the wings of the emission line for the NEL and BEL, respectively. According to Marziani et al. 2019,  $H\beta$  and CIV profiles are associated with two sub-regions within the BLR (e.g. Hall et al. 2003, Leighly & Moore 2004, Plotkin et al. 2015): one emitting predominantly low ionization lines (LILs, e.g. Matsuoka et al. 2008) and another emitting high-ionization lines (HILs), associated with gas outflows and winds (e.g. Richards et al. 2011, Yong et al. 2018). The LILs and the core of the HILs could have a FWHM  $\sim 500\text{-}5000 \text{ km s}^{-1}$  that could be insensitive to microlensing, while the broad wings could have FWHM  $\sim 10.000 \text{ km s}^{-1}$  and is meant to represent the innermost part of the BLR, prone to microlensing (Marziani et al. 2019). Since both of them are part

of the BLR, we follow the work by other authors who have used this method of microlensing (see e.g., [Mediavilla et al. 2011](#), [Motta et al. 2012](#), [Rojas et al. 2014, 2020](#)) and use small integrated regions in the core of the emission lines that will be dominated by the NLR and the outer regions for the BLR. In addition, the light of each image follows a different path through the lens galaxy where gas and dust can produce extinction. Microlensing can be separated from extinction considering that the latter will affect both the continuum flux ratio and the core of the emission line ([Falco et al. 1999](#), [Motta et al. 2002](#), [Mediavilla et al. 2005](#)).

I obtained the magnitude difference between components in the continuum by fitting a straight line ( $y = a\lambda + b$ ) between two regions on each side of each emission line (e.g., [Motta et al. 2012](#)). The regions are  $\sim 30 - 100 \text{ \AA}$  in size and uncontaminated of emission lines (and/or tellurics) following the parameters in appendix A. I integrated the line between the two regions (total wavelength range from  $\lambda_A$  to  $\lambda_B$ ) to obtain the continuum flux for both images. This continuum is then subtracted from the spectrum and we integrate a small window (between 10-30  $\text{\AA}$ ) centered in the emission line core to obtain the flux uncontaminated by the continuum. The intervals are defined according to [Guerras et al. 2013](#) (see also [Fian et al. 2018](#)), in which the cores of emission lines are centered in the peak of the line and have a narrow interval of  $\sim \pm 6 \text{ \AA}$  while the wings have a wavelength interval of  $\sim \pm 30 \text{ \AA}$ . Integrating in the core of the emission line decreases the BEL contamination that can also be affected by microlensing. The integration is made following the Trapezoidal rule, which uses trapezoids to approximate the area under a function:

$$\int_{\lambda_A}^{\lambda_B} f(x) dx = (\lambda_B - \lambda_A) \cdot \frac{1}{2} (f(\lambda_A) + f(\lambda_B)) \quad (3.5)$$

The uncertainty of the flux is assumed to be related to the continuum fitting and is obtained using error propagation, where the square root of the error in the spectra and the straight line are added in quadrature. Finally, the magnitude difference between image A and B for each region (continua and line cores) is  $m_A - m_B = -2.5 \log(F_A/F_B)$ , obtaining a  $(m_A - m_B)^{\text{line}}$  for the core of the emission line and a  $(m_A - m_B)^{\text{cont}}$  for the continuum e.g., [Guerras et al. 2013](#)).

### 3.4 Accretion disk size estimation

We will use two methods to infer the accretion disk size ( $r_s$ ): the first one is based on the estimated  $M_{BH}$  and the second one employs simulations when chromatic microlensing is present. In the first method, we use the  $M_{BH}$  estimation and we can use the equation by [Mosquera & Kochanek 2011](#):

$$r_s = 9.7 \times 10^{15} \left( \frac{\lambda_{rest}}{\mu m} \right)^{4/3} \left( \frac{M_{BH}}{10^9 M_\odot} \right)^{2/3} \left( \frac{L}{\eta L_E} \right)^{1/3} \text{ [cm]}, \quad (3.6)$$

where,  $\lambda_{rest}$  is the wavelength where the  $M_{BH}$  is measured,  $\eta$  is the accretion efficiency, and  $L/L_E$  the luminosity in units of the Eddington luminosity. For a typical accretion rate  $\eta = 0.1$  and  $L/L_E \sim 1/3$  (e.g., [Hopkins & Hernquist 2009](#), [Schulze & Wisotzki 2010](#)), the flux sizes are smaller than the theoretical sizes (e.g., [Collin et al 2002](#)).

For the second method, I need to investigate whether chromatic microlensing is present in the systems. this characteristic allows us to estimate the size and temperature profile of the quasar accretion disk.

#### 3.4.1 Chromatic microlensing

As mentioned in section 3.3, the flux variation in one or more images due to microlensing allow us to study the inner regions of a quasar. These variations allow us to estimate the accretion disk size ( $r_s$ ) and the temperature profile ( $p$ ) of the lensed quasar. To determine if chromatic microlensing exists, we analyze the magnitude difference (sec. 3.3) between two images in the continua and the core of the emission line as:

$$\Delta m = \Delta m^{cont} - \Delta m^{line} = (m_A - m_B)^{cont} - (m_A - m_B)^{line} \quad (3.7)$$

If the difference changes with wavelengths, then it is established that there is a chromatic microlensing effect. Extinction will be present if  $\Delta m^{line}$  is not constant and varies in wavelength (e.g. [Mediavilla et al. 2005](#)).

---

Once the chromatic microlensing is established, we follow [Mediavilla et al. 2011](#) assuming that the accretion disk is modeled as a Gaussian intensity profile:

$$I(R) \propto \exp(-R^2/2r_s^2), \quad (3.8)$$

where  $r_s$  is the size of the accretion disk which varies with wavelength ([Wambsganss & Paczynski 1991](#), [Mosquera et al. 2009](#), [Mediavilla et al. 2011](#)). According to the thin disk model  $r_s \propto \lambda^p$ , where  $p$  is the index related to the temperature profile of the disk ( $p=4/3$  according to the standard disk model, [Shakura & Sunyaev 1973](#)). It is also related to the *half-light radius* as  $R_{1/2} = 1.18r_s$  ([Mortonson et al. 2005](#)). The probability of reproducing the magnitude difference  $\Delta m$  for each wavelength, can be estimated by placing a random source on microlensing magnification maps ([Mediavilla et al. 2011](#)). These maps represent the magnification produced by the microlenses on the lens galaxy. The magnification patterns were usually created using the *Inverse Ray Shooting technique* (IRS, [Kayser et al. 1986](#), [Schneider & Weiss 1987](#), [Wambsganss et al. 1990](#)). In this method we try to simulate magnifications patterns of the source shooting regular lights rays from the lens plane towards the source plane (pixel by pixel). The lens and the source plane are divided in grids of pixel size. Each pixel in the source plane will have a magnification pattern proportional to the number of rays that hit it. This method demands a huge amount of time. An improvement was made by [Mediavilla et al. 2006](#) with the *Inverse Polygon Mapping algorithm* (IPM by [Mediavilla et al. 2011](#)), which consists on mapping square polygon (groups of pixels) on the image plane into the source plane. The magnification at each source pixel is computed by adding each portion of converted cell surface that overlays with that pixel ([Mediavilla et al. 2006](#)).

To construct the maps (see figure 3.2 as an example) we need the convergence and shear at each image ( $\kappa_A, \gamma_A, \kappa_B, \gamma_B$ ) and the mass fraction in randomly distributed compact objects ( $\alpha$ ). It is estimated that about 10% of the total matter of a galaxy is composed of compact objects in the halo of a galaxy ([Mediavilla et al. 2009](#), [Pooley et al. 2009](#), [Mosquera & Kochanek 2011](#)). The size of the microlens was considered with its Einstein radius, with  $1 M_\odot$ .

We convolve the magnification maps with Gaussians of different sizes ( $r_s(\lambda_i) = r_s(\lambda_i/\lambda_{ref})^p$ , with  $i = 1, 2, 3$ , evaluating in  $p$  and  $r_s$ ), that represents the disk structure over a grid. The



FIGURE 3.2: Microlensing magnification maps for component A of Q1355-2257 with a size of  $1000 \times 1000$  pix<sup>2</sup>. The  $\kappa$  and  $\gamma$  parameters for image A are 0.31 and 0.28 respectively (Sluse et al. 2012).

$\lambda_{ref}$  was considered 1026 Å (rest frame) to compare with other estimations (e.g., Jiménez-Vicente et al. 2014). The values of  $p$  go from 0.0 to 2.4 with steps of 0.15, and for  $\ln(r_s)$  (is a logarithmic grid) from 0.0 to 3.6 with steps of 0.15. Given  $p$  and  $\ln(r_s)$ , the likelihood of observing the three  $\Delta m$  due to the microlensing effect in the three wavelengths is:

$$P_l \left( \Delta m_k^{\text{obs}} \mid p_i, \ln(r_{sj}) \right) \propto \int \Delta m_1 \int \Delta m_2 \int \Delta m_3 N_{ij} e^{-\frac{1}{2}\chi^2}, \quad (3.9)$$

where  $\Delta m_1$ ,  $\Delta m_2$  and  $\Delta m_3$  are the magnitude difference obtained from the model given  $p$  and  $\ln(r_s)$ , and  $N_{i,j}$  is the number of trials. The chi-square ( $\chi^2$ ) measures the difference between the observed and expected set of variables, defined as:

$$\chi^2 = \sum_{k=1}^3 \frac{(\Delta m_k^{\text{obs}} - \Delta m_k^{\text{model}})^2}{\sigma_k^2}, \quad (3.10)$$

where  $\sigma_k^2$  are the uncertainties of the three  $\Delta m$  measured in the three wavelengths. Finally, a joint likelihood function is constructed by multiplying the individual likelihood functions:

$$P \left( \Delta m_{k,l}^{\text{obs}} \mid p_i, \ln(r_{sj}) \right) \propto \prod_{l=1}^m P_l \left( \Delta m_k^{\text{obs}} \mid p_i, \ln(r_{sj}) \right), \quad (3.11)$$

The parameter  $p$  and  $\ln(r_s)$  can be directly estimated in the joint likelihood function.

# Chapter 4

## Results

The results presented in section 4.1 are published in [Melo et al. 2021](#), while 4.2 and 4.3 are articles in preparation.

### 4.1 First black hole mass estimation for the quadruple lensed system WGD2038-4008

This system, also known as DES J2038-3008, is a quadruple lensed quasar (Figure 4.1) discovered in 2017 using a combination of Wide-field Infrared Survey Explorer (*WISE*, [Wright et al. 2010](#)) and *Gaia* ([Gaia Collaboration et al. 2016](#)) over the Dark Energy Survey (*DES*, [Dark Energy Survey Collaboration et al. 2016](#)) footprint. The source and deflector have redshifts of  $z_s = 0.777 \pm 0.001$  and  $z_l = 0.230 \pm 0.002$  respectively ([Agnello et al. 2018](#)). The deflector is a red galaxy with a compact bulge and a bright halo while the source has an extended quasar host galaxy ([Agnello et al. 2018](#)). It was observed using the Hubble Space Telescope (*HST*, see figure 4.1, right) and the images were used by [Shajib et al. 2019](#) to obtain a lens model using LENSTRONOMY ([Birrer & Amara 2018](#)). Spatially resolved narrow-line fluxes ([OIII] in [Nierenberg et al. 2020](#)) are also available. [Buckley-Geer et al. 2020](#) studied the lensing galaxy to measure its velocity dispersion and to identify the line-of-sight galaxies that need to be included in the lens model.

The reduction and extraction of spectra for images A and B and lens galaxy was made following the methodology explained in section 2.2.1. Unfortunately, the ADC<sup>1</sup> did not work

---

<sup>1</sup>Atmospheric dispersion corrector.

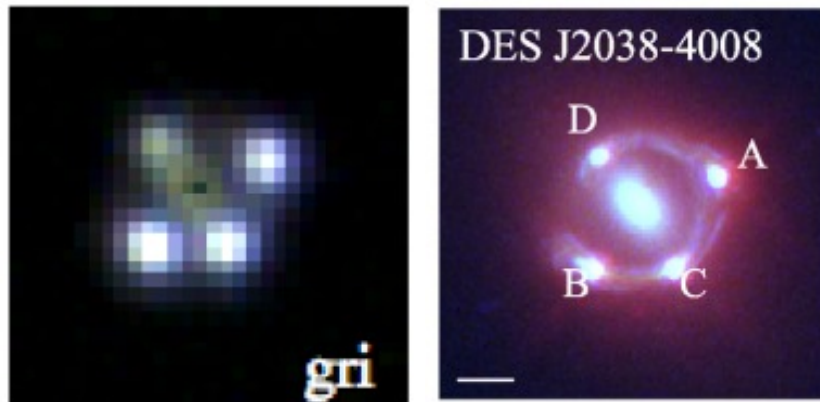


FIGURE 4.1: Two images of WGD2038-4008 using different telescopes. Left: DES image in filter gri from [Agnello et al. 2018](#). Right: Image obtained from [Shajib et al. 2019](#), which is a combination of three HST bands: F160W, F814W, and F475X.

during the night that OB 1 and 2 were taken, thus the UVB and VIS arm experienced flux loss (Appendix B), which explains the atypical profile of the AGN spectra (see [Vanden Berk et al. 2001](#) and [Glikman et al. 2006](#) for a composite quasar spectra). This flux loss will affect the luminosity measurement, specially in the UVB arm.

#### 4.1.1 Line profiles comparison

We identified the three most prominent emission lines of the lensed quasar WGD2038-4008 ( $\text{MgII}$ ,  $\text{H}\beta$ , and  $\text{H}\alpha$ ) with high S/N (see table 4.1). The spectra were demagnified using the parameters from the lens model of [Shajib et al. 2019](#) and the continuum was subtracted to compare the profiles of image A and B (Fig. 4.2). Interestingly, we find an enhancement of the right wing of  $\text{H}\alpha$  emission line of image B compared to image A (between  $\sim 6600$  and  $6700 \text{ \AA}$ ). This magnitude difference ( $\sim 0.28 \pm 0.03 \text{ mag}$  integrated in the region  $[6591.4:6686.5] \text{ \AA}$ ) could be explained assuming that microlensing is affecting the  $\text{H}\alpha$  broad emission line. This effect should also be seen in the  $\text{H}\beta$  profile as it arises from a region of similar size to  $\text{H}\alpha$ . However, we do not detect this effect, although this could be due to the low S/N of  $\text{H}\beta$  ( $S/N \lesssim 20$ ) compared to  $\text{H}\alpha$  ( $S/N \gtrsim 72$ ) and to the presence of absorption-like features. There is no sign of this effect in the  $\text{MgII}$  profile ( $S/N \lesssim 31$ ), which is reasonable because  $\text{MgII}$  emission is produced in a region farther away than the Balmer lines ([Goad et al. 2012](#)), and hence is less susceptible to microlensing effects.

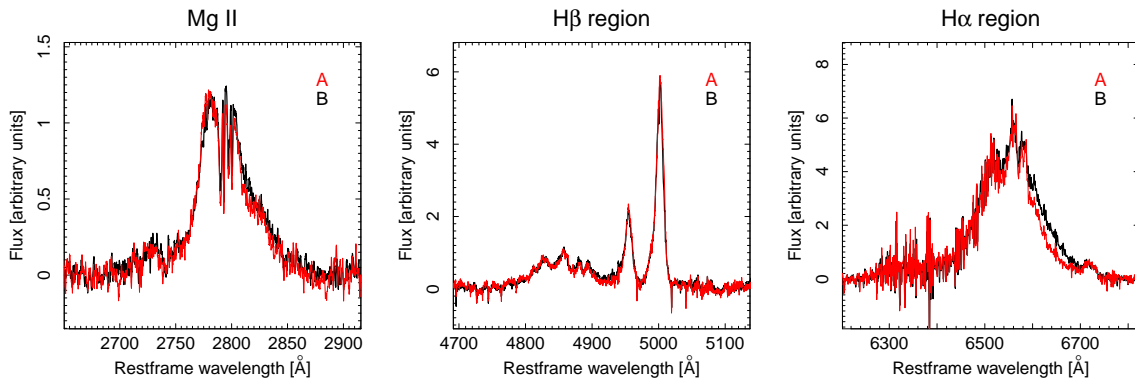


FIGURE 4.2: MgII, H $\beta$ , and H $\alpha$  emission line region. The images are demagnified using the magnification values from the lens model.

TABLE 4.1: FWHM, luminosities, and  $M_{BH}$ .

Image	Line	FWHM [km/s]	$\log_{10}(L_{ref})[L_{\odot}]^a$	$\log_{10}(M_{BH}) [M_{\odot}]$	$\log_{10}(r_s) [\text{cm}]^b$	S/N Line <sup>c</sup>	S/N Continuum
A	MgII	$3914.52 \pm 500.09$	$44.23 \pm 0.19$	$8.25 \pm 0.59$	$14.92 \pm 0.31$	30	5
	H $\beta$	$4689.32 \pm 42.96$	$44.29 \pm 0.17$	$8.27 \pm 0.24$	$15.26 \pm 0.79$	16	6
	H $\alpha$	$5595.68 \pm 125.92$	$44.36 \pm 0.23$	$8.57 \pm 0.22$	$15.63 \pm 0.83$	73	11
B	MgII	$4118.73 \pm 921.90$	$44.23 \pm 0.19$	$8.29 \pm 0.88$	$14.95 \pm 0.23$	35	6
	H $\beta$	$4817.63 \pm 48.15$	$44.21 \pm 0.16$	$8.24 \pm 0.21$	$15.23 \pm 0.85$	19	6
	H $\alpha$	$6150.98 \pm 133.39$	$44.29 \pm 0.23$	$8.61 \pm 0.27$	$15.66 \pm 0.74$	85	12

**Notes.** <sup>(a)</sup>  $L_{ref}$  = Luminosity ( $L_{3000}$ ,  $L_{5100}$ ,  $L_{5100}$ ) for MgII, H $\alpha$  and H $\beta$  respectively. The luminosity for H $\alpha$  and H $\beta$  is from the spectra and for MgII is obtained from the SED. <sup>(b)</sup>  $r_s$  is the accretion disk size obtained from equation 3.6 at the  $\lambda_{rest}$  of the emission line used for the  $M_{BH}$  measurement.

<sup>(c)</sup> This is the maximum S/N at the peak of the emission line.

### 4.1.2 Line width estimation

Multi-Gaussian fitting of images A and B are shown in Figure 4.3 following the procedure described in Section 3.2. The gray shaded regions represent the masked sections used during the fitting. Table 4.1 shows the FWHM estimated for each broad emission line in each quasar image. Even though the components of MgII have slightly different amplitudes, probably due to the absorptions that are contributing to the profile, the FWHM values are within the errors.

The FWHM of H $\beta$  is in good agreement in spite of the low S/N. In the case of H $\alpha$ , the estimated FWHM is different ( $>5\sigma$ ) and we discuss below how this might affect our  $M_{BH}$  estimations.

### 4.1.3 Microlensing analysis

To investigate whether microlensing is present in the continuum, we obtained the magnitude difference between the core of each emission line uncontaminated by the continuum,

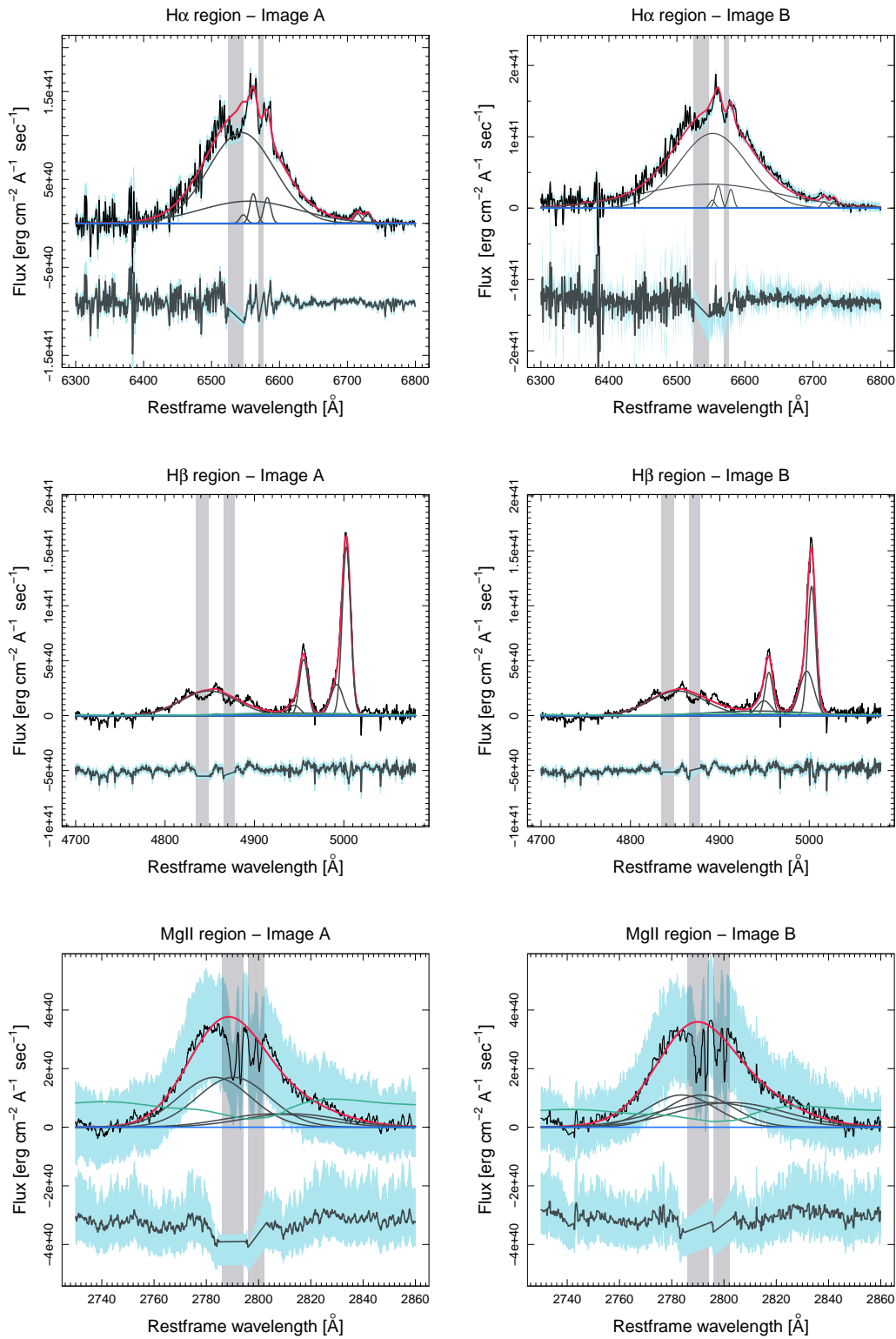


FIGURE 4.3: Gaussian fitting of H $\alpha$ , H $\beta$ , and MgII regions for images A (left) and B (right). The red line represents the best fit, the black lines represent the different components of each region (emission and absorption), the green line represents the Fe template, and the blue line is the continuum fit to the spectra. The 1 $\sigma$  error of the spectra along with the residuals and their respective errors are at the bottom of the images.

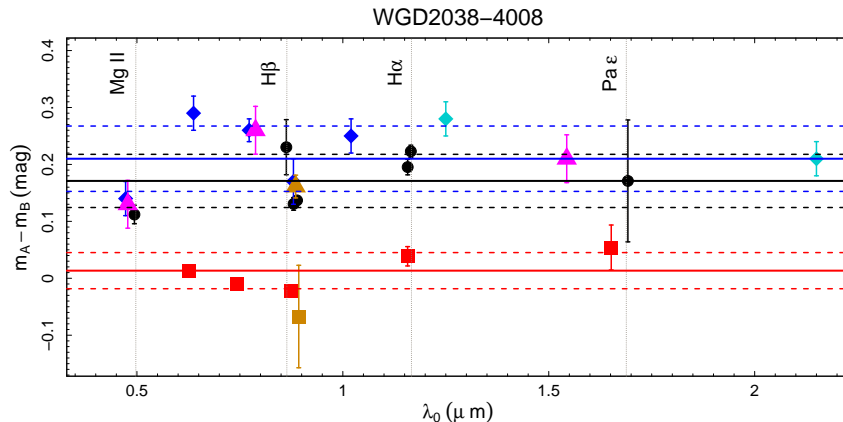


FIGURE 4.4: Magnitude difference  $m_A - m_B$  vs wavelength ( $\lambda_0$ ) between images A and B. The red squares show the integrated continuum and the black circles the emission line core without the continuum using X-shooter. Shown are the measurements obtained from the literature: HST [Shajib et al. 2019](#) (magenta triangles), VISTA [Lee 2019](#) (cyan diamonds), DES [Agnello et al. 2018](#) (blue diamonds) and HST F105W/G102 [Nierenberg et al. 2020](#) (orange square for continuum and orange triangle for a narrow emission line). The red line is the median of the continuum, the dotted red line the standard deviation, the black line the emission line core, and the blue line the literature.

$(m_A - m_B)^{\text{line}}$ , and the continuum under the emission line,  $(m_A - m_B)^{\text{cont}}$ , shown in Fig. 4.4. The  $H\alpha$  emission line region shows two values corresponding to two emission line peaks, avoiding the right wing (see Figure 4.2), integrated in the windows  $[6500.1:6526.0, 6547.7:6565.4]$  Å. The  $H\beta$  region shows three values corresponding to  $H\beta$  ( $[4820:4890]$  Å integration window) and the [OIII] doublet emission line cores ( $[4949.2:4960.0, 4996.4:5007.0]$  Å integration window). We included the MgII region integrated between  $[2774.6:2784.1]$  Å and Paschen  $\epsilon$   $[9512.0:9533.0]$  Å. Considering that the magnitude difference in the emission lines is approximately constant, we use the median and its standard error,  $(m_A - m_B)^{\text{line}} = 0.17 \pm 0.05$  mag, as our baseline of no-microlensing. As the values for the integrated continuum also yield a roughly constant value along the wavelength, we use the median to estimate  $(m_A - m_B)^{\text{cont}} = 0.01 \pm 0.03$  mag. We compare our result with spectroscopic data of the integrated flux obtained by [Nierenberg et al. 2020](#) (see Fig. 4.4)  $(m_A - m_B)_N^{\text{cont}} = -0.06 \pm 0.09$  and  $(m_A - m_B)_N^{\text{line}} = 0.16 \pm 0.02$  mag, which is in agreement with our magnitude difference for the continuum and emission line in the  $H\beta$  region, respectively. Published data from broadband photometry taken between 2016 and 2017 is also included in Fig. 4.4 ([Agnello et al. 2018](#), [Lee 2019](#), [Shajib et al. 2019](#)). We fit a median function to these values obtaining  $(m_A - m_B)^{\text{lit}} = 0.21 \pm 0.06$  mag. The values are in agreement with the core of our narrow emission lines.

Since the above-mentioned data are not time-delay corrected, the magnitude difference estimated from our spectra,  $\Delta m = (m_A - m_B)^{\text{cont}} - (m_A - m_B)^{\text{line}} = -0.16 \pm 0.06$  mag, could be due to intrinsic variability coupled with a time lag between the images. We use the [Yonehara et al. 2008](#) procedure to estimate this effect. We assume the structure function inferred from the imaging data of quasars ([Vanden Berk et al. 2004](#)), an absolute magnitude range for the source in I band,  $M_I = (-21, -30)$ , the predicted time delay for the quasar images  $\Delta t_{AB} = -6 \pm 1$  days ([Shajib et al. 2019](#)), and assume no lag between our observations as they were obtained with one day of difference. We obtained a magnitude difference induced by time delay coupled with intrinsic variability of 0.05 mag (0.03 mag) to 0.07 mag (0.04 mag) for a -21. mag (-30. mag) source in the F160W and F475W HST broadband filters, respectively. On the other hand, we also use light curves obtained by COSMOGRAIL (e.g., [Bonvin et al. 2017](#), [Courbin et al. 2011](#), [Eigenbrod et al. 2005](#)), which has a monitoring program to obtain time delay between multiple images of lensed quasars. WGD2038-4008 follow-up is carried out in MPIA 2.2m telescope (La Silla Observatory, Chile) with an average of one measurement per week (F. Courbin, private communication), although no time delay has been measured yet. We considered three dates that were seven days apart and within two weeks of our X-shooter observations, then shift the B data to correct by time delay, and estimate the average magnitude difference as  $(m_A - m_B)_{\text{corr}} \sim 0.16 \pm 0.03$  mag. This value is in good agreement with our estimation using the core of the emission lines. Therefore,  $\Delta m = -0.16 \pm 0.06$  mag seems to indicate the presence of a constant or long-lasting microlensing event not detected by the light curves ([Sluse & Tewes 2014](#)).

#### 4.1.4 Luminosity and $M_{\text{BH}}$ measurement

The monochromatic luminosity at  $L_{5100}$  was estimated using a single power-law function between two continuum windows on each side of the BELs. It agrees for  $H\alpha$  and  $H\beta$  of each image, within the errors, with an average value of  $\log_{10}(L_{5100}/L_{\odot}) = 44.29 \pm 0.03$ . Due to flux loss in UVB, we modeled a SED to estimate  $L_{3000}$  using the magnitudes and magnification of image A, obtaining  $\log_{10}(L_{3000}/L_{\odot}) = 44.23 \pm 0.19$ . The luminosities  $L_{3000}$  and  $L_{5100}$  agree within their errors, even though they were obtained with different methods. The  $M_{\text{BH}}$  was obtained following eq. 3.4 with an average value between images A and B of  $\log_{10}(M_{\text{BH}}/M_{\odot}) = 8.59 \pm 0.35$ ,  $8.25 \pm 0.32$ ,  $8.27 \pm 1.06$  for  $H\alpha$ ,  $H\beta$ , and  $\text{MgII}$ , respectively. The  $M_{\text{BH}}$  estimates obtained using the three different emission lines are consistent within  $2\sigma$ . We show the  $M_{\text{BH}}$  estimations along with those of the literature of lensed quasars in Figure 4.5. To

avoid the discrepancies associated with the different parameter values used by the authors, we combine their FWHM and monochromatic luminosity values using equation 3.4 to obtain  $M_{\text{BH}}$ . We converted from intrinsic to bolometric luminosity applying  $L_{\text{bol}} = A L_{\text{ref}}$ , where  $A = (3.81, 5.15, 9.6)$  for  $L_{\text{ref}} = (L_{1350}, L_{3000}, L_{5100})$  presented in [Sluse et al. 2012](#).

$M_{\text{BH}}$  estimates for 33 lensed quasars are also included in Fig. 4.5 (some of them have several values as they are obtained from different emission lines) as well as those of [Shen et al. 2019](#) for non-lensed quasars from SDSS reverberation mapping. The figure shows that our results for image A and B of WGD2038-4008 are in good agreement with those of the non-lensed quasars, situating our object in the low-luminosity range of the diagram.

The accretion disk size is estimated using equation 3.6 using the different  $M_{\text{BH}}$  estimates with the wavelength value at  $\text{H}\alpha$ ,  $\text{H}\beta$ , and  $\text{MgII}$ , and the measurements are shown in Table 4.1. The size of  $\text{MgII}$  is on average  $\log_{10}(r_s/\text{cm}) = 14.98 \pm 0.84$ ,  $\text{H}\beta$  is  $15.25 \pm 0.4$ , and  $\text{H}\alpha$   $15.67 \pm 0.74$ . Our estimates are in agreement within each other and with other systems accretion disk sizes ([Morgan et al. 2018](#)). We scaled our wavelength ( $\lambda$  in which the  $M_{\text{BH}}$  was measured) to  $2500 \text{ \AA}$ , assuming  $r_s \propto \lambda^{4/3}$  and obtained  $\log_{10}(r_s/\text{cm}) = 14.94 \pm 0.22$ ,  $15.25 \pm 0.82$  and  $15.65 \pm 0.79$  in  $\text{MgII}$ ,  $\text{H}\beta$ , and  $\text{H}\alpha$ , respectively. These values are consistent with the theoretical values estimated by [Morgan et al. 2018](#) at  $r_{2500}$ :  $15.41 \pm 0.15$  for  $\text{MgII}$ ,  $15.37 \pm 0.26$  for  $\text{H}\beta$ , and  $15.62 \pm 0.18$  for  $\text{H}\alpha$ .

#### 4.1.5 Conclusions

Here I summarize the results from my work. High S/N observations were obtained for the quadruple lensed system WGD2038-4008 using the X-shooter instrument at VLT. I used Gaussian fitting to obtain uncontaminated spectra for the A and B lensed quasar images and the lens galaxy. The most prominent emission lines were detected ( $\text{MgII}$ ,  $\text{H}\beta$ , and  $\text{H}\alpha$ ) as well as the absorption lines in the lensing galaxy. The velocity dispersion of the lensing galaxy spectra was confirmed, obtaining  $299 \pm 12 \text{ km/s}$ , in agreement with previously estimated values ( $2.96 \pm 19 \text{ km/s}$  [Buckley-Geer et al. 2020](#)).

The magnification factors were estimated from the lens parameters of [Shajib et al. 2019](#) ( $\mu_A = 2.27 \pm 0.21$  and  $\mu_B = 2.71 \pm 0.32$ ) and were used to demagnify the spectra. Comparing the continuum-subtracted emission lines, we find that there is an enhancement in the right wing of  $\text{H}\alpha$  of image B that could be due to microlensing. However, this effect is not seen in

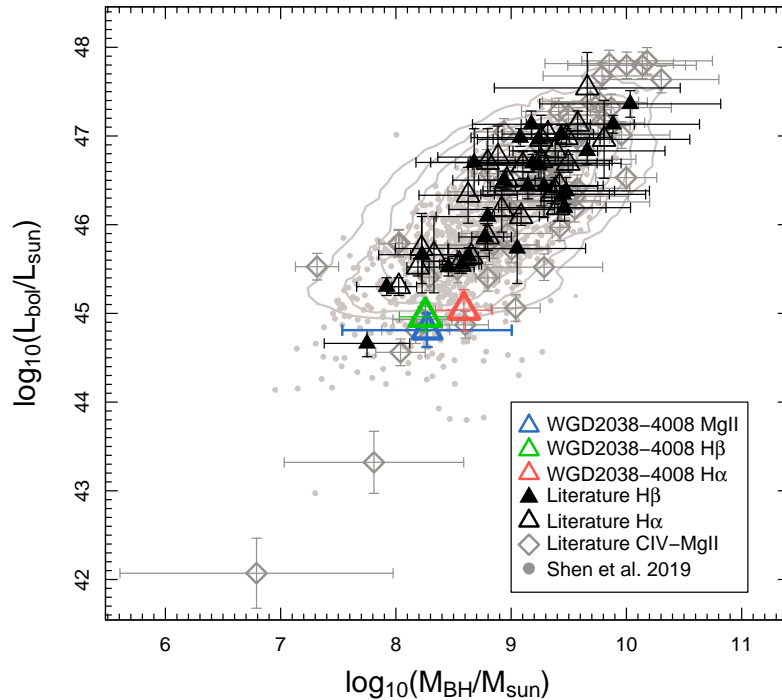


FIGURE 4.5:  $M_{BH}$  vs  $L_{bol}$  for quasars. The masses plotted are estimated from different emission lines and monochromatic luminosity found to date (Peng et al. 2006b, Assef et al. 2011, Sluse et al. 2012, Ding et al. 2017a). For lensed quasars, black open diamonds correspond to the  $M_{BH}$  derived from the MgII and CIV emission lines, black open triangle correspond to the  $H\alpha$  emission line, and black filled triangles to the  $H\beta$  emission line. For non-lensed quasars, Shen et al. 2019 data for  $M_{BH}$  from SDSS are represented by the gray dots and gray contours. The average  $M_{BH}$  mass estimation for WGD2038-4008 is represented as blue, red, and green triangles for MgII,  $H\beta$ , and  $H\alpha$  emission lines.

$H\beta$  (a region similar in size to  $H\alpha$ ) but this might be because of the low S/N and to the presence of absorption-like features. The MgII profile does not show any sign of microlensing, and it could be because it is produced in a region that is farther away. Magnification in the red wing of the  $H\alpha$  broad emission line has been detected in HE0435-1223 (Braibant et al. 2014) and QSO2237+0305 (Braibant et al. 2016). The main conclusion is that these line profile distortions can be explained by the differential magnification of a Keplerian disk model. As the continuum region is expected to be smaller than the BLR, the profile distortions are also accompanied by larger magnification of the continuum. However, in our case the magnification in the continuum is smaller than that in the  $H\alpha$  broad emission line. On the other hand, several papers describe an enhancement in the Fe  $K\alpha$  profile with higher magnification than the X-ray continuum in MG J0414+0534 (Chartas et al. 2002), QSO 2237+0305 (Dai et al. 2003), and H1413+117 (Chartas et al. 2004). This effect is attributed

to differential microlensing. [Popović et al. 2003](#), who use a standard accretion disk and caustic crossing to investigate the structure that could lead to such differences, conclude in [Popović et al. 2006](#) that different dimensions for the emitting region (e.g., an inner BEL annulus radius smaller than the continuum disk) and the segregation of emitters allow the reproduction of the Fe K $\alpha$  enhancement without an equivalent amplification of the continuum. Furthermore, [Abajas et al. 2007](#) demonstrated that this result could also be obtained in the case of a biconic model for the BEL. Thus, a similar effect might be used to explain our results, but a further analysis is needed to confirm this.

The FWHM was measured for the three emission lines and are in agreement for H $\beta$  and MgII for both images. Even though H $\alpha$  has a discrepancy in the right wing, we measured the FWHM for both of them (with a difference of  $> 5\sigma$ ).

The microlensing effect in the continuum was investigated obtaining the magnitude difference for the continuum ( $0.01 \pm 0.03$  mag) and the core of the emission lines ( $0.17 \pm 0.05$  mag). Our values are in agreement with spectroscopic data from [Nierenberg et al. 2020](#) and with photometric data corrected by time-delay. There seems to be a microlensing effect in the continuum of  $\Delta m = -0.16 \pm 0.06$  mag.

The monochromatic luminosity at 5100 Å was obtained for H $\alpha$  and H $\beta$  using a single power-law function to the region of interest. The luminosities for both images are in good agreement, with a mean of  $\log_{10}(L_{5100}/L_{\odot}) = 44.29 \pm 0.20$ . On the other hand,  $L_{3000}$  was estimated using SED and obtained  $\log_{10}(L_{3000}/L_{\odot}) = 44.23 \pm 0.19$ . Both luminosities are in agreement within the errors.

The  $M_{BH}$  was measured with the luminosity and the FWHM from the broad emission lines, obtaining a consistent mass for both images in the same BEL and a mean mass of  $\log_{10}(M_{BH}/M_{\odot}) = 8.37 \pm 0.40$  for this quadruple lensed quasar. When combined with the quasar's monochromatic luminosities, we find Eddington ratios similar to those measured in the literature for unlensed low-luminosity quasars. Finally, we obtained the accretion disk size from equation 3.6, obtaining an average size of  $\log_{10}(r_s/\text{cm}) = 15.28 \pm 0.63$ .

## 4.2 Black Hole masses using $H\alpha$ and $H\beta$ lines of gravitational lensing quasars

Reverberation mapping is often used to measure the  $M_{BH}$  in type 1 AGNs (Wandel et al., 1999, Kaspi et al., 2000, Peterson et al., 2004). Unfortunately, this method requires long-term monitoring, not practical for large samples (e.g. Peterson et al. 2004, Bentz et al. 2009, Barth et al. 2015, Grier et al. 2017, 2019, Du et al. 2016, Lira et al. 2018). In addition, the long-time variability in high redshift sources make the RM method unfeasible (e.g. Lira et al. 2018). Fortunately, the correlation relating the BLR size and the monochromatic luminosity at 5100 Å (Kaspi et al. 2000, 2005, Bentz et al. 2009, Park et al. 2012, Bentz et al. 2013) makes it possible to estimate the virial  $M_{BH}$  from the SE method using the  $H\beta$  width (e.g. Vestergaard 2004, Xiao et al. 2011, Shen & Liu 2012). For high redshift systems ( $z > 0.9$ ),  $H\beta$  is shifted into the NIR, making it difficult to observe from the ground for large samples due to the sky emission. Thus, the use of MgII and CIV emission lines to measure  $M_{BH}$  using the SE method was proposed by Vestergaard 2002 and McLure & Jarvis 2002. These lines allowed us to reach more high redshift systems in the optical range (e.g. McGill et al. 2008, Park et al. 2013, 2015, Coatman et al. 2017, Woo et al. 2018), but they present several drawbacks: UV lines lack of local calibrations, MgII have a small dependence on the Eddington ratio of the AGN and CIV may be affected by winds (see section 1.3). And hence, the Balmer lines are the more reliable virial mass estimators. The  $H\alpha$  emission line provides a good substitution in the absence of  $H\beta$  due to the fact that its width is well correlated with the width of  $H\beta$  (Greene & Ho 2005, Netzer & Trakhtenbrot 2007, Xiao et al. 2011).

Many studies have estimated  $M_{BH}$  using the SE method for large samples of quasars (e.g. McLure & Jarvis 2002, McLure & Dunlop 2004, Vestergaard & Peterson 2006a, Shen 2013, Peterson 2014, Mejía-Restrepo et al. 2016, Shen et al. 2019), and over the last decade, samples of lensed quasars have also been used. Peng et al. 2006b were the first to estimate the  $M_{BH}$  of 31 gravitationally lensed AGNs of redshift  $0.6 < z < 4.1$ . They applied the virial technique using the CIV (22 systems), MgII (19 systems) and  $H\beta$  (2 systems) emission line widths with the continuum luminosities  $\lambda L_{\lambda}$ : 1300, 3000 and 5100 Å, respectively. Seven of the systems have two estimations obtained from two different emission lines. The FWHM was calculated using the emission lines from existing published spectra (Peng et al. 2006a). The AGN continuum luminosity comes from first separating the AGN from the host galaxy (using observed HST images as part of the CASTLES program), and then fit the broadband

HST photometry with a power-law to estimate the continuum luminosity entering the virial relation (see Peng et al. 2006b for details). For seven of the lensed quasars, the  $M_{BH}$  was obtained from both the MgII and CIV emission lines, and Peng et al. 2006b concluded that they are in consistent with other studies using non-lensed AGNs.

The estimation for lensed AGNs was followed by Greene et al. 2010, Assef et al. 2011 and Sluse et al. 2012. Greene et al. 2010 used data from the near-infrared spectroscopy from the Triplespec at Apache Point Observatory (Wilson et al. 2004) and obtained the  $M_{BH}$  for 16 systems using the Balmer lines. Their goal was to remove the systematic bias made by Peng et al. 2006b in the  $M_{BH}$  using CIV emission line, by calculating the mass using the Balmer lines. For the luminosity, they fitted a power-law continuum, Fe II emission, and Balmer continuum simultaneously, using emission-line-free windows. The emission lines were fitted with multi-component Gaussians (narrow and broad). Even though the masses presented by Greene et al. 2010 are more robust because they used spectra with higher S/N than Peng et al. 2006b, they conclude that there is no evidence for a systematic bias between the lines used by Peng et al. and the Balmer lines, despite the large scatter.

Continuing with the work made by Greene et al. 2010, Assef et al. 2011 searched for possible biases between  $M_{BH}$  estimates based on the  $H\alpha$ ,  $H\beta$  and CIV broad emission lines. Assef et al. believed that the sample from Greene et al. 2010 did not cover a large range in  $M_{BH}$  to conclude if there was a mass-dependence slope to the relation between the masses and that Peng et al. 2006b sample lacked access to original spectra for several targets. They selected 12 lensed quasar ( $1.3 < z < 3.6$ ) from the CASTLES survey with high quality spectra of CIV and published NIR spectra of the Balmer lines. Three objects were added from the sample presented by Greene et al. 2010 (SDSS1138+0314, HS0810+2554 and SBS0909+532). The FWHM was estimated using broad and narrow Gaussian components and the continuum luminosity at 5100 Å was estimated using the AGN SED template of Assef et al. (2010). They conclude that the  $M_{BH}$  estimated from CIV using the line dispersion ( $\sigma_l$ ) shows a systematic offset with respect to the  $M_{BH}$  using the FWHM. Then, Assef et al. 2011 compared the  $M_{BH}$  estimated using CIV and the Balmer lines and found no significant offset. For the first time, microlensing was mentioned (but not analyzed) in the CIV emission line.

Sluse et al. 2012 searched for microlensing in the continuum and broad emission lines for 17 lensed quasars. In addition,  $M_{BH}$  was estimated using CIV (5 systems), MgII (12 systems) and  $H\beta$  emission lines (2 systems), where two objects have estimations from two different

---

emission lines and four of these systems are published values from Peng et al. 2006b and Assef et al. 2011. The luminosity at 3000 Å and FWHM derived for MgII was made fitting two Gaussians to the emission line on top of a pseudo-continuum component. From the  $M_{BH}$ , Sluse et al. 2012 estimated that 85% of the sources showed microlensing in the continuum, but the luminosity is corrected from the macro-magnification associated to lensing.

To date, no new large samples of lensed quasars have been used to measure the black hole mass with the SE method. In general, recent publications refer to the  $M_{BH}$  mentioned above (e.g. Ding et al. 2017b, Guerras et al. 2020, Ding et al. 2021, Hutsemékers & Sluse 2021). Considering those systems in the CASTLES survey, only 11 out of 100 lensed quasars have  $M_{BH}$  measured using H $\alpha$  and/or H $\beta$  lines. We want to increase the sample both in number of systems and luminosity range to compare our measurements with those already in the literature for lensed and non-lensed quasars.

In this thesis, I present 14 spectroscopic observations taken in 2012 for 11 lensed quasars. The whole sample consists of six doubles and five quadruple lensed quasars (Figure 4.6) that have source redshifts between  $1.52 \leq z_s \leq 2.55$ . Two have no  $M_{BH}$  measurements and two have previous estimates using H $\alpha$  (HE1104-1805 and SDSS1138+0314), while nine systems have estimates using CIV and/or MgII broad emission lines.

HE0047-1756, HE0435-1223 and SDSS0924+0219 were observed with the Large Binocular Telescope using LUCIFER instrument, and the remaining objects were observed with MMIRS instrument mounted in the *Magellan* Clay telescope, Chile.

#### 4.2.1 $M_{BH}$ measurement

After de-magnifying the spectra and converting from flux to luminosity (sec. 2.2.3), the FWHM and monochromatic luminosity at 5100 Å was measured. The FWHM of H $\alpha$  and H $\beta$  emission lines were modelled using the Gaussian fitting of broad and narrow emission lines described in Section 3.2.1 (Figure 4.7). The gray shaded regions represent the masked regions due to poor telluric correction. The luminosity at 5100 Å was obtained following Assef et al. 2010 method, i.e. creating SEDs for the brightest image (image A) using the fluxes from CASTLES. SEDs were preferred to measure the luminosity instead of using the spectra because of the low S/N ( $3 < S/N < 18$ , see table 2.5). The  $M_{BH}$  was finally obtained following equation 3.4 (table 4.2).

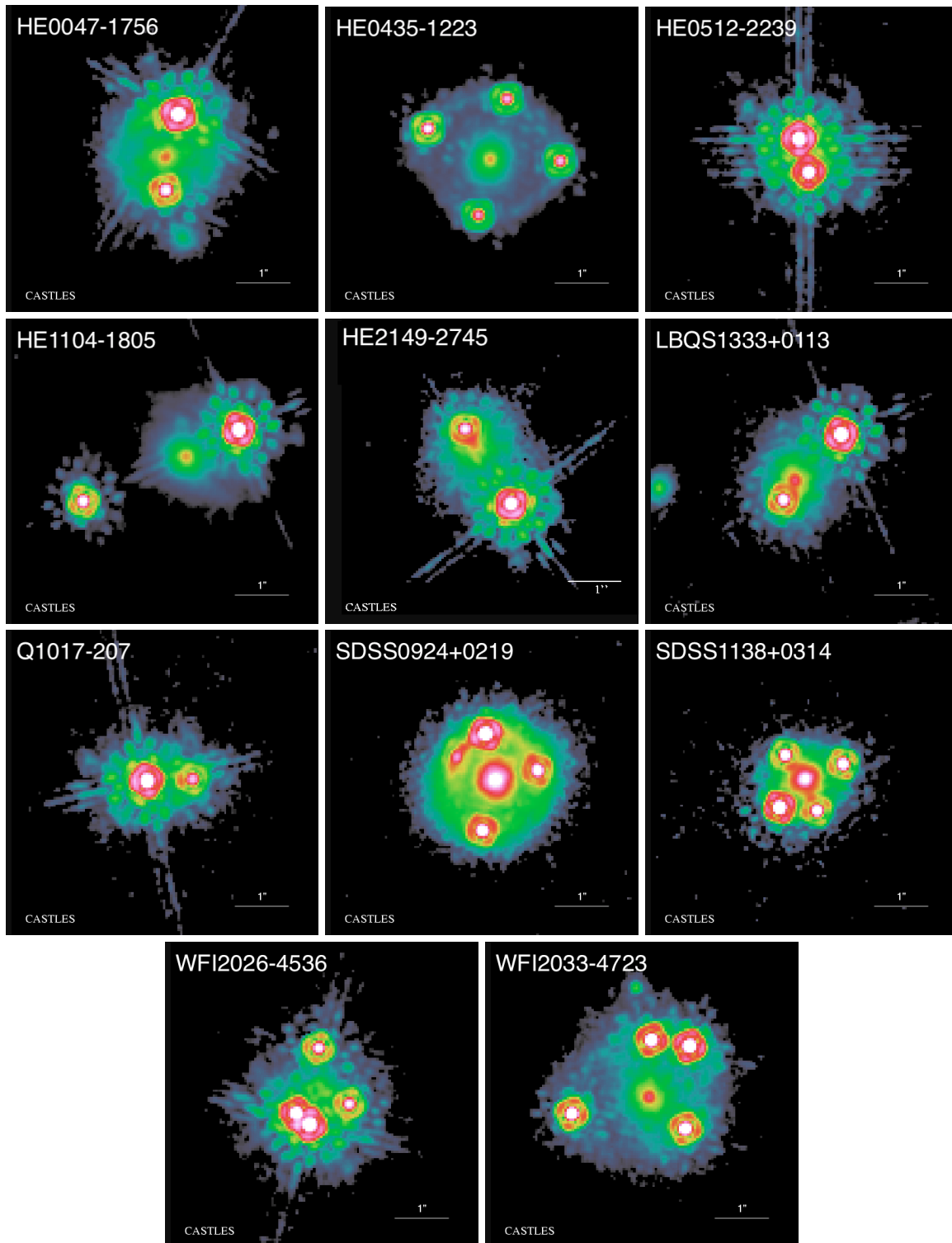


FIGURE 4.6: HST images in filter F160W for the 11 lensed quasars. The images are obtained from CASTLES webpage in filter F160W.

Figure 4.8 shows the new  $M_{BH}$  measurements obtained with MMIRS and LUCIFER (including WGD2038-4007 results from section 4.1). Compared to the previous figure of sec. 4.1, two systems from the literature were excluded: MG 2016+112 because it is a type II AGN (no

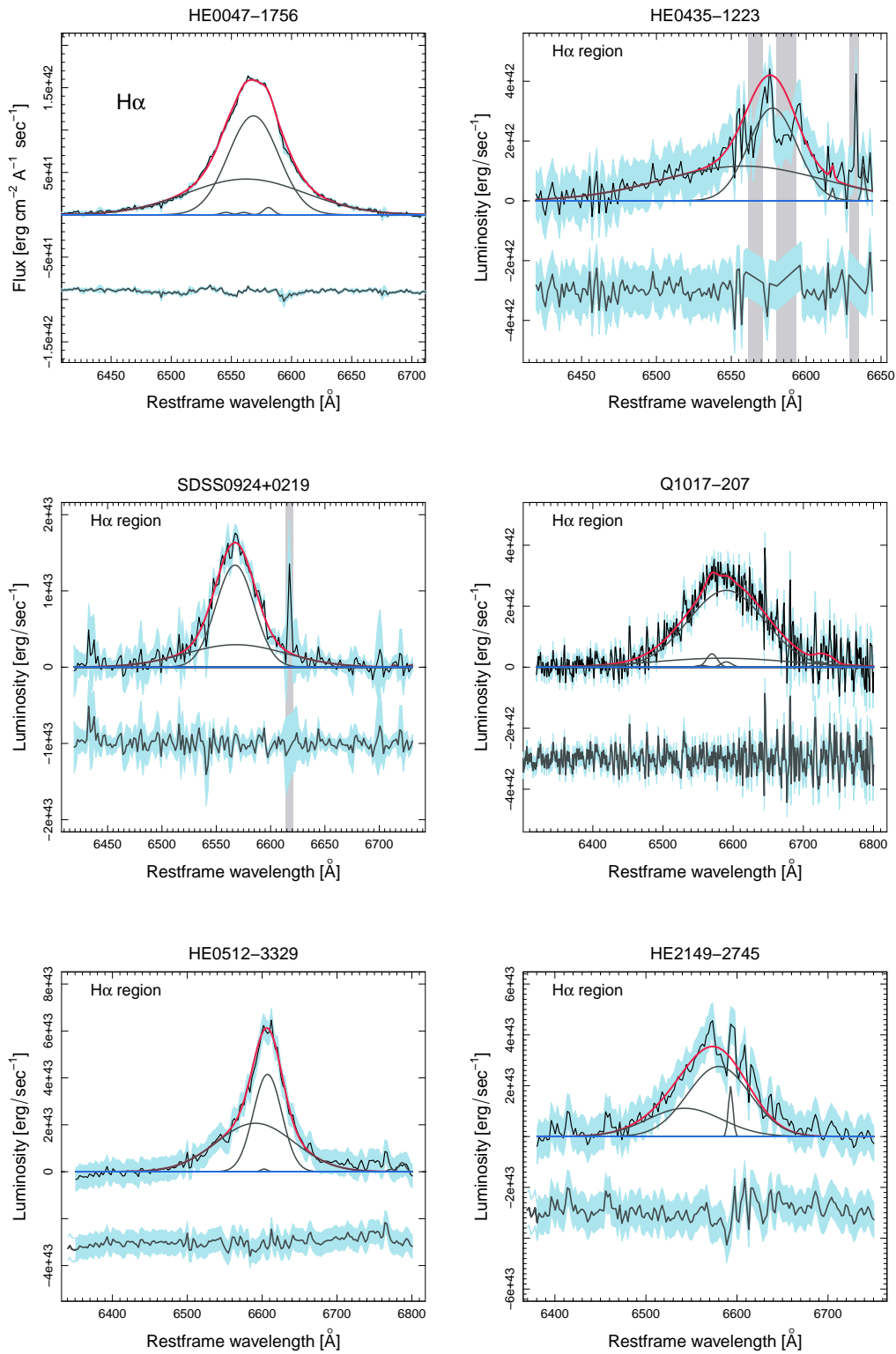


FIGURE 4.7: Gaussian fitting of H $\alpha$  and H $\beta$  emission lines for the lensed quasars. The red line represents the best fit, the black lines represent the different components of each region, the green line represents the Fe template, and the blue line is the continuum fit to the spectra. The 1 $\sigma$  error of the spectra along with the residuals and their respective errors are at the bottom of the plots.

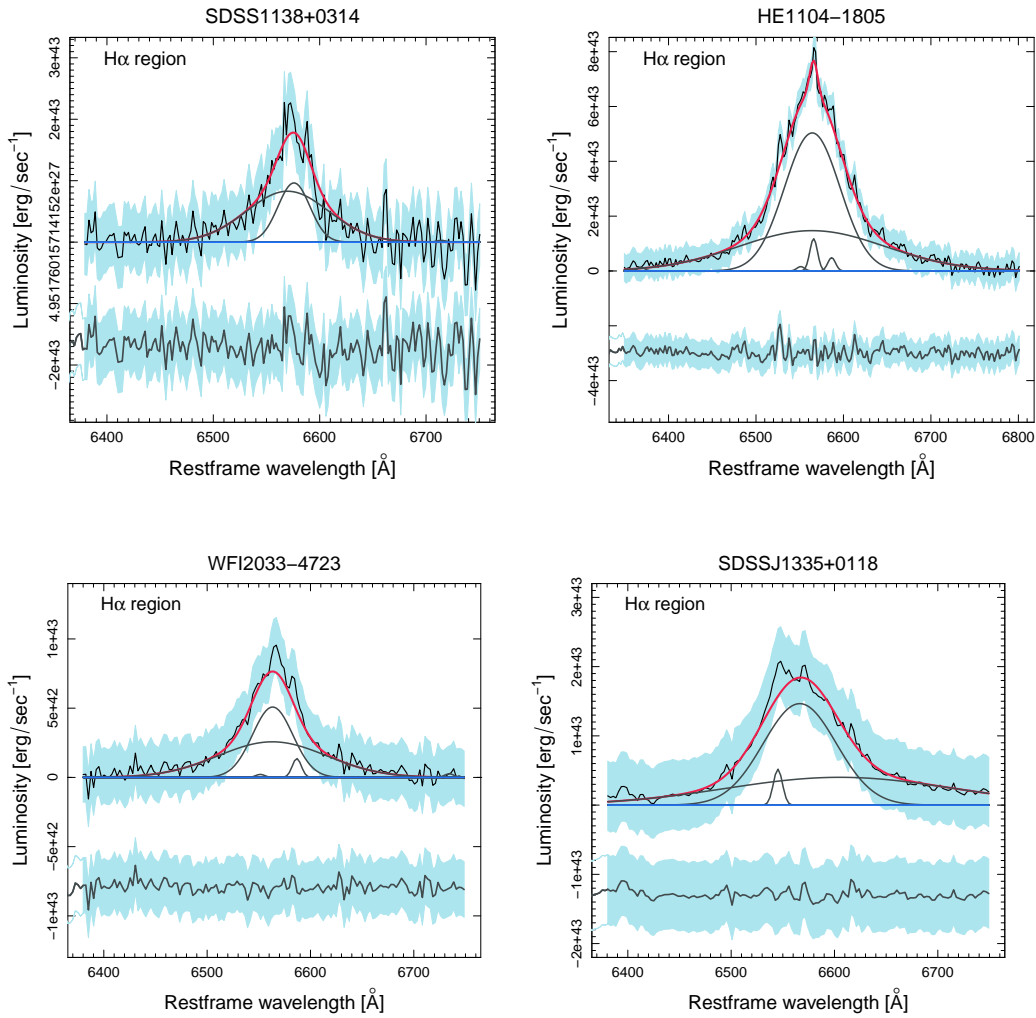


FIGURE 4.7: Gaussian fitting of  $H\alpha$  and  $H\beta$  regions for the lensed quasars. The red line represents the best fit, the black lines represent the different components of each region, the green line represents the Fe template, and the blue line is the continuum fit to the spectra. The  $1\sigma$  error of the spectra along with the residuals and their respective errors are at the bottom of the plots. (cont.)

broad lines: [Koopmans et al. 2002](#), [Ding et al. 2017b](#)) and B2045+265 due to the incorrect redshift identification of the AGN by [Fassnacht et al. 1999](#) ([Ding et al. 2017b](#)). The  $M_{BH}$  using  $H\alpha$ ,  $H\beta$ ,  $MgII$  and  $CIV$  of 33 lensed quasars from the literature of lensed quasars are included in the figure (measurements from [Peng et al. 2006b](#), [Greene et al. 2010](#), [Assef et al. 2011](#) and [Sluse et al. 2012](#)). The recently new  $M_{BH}$  estimation for WGD2038-4008 ([Melo et al. 2021](#)) is also included along with measurements of non-lensed quasars from the SDSS ([Shen et al. 2019](#)). To avoid discrepancies due to the different parameter values used by the authors ( $K$  and  $\alpha$  in equation 3.4), we used their FWHM and luminosity to calculate the  $M_{BH}$ . We converted the intrinsic luminosity to bolometric using  $L_{bol} = A \times L_{ref}$ , where  $A = (3.81, 5.15, 9.6)$  for  $L_{ref} = (L_{1350}, L_{3000}, L_{5100})$  from [Sluse et al. 2012](#). Notice that this

TABLE 4.2: H $\alpha$  and H $\beta$  BH mass estimates of lensed quasars.

Object	$z_{source}$	Line	$\log_{10}(L_{ref})[L_{\odot}]$	FWHM [km/s]	$\log_{10}(M_{BH})[M_{\odot}]$
HE0047-1756	1.67	H $\alpha$	$44.83 \pm 0.25$	$2678 \pm 37$	$8.24 \pm 0.12$
HE0047-1756	1.67	H $\beta$	$44.83 \pm 0.25$	$5455.73 \pm 540$	$8.75 \pm 0.80$
HE0435-1223	1.69	H $\alpha$	$44.91 \pm 1.04$	$2143.27 \pm 315.93$	$8.09 \pm 0.60$
HE0512-3329	1.57	H $\alpha$	$45.62 \pm 0.63$	$2629.03 \pm 10.97$	$8.73 \pm 0.67$
SDSS0924+0219	1.52	H $\alpha$	$44.01 \pm 1.03$	$2127.71 \pm 161.63$	$7.51 \pm 0.13$
SDSS0924+0219	1.52	H $\beta$	$44.01 \pm 1.03$	$4081.17 \pm 356.09$	$7.96 \pm 0.55$
Q1017-207	2.55	H $\alpha$	$45.66 \pm 1.01$	$6176.82 \pm 925.95$	$9.50 \pm 1.23$
HE1104-1805	2.32	H $\alpha$	$46.05 \pm 0.7$	$3972.43 \pm 226.61$	$9.37 \pm 1.06$
SDSS1138+0314	2.43	H $\alpha$	$45.03 \pm 0.42$	$2330.41 \pm 38.29$	$8.24 \pm 0.16$
SDSSJ1335+0118	1.57	H $\alpha$	$45.06 \pm 0.82$	$4437.89 \pm 141.09$	$8.82 \pm 0.58$
WFI2026-4536	2.23	H $\alpha$	$45.13 \pm 1.07$	$2344.28 \pm 15.99$	$8.21 \pm 0.58$
WFI2033-4723	1.66	H $\alpha$	$46.01 \pm 1.02$	$2684.07 \pm 255.25$	$9.00 \pm 1.17$
HE2149-2745	2.03	H $\alpha$	$46.83 \pm 0.8$	$4205.82 \pm 272.56$	$9.93 \pm 1.58$

is the first  $M_{BH}$  estimation for the systems HE0512-3329 ( $\log_{10}(M_{BH}/M_{\odot}) = 8.73 \pm 0.67$ ) and WFI2026-4536 ( $\log_{10}(M_{BH}/M_{\odot}) = 8.21 \pm 0.58$ ).

## 4.2.2 Discussion

Until this moment, there are 11 lens systems from the CASTLES database with black hole masses estimated using H $\alpha$  and H $\beta$  broad emission lines. In this work, we are expanding the sample by adding 11 systems (11 using H $\alpha$  and two with H $\beta$  BEL), increasing the number of estimated  $M_{BH}$  from Balmer lines by 50%. Our sample covers a range of luminosities similar to that presented by the non-lensed AGNs ( $\sim 10^{45} - 10^{48}$ , see fig. 4.8). Our results are in agreement with those obtained for the other systems, and shows less dispersion than the  $M_{BH}$  values using MgII and CIV. In addition to WGD2038-4008, there is another low luminosity  $M_{BH}$  value (SDSS0924+0219). This system has  $M_{BH}$  estimation but with MgII emission line (Peng et al. 2006b, Sluse et al. 2012), which are in agreement with their errors. HE2149-2745 present the highest  $M_{BH}$  of the lensed quasars with  $\log_{10}(M_{BH}/M_{\odot}) = 9.93 \pm 1.58$  using the H $\alpha$  emission line and SDSS0924+0219 the lowest ( $\log_{10}(M_{BH}/M_{\odot}) = 7.51 \pm 0.13$ ). For the first time, we estimated the  $M_{BH}$  for two of the systems: HE0047-1756 and SDSS0924+0219. The H $\beta$  measurements are in agreement within the errors with the  $M_{BH}$  of H $\alpha$  for both objects.

Comparing our results with previous samples given  $M_{BH}$  estimations, there are differences that need to be noticed. The magnification factor in which the monochromatic luminosity is demagnified is not reported by Peng et al. 2006b and Greene et al. 2010, there is also no

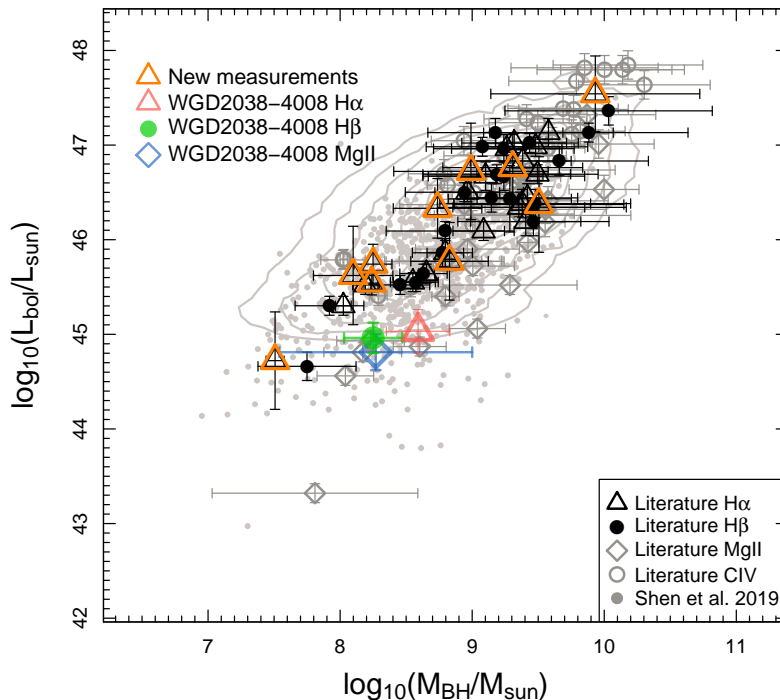


FIGURE 4.8: Mass-luminosity relation for AGNs. The masses are estimated from different emission lines and the monochromatic luminosity found to date for lensed quasars (Peng et al. 2006b, Greene et al. 2010, Assef et al. 2011, Sluse et al. 2012) is compared to those obtained for non-lensed quasar from Shen et al. 2019. For lensed quasars, gray open diamonds correspond to the  $M_{BH}$  derived from the MgII, gray circles from CIV emission lines, black open triangles correspond to the H $\alpha$  emission line, and black filled circles to the H $\beta$  emission line. For non-lensed quasars, Shen et al. 2019 data for  $M_{BH}$  from SDSS are represented by the gray dots and gray contours. The orange open triangles are our new  $M_{BH}$  estimation of lensed AGNs. We red open triangle, blue open diamond and green circle are the WGD2038-4008 values from Melo et al. 2021

mention to whether the spectra was deblended or not. The S/N is not mentioned either, and Peng et al. 2006b do not correct for the Fe II contribution in MgII and H $\beta$ . Even though we can compare our  $M_{BH}$  with the results obtained by Assef et al. 2010 using the Balmer lines, their CIV  $M_{BH}$  might be unreliable due to several reasons (section 1.3). For instance, the CIV line with is weakly correlated with the width of H $\beta$  and H $\alpha$  and exhibit a large scatter in many AGN sample (e.g. Baskin & Laor 2005, Shen et al. 2008, Fine et al. 2010, Trakhtenbrot & Netzer 2012, Mejía-Restrepo et al. 2018), CIV profile shows large blueshifts (Shang et al. 2007, Richards et al. 2011) and the core of CIV does not reverberate in response to continuum variations (Denney 2012). The Balmer lines continues to be the most reliable  $M_{BH}$  estimation.

In general, our estimations have larger uncertainties compared to [Assef et al. 2011](#), which is expected due to the low S/N of LUCIFER and MMIRS spectra. [Assef et al. 2011](#) measured the mass using the Balmer lines for SDSS1138+0314 ( $\log_{10}(M_{\text{BH}}/M_{\odot}) = 8.22 \pm 0.22$  and  $8.5 \pm 0.23$  for H $\alpha$  and H $\beta$  respectively) and HE1104-1805 ( $\log_{10}(M_{\text{BH}}/M_{\odot}) = 9.05 \pm 0.23$  and  $8.77 \pm 0.3$  for H $\alpha$  and H $\beta$  respectively). Their values are in agreement with ours for SDSS1138+0314 using the H $\alpha$  emission line, and for HE1104-1805 they are consistent, but our measurements have large uncertainties. The reason is the low S/N we have in our spectra (S/N  $\sim 11$ ) compared to [Assef et al.](#)'s (S/N  $\sim 221$ ), which result in a bigger FWHM error, and hence  $M_{\text{BH}}$  errors.

We need to consider multiple factors that could contribute to the uncertainties in the  $M_{\text{BH}}$  (in addition to the S/N). For instance, the BEL could be distorted by microlensing (e.g. [Richards et al. 2004b](#), [Guerras et al. 2013](#), [Braibant et al. 2016](#), [Fian et al. 2021](#)), affecting the FWHM value. In a few cases (see table 2.5) we were unable to deconvolve the two images, thus the  $M_{\text{BH}}$  estimation corresponds to the combination of the FWHM of both images. Nevertheless, even if we have a FWHM difference between the images of  $> 5$  sigma, the impact in the  $M_{\text{BH}}$  is negligible compared with other sources of errors (see [Melo et al. 2021](#)). The uncertainties in the monochromatic luminosity could be produced by several factors: the systematic error of the instrument, magnification of the image given by the lens model, flux calibration, intrinsic variability and microlensing in the continuum.

### 4.2.3 Conclusion

Black hole masses were estimated for 11 lensed quasars using H $\alpha$  and/or H $\beta$  emission lines (increase by a 50%). For the first time the  $M_{\text{BH}}$  was measured for HE0512-3329 and WFI2026-4536. Even though some systems have  $M_{\text{BH}}$  estimated using MgII and/or CIV broad emission lines, they show more dispersion in the  $M_{\text{BH}} - L_{\text{bol}}$  plot. Our data covers a range of luminosities comparable to non-lensed AGNs ( $\sim 10^{45} - 10^{48}$ ) consistent with the  $M_{\text{BH}}-L$  relation obtained from non-lensed AGNs. We compare our sample to other  $M_{\text{BH}}$  estimates from other lines, and we conclude that the Balmer lines are more reliable. We increase the sample of lensed quasars that have  $M_{\text{BH}}$  using the Balmer emission lines from 11 to 24 new sources.

We are still working on the analysis of the results to be sent for publication soon.

### 4.3 Black hole mass estimation using different emission lines for three double lensed quasars

The study of the broad emission lines in type I AGNs is crucial due to its proximity they have to the black hole. The geometry and kinematics of the BLR have been deeply investigated through reverberation mapping (RM), which measures the lag between the variation in the luminosity of the central continuum source and the response of the BLR (Blandford & McKee 1982, Peterson 1993). The RM studies were able to constrain the physical scales of three components of the AGN (Fausnaugh et al. 2017): the accretion disk is about a few light days from the SMBH (e.g. Sergeev et al. 2005), the BLR size will depend on the AGN luminosity, ranging from light days upto light years (Wandel et al. 1999, Kaspi et al. 2000, 2005, Guerras et al. 2013), and the obscuring torus extends beyond the BLR for several light months or years (Oknyanskij & Horne 2001, Suganuma et al. 2006). Furthermore, it seems that the accretion disk is larger than predicted by the standard model (Shakura & Sunyaev 1973) due to the observed continuum lags throughout the disk (e.g. Edelson et al. 2015, McHardy et al. 2016). This was also supported by microlensing analyses of lensed quasars (e.g. Morgan et al. 2010, Blackburne et al. 2011, Mosquera et al. 2013).

Even though RM has been successful in measuring the  $M_{BH}$ , it also has its limitations. The higher the luminosity of an AGN, the longer the time delay scale, and quasars will have lower variability amplitudes (MacLeod et al. 2010). This means that RM studies are limited to nearby, lower luminosity AGNs. The calibration for the estimation of the  $M_{BH}$  was improved with the discovery of the strong correlation between the size of the BLR and the continuum luminosity ( $R_{BLR} - L$  relation, Kaspi et al. 2000, Bentz et al. 2013), allowing us to measure the  $M_{BH}$  from single epoch spectra (SE method, Vestergaard 2004). However, this calibrations were made for the  $H\alpha$  and  $H\beta$  emission lines in the optical range. These lines are shifted into the NIR for high redshift quasars, and the easiest lines to measure  $M_{BH}$  in the optical are MgII and CIV (Vestergaard 2002). Even though these lines allow us to reach high redshift quasars, they have limitations without direct calibrations and might not be reliable (e.g., the width of CIV could be affected by wind flows: Mejía-Restrepo et al. 2018, and MgII could have a small dependence on the Eddington ratio of the AGN: Marziani et al.). The  $M_{BH}$  for lensed quasars has been calculated using the SE method for the CIV, MgII and the Balmer lines (Peng et al. 2006b, Greene et al. 2010, Assef et al. 2011, Sluse et al.

---

2012, Melo et al. 2021). Although it was an improvement for higher redshifts, a disadvantage is that they could suffer from microlensing effect.

In this work I will present the  $M_{BH}$  estimation for three double lensed quasars observed with the X-shooter instrument: LBQS1333+0113 (also named SDSSJ1335+0118), Q1355-2257 and QJ0158-4325. The three systems were chosen from the CASTLES database and their redshifts ( $1.5 < r_s < 2.7$ ) allows to observe the four most prominent emission lines. LBQS1333+0113 and Q1355-2257 have previous  $M_{BH}$  using MgII emission line. In addition, microlensing has been reported in Q0158-4325 (Chartas et al. 2017), Q1355-2257 (Sluse et al. 2012, Rojas et al. 2020) and LBQS1333+0113 (Sluse et al. 2012) and the three shows chromatic microlensing. Thus, the size of the accretion disk will be calculated and compared using two methods:  $M_{BH}$  and chromatic microlensing analysis.

The systems were observed between August of 2019 and April of 2021 (ESO proposal ID 103.B – 0566(A); PI: A. Melo) using the X-shooter instrument at VLT, Paranal, Chile. The reduction was made using ESO pipeline `EsoReflex` along with Principal Component Analysis for the sky emission subtraction (see section 2.2.1). The extraction of each component was made using only two Gaussian functions because the emission from the lens galaxy is negligible. The details for the reduction and extraction of each component can be seen in section 2.2.1. The 1D spectra for image A and B of each system are shown in appendix B.

In the next subsections I will present the analysis and results for each system individually and then compare the  $M_{BH}$  and the accretion disk size estimation obtained from two approaches: using the  $M_{BH}$  measurements and the chromatic microlensing effect

### 4.3.1 Data and line profiles

#### 4.3.1.1 LBQS1333+0113

This double system (Figure 4.9), also known as SDSSJ1335+0118, was discovered by Oguri et al. 2004. They presented imaging data from the Subaru Prime Focus Camera (Miyazaki et al. 2002) on the Subaru 8.2-m telescope of the National Astronomical Observatory of Japan and with the Near InfraRed Camera (NIRC, Matthews & Soifer 1994), including spectroscopic follow-up observations from ESO Multi-Mode Instrument (EMMI) on the ESO New Technology Telescope (NTT, D’Odorico 1990), confirming a double gravitational lens at

---

$z_s = 1.57$  with a separation of  $1.56''$ . The lens galaxy has a redshift of  $z_l = 0.44$  (Eigenbrod et al., 2006).

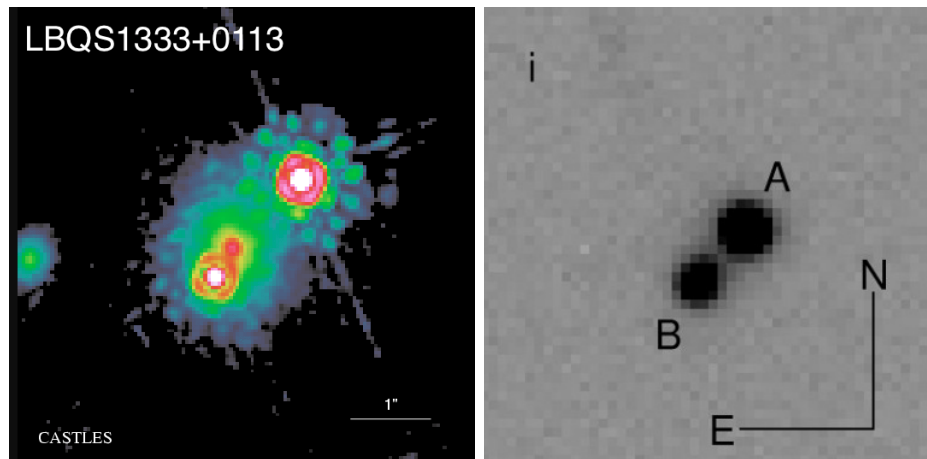


FIGURE 4.9: Images of the system LBQS1333+0113. Left: HST images in filter F160W obtained from CASTLES. Right: Original Subaru Suprime-Cam image in the  $i$ -band from Oguri et al. 2004 taken in 2003.

Even though this system was discovered almost two decades ago, it has not been further investigated using  $H\alpha$  and  $H\beta$  emission lines. Sluse et al. 2012 and Peng et al. 2006b obtained the  $M_{\text{BH}}$  using MgII emission line. The macro-magnification parameters of the lensed galaxy were obtained from a lens model made by Sluse et al. 2012 (table 3.1). Time delay between the images has been obtained with a lens model by Paraficz et al. 2009 (26.2 days) and Sluse et al. 2012 (49 days). Microlensing analysis was done by Sluse et al. 2012, confirming microlensing in MgII and CIII] broad lines, which also showed a blueshift ( $\sim 1000 \text{ km s}^{-1}$ ) in CIII]. They suggest that microlensing in both lines have two velocity components in the BLR, one that has a narrow component centered at  $v \sim 1500 \text{ km s}^{-1}$  and another that give rise to the broad symmetric profile.

In general, the X-shooter spectra of this system (appendix B) shows prominent absorption lines, specially in the UVB arm and CIV emission line. Figure 4.10 shows a region in the UVB with marked absorption lines at (1391,1400,1439,1462,1464,1516,1535,1555,1559,1575,1578) Å. The broad absorption at 1540 Å could classify this system as a broad absorption line (BAL) quasar, which shows blueshifted absorptions due to fast and massive outflows (e.g. Hamann et al. 2019, Hutsemékers et al. 2020).

Five prominent emission lines were identified in this system (CIV, CIII, MgII,  $H\beta$  and  $H\alpha$ ) with high S/N. I de-magnified the spectra using the magnification values from Sluse et al. 2012 and subtracted the continuum to analyze the profiles of image A and B (Fig. 4.11).

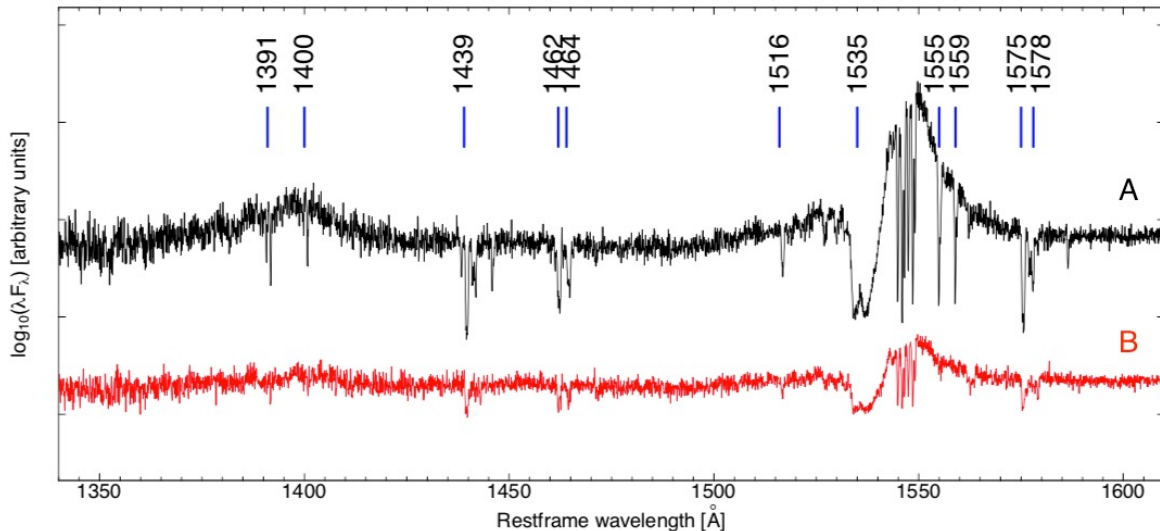


FIGURE 4.10: Part of the UVB spectra of the system LBQS1333+0113 showing absorption features in CIV.

The left wing of MgII profile is enhanced in the BEL of image B compared to image A which could be produced by microlensing. A strong absorption in CIV and a profile distortion in H $\alpha$  are detected. Notice that the distortion of H $\alpha$  line profiles is also seen in the 2D and 1D reduction obtained from ESO Phase 3 (Fig. 4.12), thus this is not an artifact of the spectrum extraction. The ESO Phase 3 is the process of preparation and validation of the data products in the ESO science archive facility after an OB was observed. The absorptions observed in Fig. 4.12 might be due to a strong telluric absorption residual in the center of the emission line that *molecfit* was unable to correct.

#### 4.3.1.2 Q1355-2257

First named as CTQ 327, it was discovered by [Morgan et al. 2003](#) during a Hubble Space Telescope Imaging Spectrograph snapshot survey for small-separation gravitational lenses, with a source redshift of  $z_s = 1.37$  and a separation of  $1.23''$ . The lens redshift was measured by [Eigenbrod et al. 2006](#) ( $z_l = 0.701$ ) using Deep VLT/FORS1 spectra. Image of this system is shown in fig. 4.13.

[Sluse et al. 2012](#) obtained the  $M_{\text{BH}}$  using MgII emission line, providing a lens model with the magnification for each image (table 3.1) and it also have possible microlensing in the emission lines. More recently, [Rojas et al. 2020](#) concluded that the system shows chromatic microlensing and estimated for the first time the accretion disk size and temperature profile.

<sup>1</sup><https://www.eso.org/sci/observing/phase3.html>

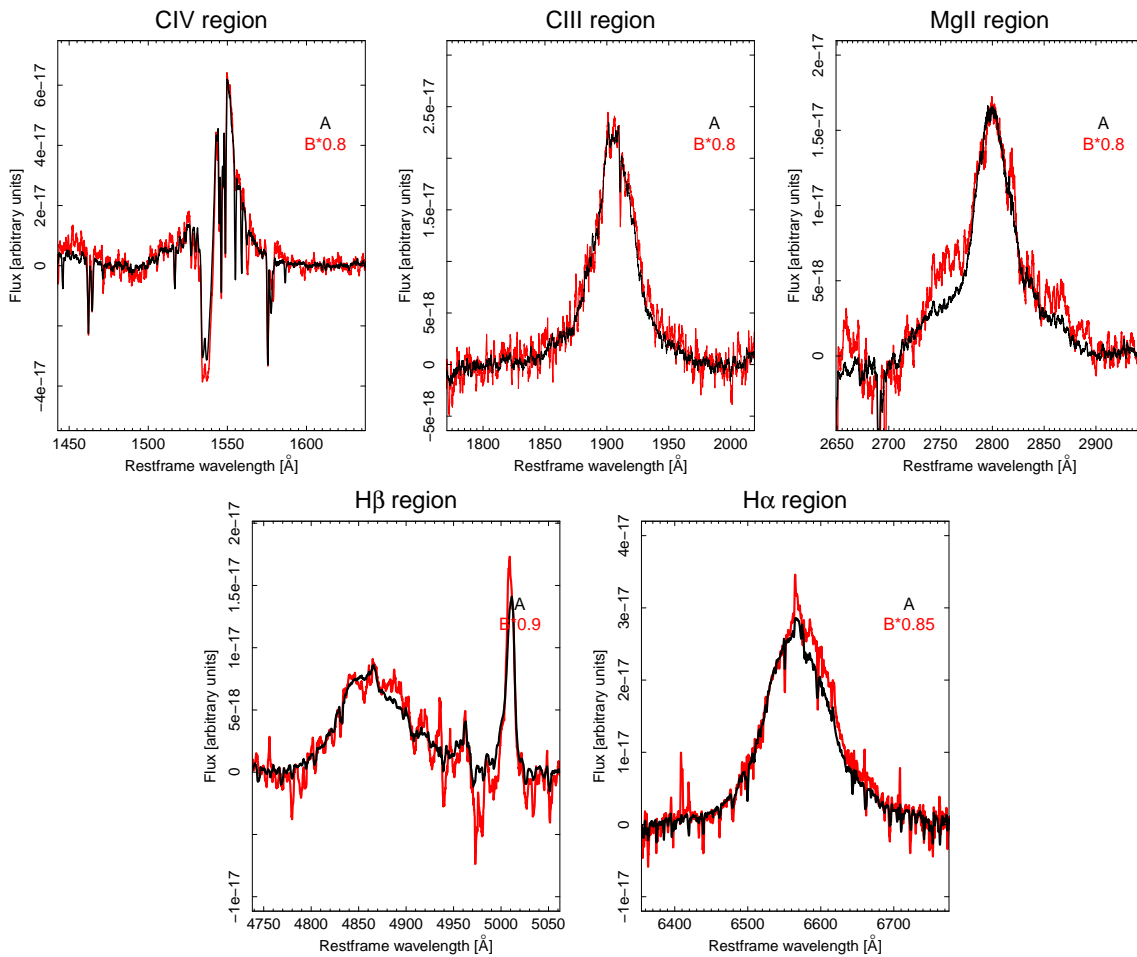


FIGURE 4.11: CIV, CIII, MgII H $\beta$  and H $\alpha$  emission line profiles for LBQS1333+0113. The images are demagnified using the magnification values  $\mu_A = 3.77$  and  $\mu_B = 0.87$  obtained from Sluse et al. 2012. Notice that H $\alpha$  and MgII shows profile difference between both images.

The line profiles of image A and B were analyzed subtracting the continuum as described in section 3.3 (fig. 4.14). In general, the X-shooter profiles do not show any difference, except in the right wing of CIV emission line. Our H $\beta$  emission line have a slight discrepancy due to the low S/N (see table 4.6) and H $\alpha$  shows also a distortion due to telluric absorption.

#### 4.3.1.3 QJ0158-4325

It was originally identified in the Calán-Tololo Quasar survey by Maza et al. 1995 and then confirmed as a lensed quasar by Morgan et al. 1999 with a source redshift  $z_s=1.29$  and a separation of  $1.22''$ . This system has been widely monitored because it has microlensing effect in the continuum (Chen et al. 2012, Morgan et al. 2012, Chartas et al. 2017, Paic et al. 2022).

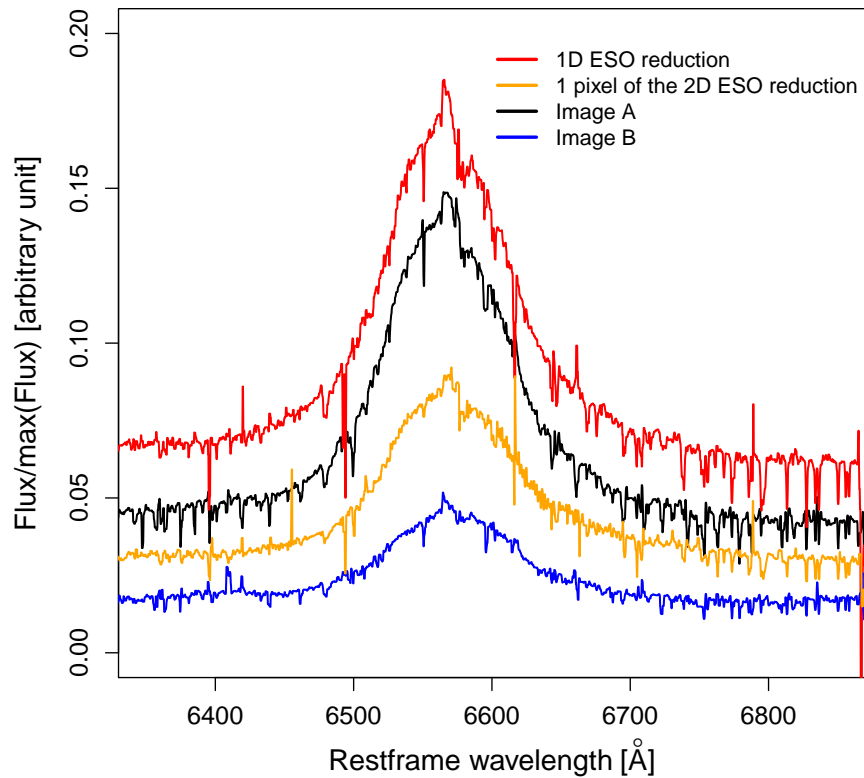


FIGURE 4.12:  $H\alpha$  profile comparison between the ESO phase 3 and my reduction and extraction of image A and B. The distortion observed in the peak is due to a poor telluric correction.

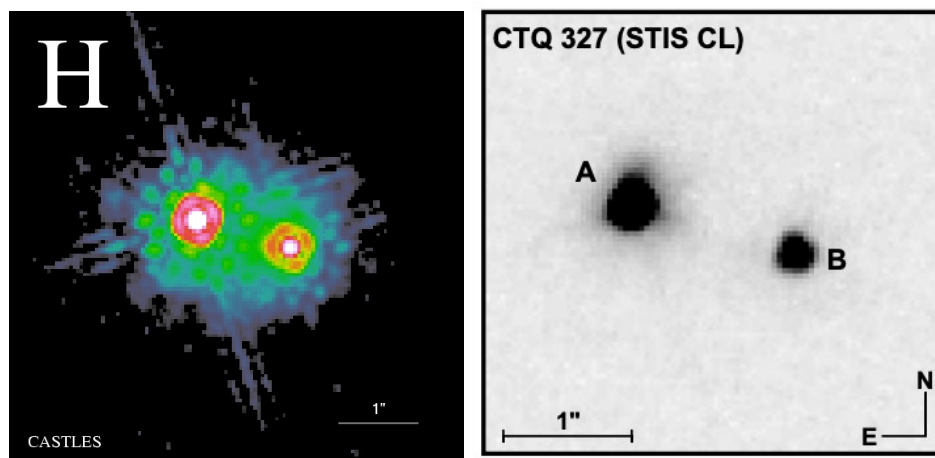


FIGURE 4.13: Images of the system Q1355-2257. Left: HST images in filter F160W obtained from CASTLES. Right: Image of three exposures taken with HST STIS from [Morgan et al. 2003](#)

Figure 4.15 shows an image of this double system. The time delay was found to be  $\Delta t_{AB} = 22.7 \pm 3.6$  days using light curves observed by the Leonhard Euler 1.2 m Swiss Telescope

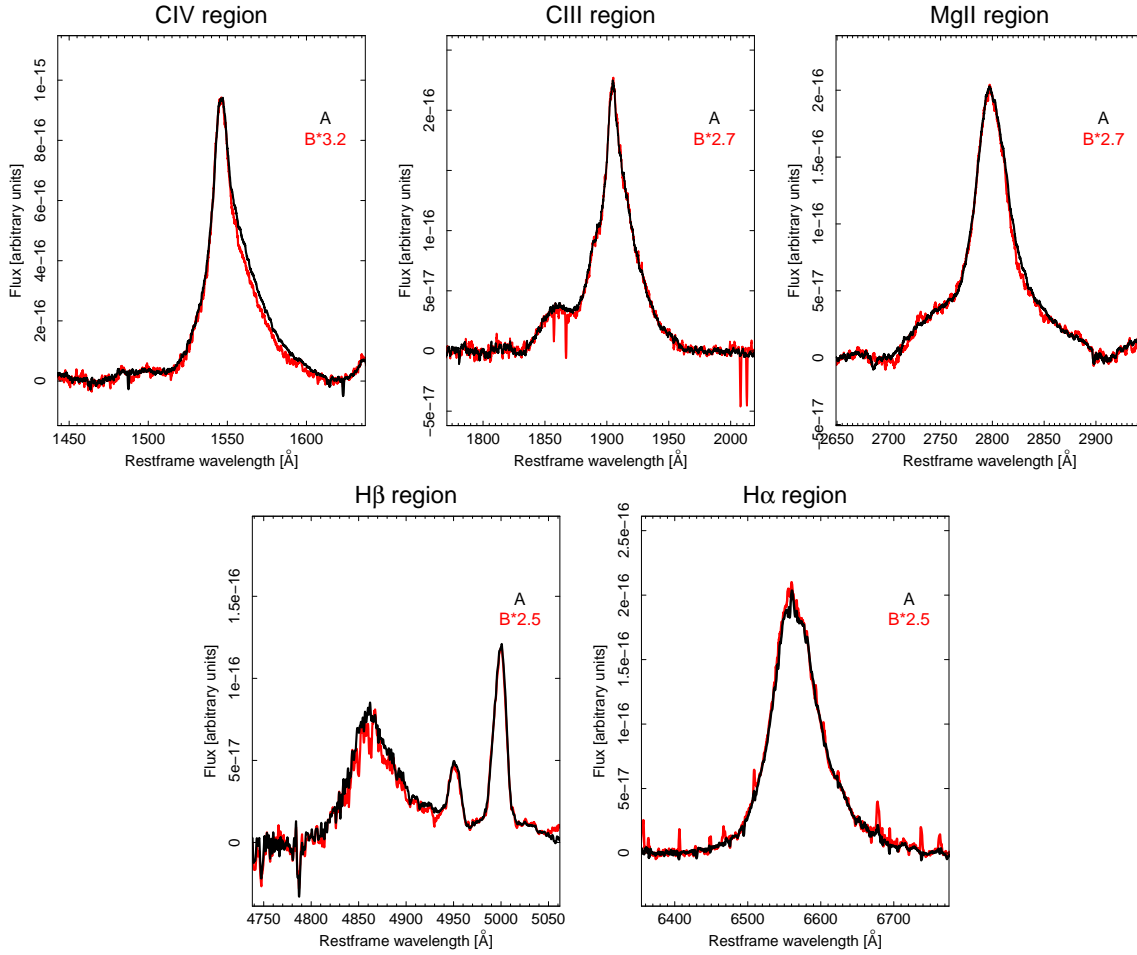


FIGURE 4.14: CIV, CIII, MgII H $\beta$  and H $\alpha$  emission line profiles for Q1355-2257.

(COSMOGRAIL programme, [Millon et al. 2020b](#)). [Paic et al. 2022](#) observed for the first time the continuum reverberation by the BLR in a single waveband photometric light. They also measure the size of the BLR ( $R_{BLR} = 1.6_{-0.8}^{+1.5} \times 10^{17}$  cm).

The line profiles of image A and B are presented in fig. 4.16. A small discrepancy is seen in the right wing of MgII ( $m_B - m_A = -0.82 \pm 0.23$  mag in the region [2812:2832] Å), CIII ( $m_B - m_A = -0.89 \pm 0.14$  mag in [1915:1935] Å), and H $\alpha$  emission line ( $-0.86 \pm 0.35$  mag in [6590:6625] Å). The left wing of CIII and MgII is also different between both images. As mentioned before for the other systems, the peak of H $\alpha$  emission line shows an artifact due to a poor telluric absorption correction.

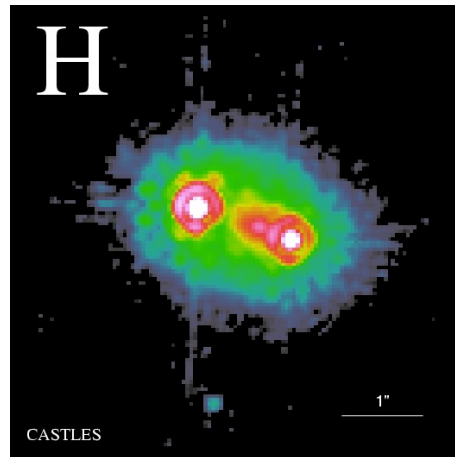


FIGURE 4.15: HST image of QJ0158-4325 in filter F160W obtained from CASTLES.

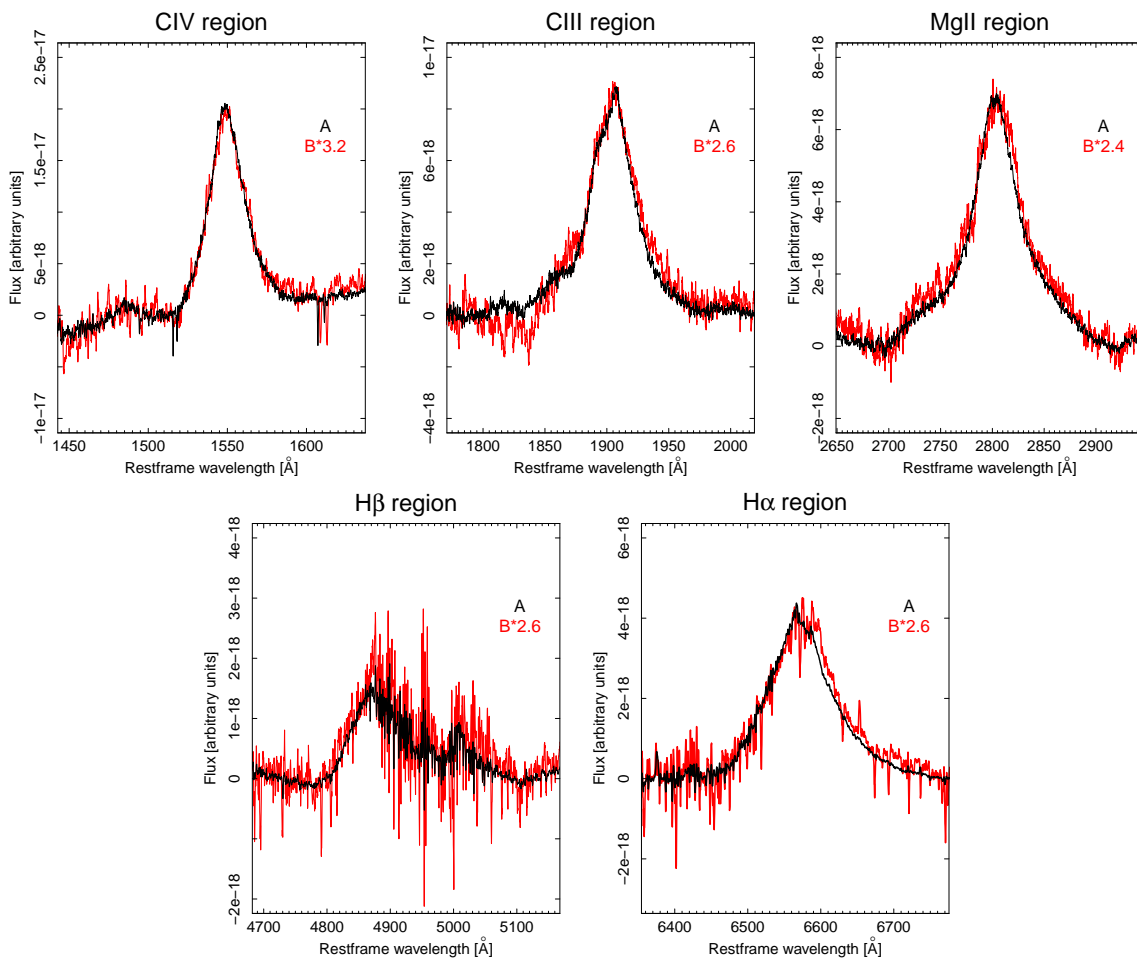


FIGURE 4.16: CIV, CIII, MgII H $\beta$  and H $\alpha$  emission line profiles for QJ0158-4325. The images are demagnified using the magnification values  $\mu_A = 25.27$  and  $\mu_B = 12.31$  obtained from [Bhatiani et al. 2019](#).

### 4.3.2 Microlensing Analysis

To investigate if microlensing is present, I obtained the magnitude difference  $m_B - m_A$  for the three systems (figure 4.17, figure 4.18 and figure 4.19) as explained in section 3.3. The integration windows used to obtain the area under the curve for the continuum ( $m_B - m_A$ )<sup>cont</sup>, and the core of the emission line ( $m_B - m_A$ )<sup>line</sup> are shown in Table 4.3, 4.4, 4.5 for LBQS1333+0113, Q1355-2257 and QJ0158-4325, respectively. The three systems show chromatic microlensing that will be used to obtain the accretion disk size and temperature profile.

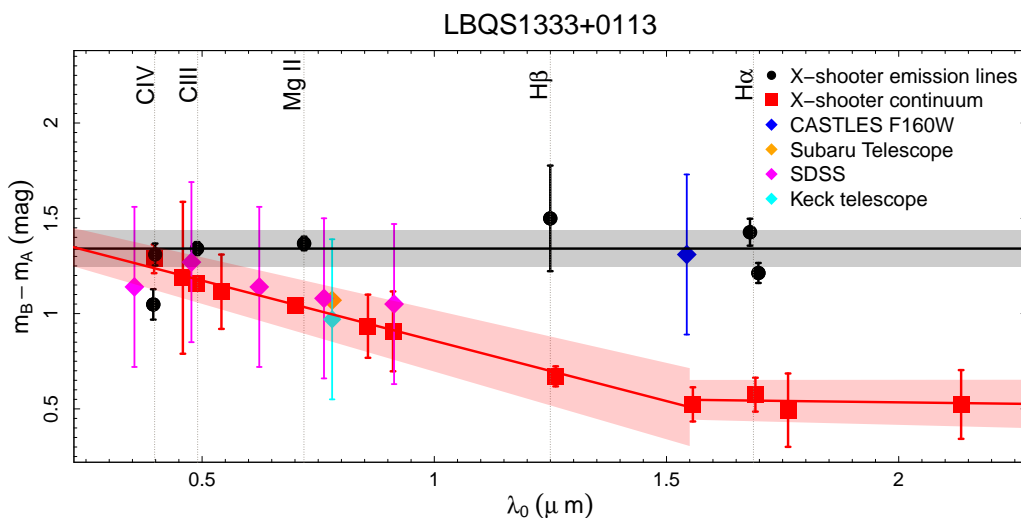


FIGURE 4.17: Magnitude difference  $m_B - m_A$  vs  $\lambda_0$  between images A and B of LBQS1333+0113. Red squares shows the integrated continuum and the black circles the emission line core without the continuum. We include measurements obtained from [Oguri et al. 2004](#): Subaru 8.2-m telescope in i band (orange diamond), Sloan Digital Sky Survey (SDSS) in u, g, r i z bands (magenta diamonds) and Keck telescope in K band (cyan diamond). We included one value from the Hubble Space Telescope (HST) in the H band (obtained from CASTLES). The red line is the best fit for the continuum and the dashed red line the standard deviation, the black line is the median for the emission line core and the blue line for the literature.

For the  $H\alpha$  emission line of LBQS1333+0113 we considered two values left and right of the line to avoid the distortion in the middle (see table 4.3). In QJ0158-4325 we considered as the baseline CIV, CIII, MgII and  $H\alpha$  emission line core data, excluding  $H\beta$  because it has low S/N.

For the three systems the magnitude difference in the emission lines is approximately constant, and we consider the median and its standard error as the baseline of no microlensing. The  $\langle \Delta m \rangle^{\text{line}}$  are  $1.34 \pm 0.1$  mag,  $1.07 \pm 0.11$  mag and  $1.85 \pm 0.08$  mag for LBQS1333+0113, Q1355-2257 and QJ0158-4325 respectively.

Data from the literature are included in all the figures (mentioned in the captions), which are mostly in agreement with the X-shooter data. In Q1355-2257 (figure 4.18) I plotted the previous analysis made by [Rojas et al. 2020](#). This is consistent with our data even though there is a difference of 0.17 mag in the no-microlensing baseline between the fit of X-shooter and [Rojas et al. 2020](#) ( $1.24 \pm 0.04$  mag), probably because we have measurements for more emission lines.

The three systems show a slope in the continuum, that confirms chromatic microlensing. A negative slope can be seen in the fit of the continuum in figure 4.17 for LBQS1333+0113, which then becomes constant. This slope could be explained with chromatic microlensing on both components (similar as previously seen in HE1104-1805 [Motta et al. 2012](#)), and in the NIR there is no longer chromaticity, just microlensing. The continuum is in agreement with optical broadband from SDSS and Keck telescope and the slope becomes constant at approximately  $1.5 \mu\text{m}$ .

The continuum of Q1355-2257 from the X-shooter data has changed over time (see fig. 4.18), as previously confirmed by [Rojas et al. 2020](#) (with data taken in 2008 by the Very Large Telescope/FOcal Reducer and low dispersion Spectrograph VLT/FORS2, ID: 381.A0508).

As in the previous case, QJ0158-4325 shows a slope up to approximately  $1 \mu\text{m}$  and then become constant. Data from the literature is in agreement with the X-shooter data in the MgII region, where both the continuum and emission line coincide. Notice that the broadband photometry from CASTLES and CHANDRA follows the constant slope.

---

TABLE 4.3: Magnitude difference of LBQS1333+0113.

Region	$\lambda_c(\text{\AA})$	Window ( $\text{\AA}$ )	$m_B - m_A$ (mag)
Line	CIV	1550 - 1554	$-1.34 \pm 0.01$
	CIV absorption	1534 - 1539	$-1.05 \pm 0.16$
	CIII	1897 - 1909	$-1.34 \pm 0.07$
	MgII	2793 - 2807	$-1.39 \pm 0.16$
	H $\beta$	4845 - 4880	$-1.50 \pm 0.55$
	H $\alpha$	6526 - 6546	$-1.43 \pm 0.14$
	H $\alpha$ right wing	6598 - 6615	$-1.21 \pm 0.10$
Continuum	1544	1473 - 1614	$-1.29 \pm 0.15$
	1784	1769 - 1800	$-1.19 \pm 0.80$
	1895	1800 - 2000	$-1.15 \pm 0.04$
	2107	2080 - 2135	$-1.11 \pm 0.39$
	2732	2533 - 2930	$-1.04 \pm 0.02$
	3335	3290 - 3380	$-0.93 \pm 0.33$
	3545	3515 - 3575	$-0.91 \pm 0.42$
	4908	4730 - 5086	$-0.67 \pm 0.10$
	6058	5955 - 6160	$-0.52 \pm 0.18$
	6582	6368 - 6795	$-0.57 \pm 0.18$
	6855	6810 - 6900	$-0.49 \pm 0.38$
8305	8190 - 8420	$-0.52 \pm 0.36$	

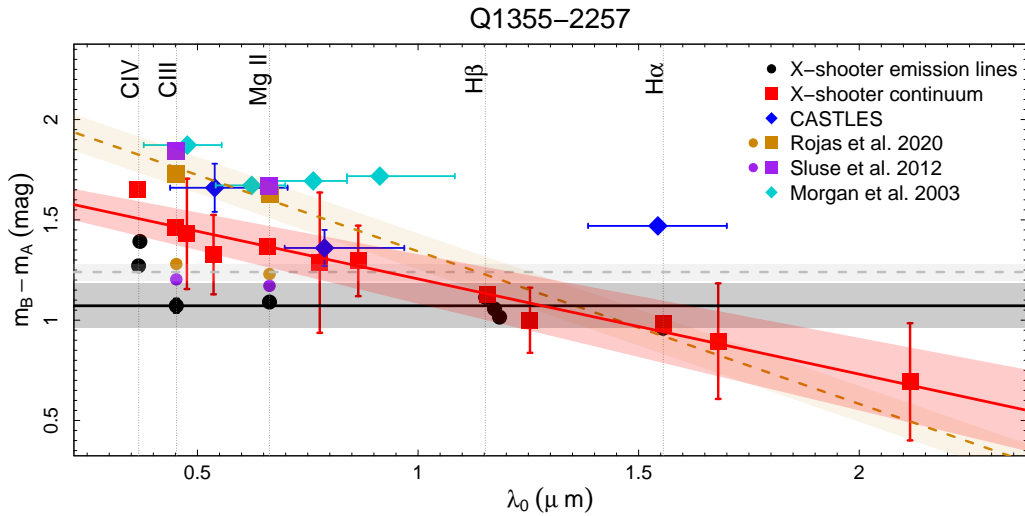


FIGURE 4.18: Magnitude difference  $m_B - m_A$  vs wavelength at restframe  $\lambda_0$  between images A and B of Q1355-2257. Red squares shows the integrated continuum and the black circles the emission line core without the continuum. We include measurements obtained from the literature: HST<sup>2</sup> in filters F160W, F555W and F814W (blue diamonds); g, r, i, and z filters of the Sloan digital Sky Survey (SDSS) from [Morgan et al. 2003](#) (cyan diamonds); spectroscopic data from [Sluse et al. 2012](#) (purple square and circle for the continuum and emission line, respectively) and spectroscopic data from [Rojas et al. 2020](#) of the VLT/FORS2 (orange square and circle for the continuum and emission line, respectively). The red and black line is the fit of the continuum and emission line core, and the red and black shaded area the standard deviation, respectively. The grey dashed line is the fitting for the core of the emission line and in orange dashed line for the continuum presented in [Rojas et al. 2020](#) along with their errors as the shaded area.

TABLE 4.4: Magnitude difference for Q1355-2257.

Region	$\lambda_c(\text{\AA})$	Window ( $\text{\AA}$ )	$m_B - m_A$ (mag)
Line	CIV	1542 - 1551	$-1.27 \pm 0.02$
	CIV right wing	1555 - 1564	$-1.39 \pm 0.02$
	CIII	1901 - 1914	$-1.07 \pm 0.07$
	MgII	2786 - 2811	$-1.09 \pm 0.03$
	H $\beta$	4858 - 4874	$-1.11 \pm 0.02$
	OIII <sub>1</sub>	4946 - 4956	$-1.06 \pm 0.05$
	OIII <sub>2</sub>	4994 - 5004	$-1.01 \pm 0.01$
	H $\alpha$	6546 - 6581	$-0.96 \pm 0.01$
Continuum	1538	1452 - 1624	$-1.65 \pm 0.04$
	1895	1790 - 2000	$-1.46 \pm 0.03$
	2008	1987 - 2030	$-1.43 \pm 0.56$
	2264	2240 - 2287	$-1.33 \pm 0.39$
	2784	2648 - 2920	$-1.37 \pm 0.02$
	3279	3254 - 3304	$-1.29 \pm 0.70$
	3648	3607 - 3688	$-1.29 \pm 0.35$
	4885	4615 - 5155	$-1.13 \pm 0.07$
	5290	5185 - 5395	$-0.99 \pm 0.32$
	6562	6368 - 6757	$-0.98 \pm 0.07$
	7090	6990 - 7190	$-0.89 \pm 0.58$
	8925	8800 - 9050	$-0.69 \pm 0.58$

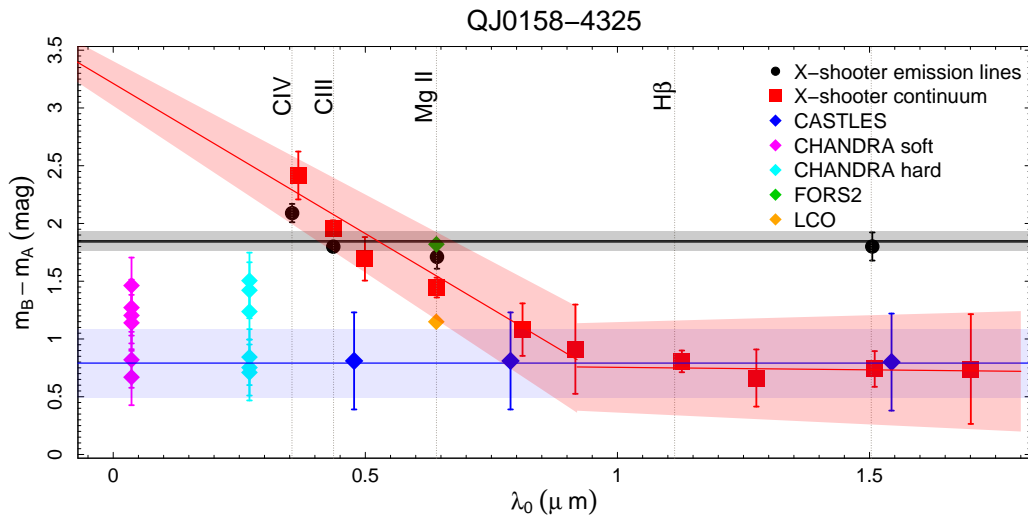


FIGURE 4.19: Magnitude difference  $m_B - m_A$  vs  $\lambda_0$  between images A and B of QJ0158-4325. Red squares shows the integrated continuum and the black circles the emission line core. I included measurements obtained from the literature: HST (Morgan et al. 2003/CASTLES; blue diamonds), hard X-ray (cyan diamond) and soft X-ray data (magenta diamond) from CHANDRA telescope (Chen et al. 2012), VLT/FORS2 from Faure et al. 2009 (green diamond) and Las Campanas Observatory (LCO) from Morgan et al. 1999 (orange diamond). The Red line is the fit of the continuum and the shaded red area the standard deviation, the black line is the median for the emission line core and the blue line for the HST data.

TABLE 4.5: Magnitude difference of QJ0158-4325.

Region	$\lambda_c(\text{\AA})$	Window ( $\text{\AA}$ )	$m_B - m_A$ (mag)
Line	CIV	1542 - 1557	$2.09 \pm 0.16$
	CIII	1900 - 1912	$1.80 \pm 0.09$
	MgII	2788 - 2820	$1.71 \pm 0.20$
	H $\beta$	4855 - 4905	$1.62 \pm 0.55$
	H $\alpha$	6546 - 6602	$1.80 \pm 0.24$
Continuum	1603	1506 - 1700	$2.41 \pm 0.41$
	1904	1770 - 2038	$1.96 \pm 0.13$
	2180	2140 - 2220	$1.69 \pm 0.37$
	2802	2680 - 2925	$1.44 \pm 0.17$
	3545	3515 - 3575	$1.08 \pm 0.45$
	4002	3980 - 4025	$0.91 \pm 0.77$
	4925	4700 - 5150	$0.81 \pm 0.19$
	5570	5470 - 5670	$0.66 \pm 0.49$
	6595	6340 - 6850	$0.74 \pm 0.31$
7427	7290 - 7565	$0.74 \pm 0.95$	

### 4.3.3 Black hole mass measurement

Black hole mass ( $M_{BH}$ ) was calculated for the three systems using the FWHM and monochromatic luminosity described in section 3.2 for both images. Since the three systems shows chromatic microlensing in the continuum, we use the luminosity obtained from the SEDs. We used photometric data (where microlensing is constant, not chromaticity) for the three systems. Table 4.6 presents their monochromatic luminosity, FWHM and  $M_{BH}$ . Below I will discuss each system separately.

In the case of LBQS1333+0113 I only used  $H\alpha$  and MgII emission lines, and discarded CIV line because of the absorptions and  $H\beta$  due to the low S/N. The Gaussian fitting can be seen in Fig. 4.20. Masked regions are shown for the  $H\alpha$  region due to the bad telluric correction. I will discuss each system separately. The FWHM for MgII emission line are in agreement within the errors and the  $M_{BH}$  are consistent for both images giving a mean value of  $\log_{10}(M_{BH}) [M_{\odot}] = 8.88 \pm 0.59$ . In the case of the  $H\alpha$  emission line, the luminosity at 5100 Å is larger in image B, but their  $M_{BH}$  are in agreement within their errors, obtaining a mean value for both images of  $\log_{10}(M_{BH}) [M_{\odot}] = 8.64 \pm 0.32$ . The previous measurement for LBQS1333+0113 and Q1355-2257 obtained by [Sluse et al. 2012](#) using MgII emission line ( $\log_{10}(M_{BH}) [M_{\odot}] = 9.19 \pm 0.26$  and  $9.04 \pm 0.34$  respectively) agrees withing the uncertainties with our X-shooter  $M_{BH}$ . This is the first  $M_{BH}$  estimation for QJ0158-4325.

For the system QJ0158-4325 we use  $H\alpha$ , MgII and CIV. Overall, this profiles for the image shows wider FWHM than for image B (probably due to microlensing in the BLR), but both are consistent within 1-sigma error.

We plotted our new measurements in the  $M_{BH}$  vs  $L_{bol}$  (Figure 4.23) along with literature estimations. The  $M_{BH}$  using CIV for QJ0158-4325 and Q1355-2257 is farther out from the other lines estimations, which can confirm that is not a reliable line to obtain the  $M_{BH}$ . There is a tendency into the low-luminosity range (from  $10^{44}$  to  $10^{46.5}$ ) of the diagram, specially with the new two systems that did not have a previously  $M_{BH}$  estimation.

A comparison between the fit of the  $M_{BH}$  using the Balmer lines that exists up to this point and the fit using our new estimations is shown in figure 4.24. It can be observe that the fit with the new  $M_{BH}$  moves to lower luminosities but still following the trend of black hole masses estimates. This analysis will be further explored in the future.

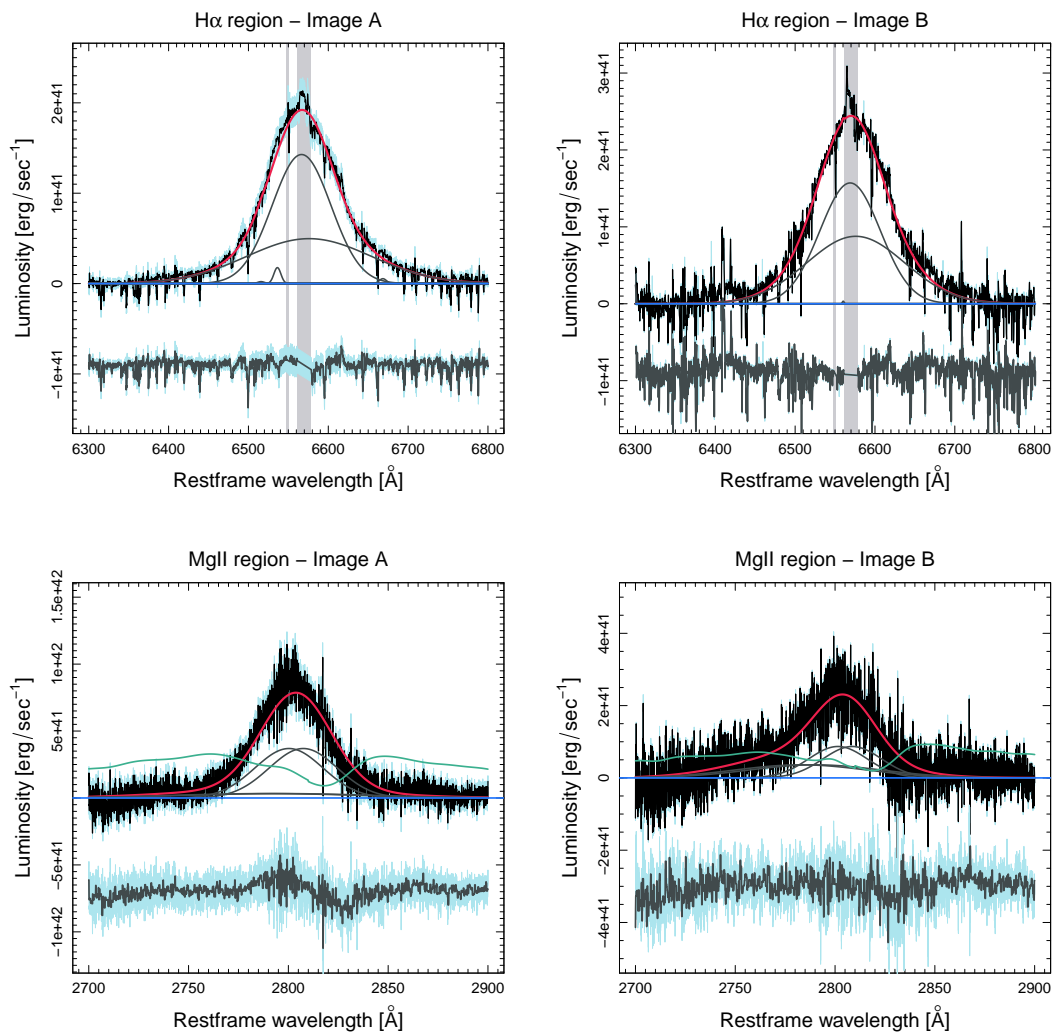


FIGURE 4.20: Gaussian fitting of the broad emission lines for LBQS1333+0113 of images A and B. Red line is the best fit, black lines is the different components of each region, green line represents the Fe template and the blue line is the continuum fit of the spectra. In the bottom of the images is the 1-sigma error of the spectra along with the residuals.

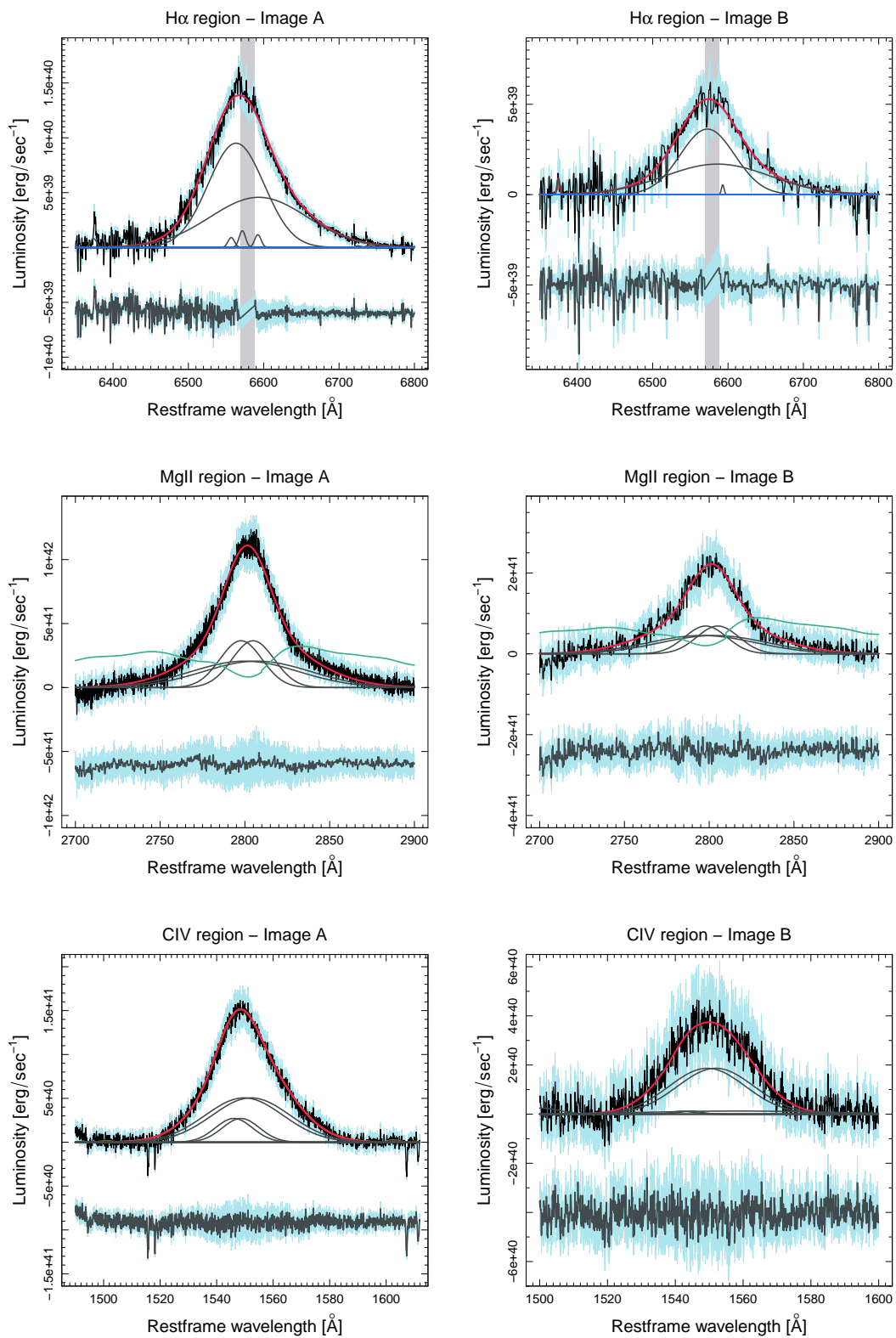


FIGURE 4.21: Gaussian fitting of the broad emission lines for QJ0158-4325 of images A (left) and B (right). Red line is the best fit, black lines is the different components of each region, green line represents the Fe template and the blue line is the continuum fit of the spectra. In the bottom of the images is the 1-sigma error of the spectra along with the residuals.

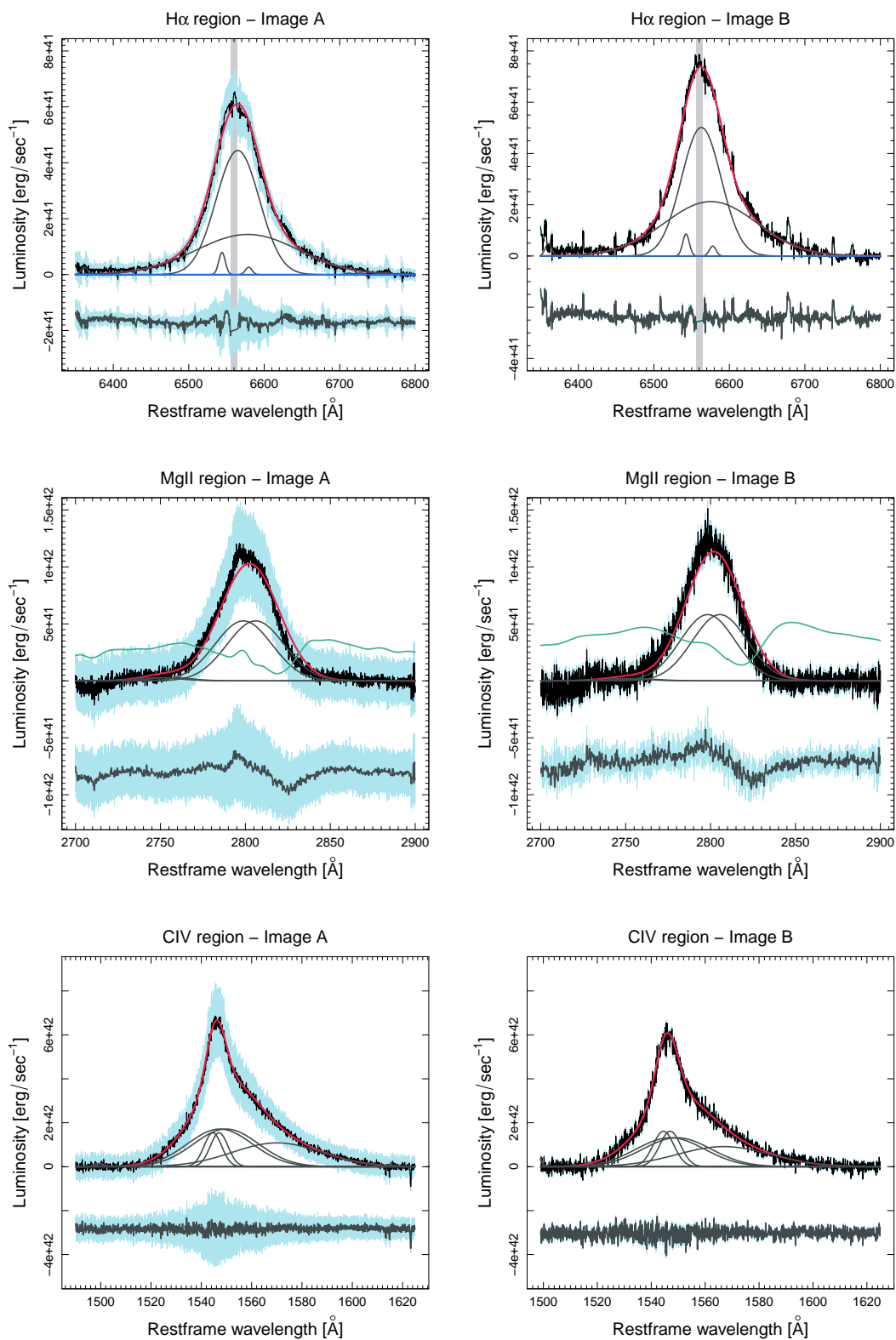


FIGURE 4.22: Gaussian fitting of the broad emission lines for Q1355-2257 of images A and B. Red line is the best fit, black lines is the different components of each region, green line represents the Fe template and the blue line is the continuum fit of the spectra. In the bottom of the images is the 1-sigma error of the spectra along with the residuals.

TABLE 4.6: FWHM, luminosities, and  $M_{BH}$  for the systems.

Image	Line	FWHM [km/s]	$\log_{10}(L_{ref})[\text{erg/s}]^a$	$\log_{10}(M_{BH}) [M_{\odot}]$	$\log_{10}(r_s) [\text{cm}]^b$	S/N Continuum
QJ0158-4325						
A	CIV	$4880.26 \pm 166.63$	$43.80 \pm 0.06$	$7.61 \pm 0.21$	$14.15 \pm 0.85$	11.06
	MgII	$4069.70 \pm 92.59$	$43.87 \pm 0.04$	$8.06 \pm 0.12$	$14.79 \pm 1.09$	18.74
	H $\alpha$	$4865.23 \pm 129.42$	$43.42 \pm 0.10$	$7.84 \pm 0.11$	$15.14 \pm 1.13$	9.63
B	CIV	$5164.00 \pm 334.75$	$43.80 \pm 0.06$	$7.20 \pm 0.54$	$13.88 \pm 0.44$	2.63
	MgII	$4204.90 \pm 204.77$	$43.87 \pm 0.04$	$7.95 \pm 0.24$	$14.72 \pm 0.79$	7.44
	H $\alpha$	$4651.04 \pm 232.36$	$43.42 \pm 0.10$	$7.79 \pm 0.34$	$15.11 \pm 0.64$	5.80
LBQS1333+0113						
A	MgII	$4521.71 \pm 69.38$	$44.93 \pm 0.02$	$8.80 \pm 0.20$	$15.29 \pm 0.87$	15.80
	H $\alpha$	$4608.55 \pm 69.73$	$44.51 \pm 0.05$	$8.50 \pm 0.15$	$15.58 \pm 1.00$	8.47
B	MgII	$4508.73 \pm 29.97$	$44.93 \pm 0.02$	$8.96 \pm 0.56$	$15.39 \pm 0.42$	8.79
	H $\alpha$	$4754.73 \pm 23.66$	$44.51 \pm 0.05$	$8.79 \pm 0.28$	$15.77 \pm 0.73$	8.56
Q1355-2257						
A	CIV	$2939.65 \pm 254.82$	$45.38 \pm 0.04$	$8.12 \pm 0.17$	$14.49 \pm 0.94$	9.69
	MgII	$4254.30 \pm 74.41$	$45.23 \pm 0.01$	$8.93 \pm 0.20$	$15.37 \pm 0.87$	23.34
	H $\alpha$	$3620.07 \pm 65.09$	$44.76 \pm 0.17$	$8.45 \pm 0.09$	$15.55 \pm 1.22$	23.84
B	CIV	$2702.83 \pm 120.74$	$45.38 \pm 0.04$	$7.91 \pm 0.18$	$14.35 \pm 0.92$	3.41
	MgII	$4118.03 \pm 106.32$	$45.23 \pm 0.01$	$8.81 \pm 0.06$	$15.29 \pm 1.39$	10.40
	H $\alpha$	$3442.36 \pm 108.17$	$44.76 \pm 0.17$	$8.46 \pm 0.13$	$15.55 \pm 1.06$	14.14

**Notes.** <sup>(a)</sup>  $L_{ref}$  = Luminosity ( $L_{1450}$ ,  $L_{3000}$ ,  $L_{5100}$ ) for  $\text{CIV}$ ,  $\text{MgII}$  and  $\text{H}\alpha$  respectively. <sup>(b)</sup>  $r_s$  is the accretion disk size obtained from equation 3.6 at the  $\lambda_{rest}$  of the emission line used for the  $M_{BH}$  measurement.

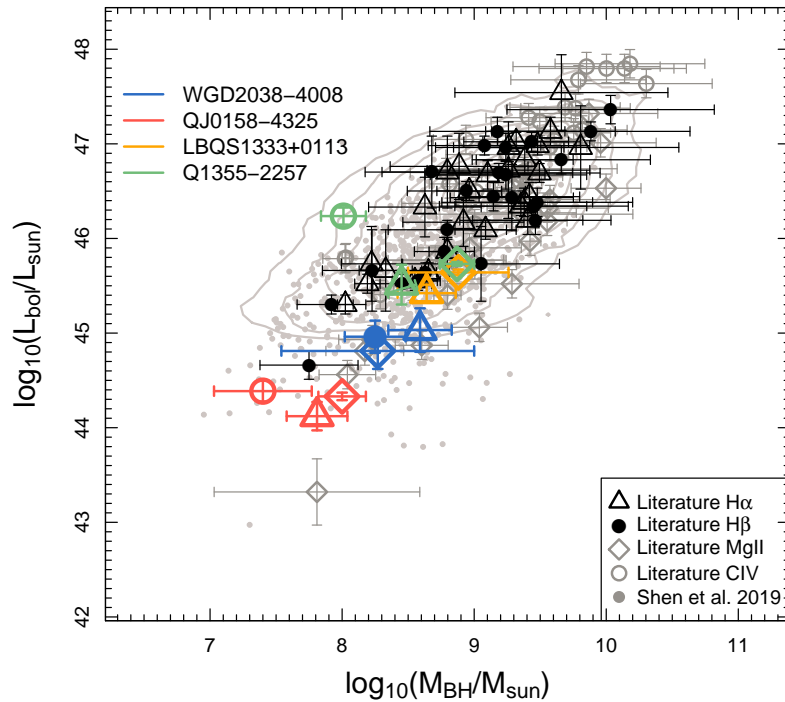


FIGURE 4.23:  $M_{BH}$  vs  $L_{bol}$  for quasars. Masses of lensed quasars are plotted from different emission lines and luminosities that exists upto date (Peng et al. 2006b, Assef et al. 2011, Sluse et al. 2012, Ding et al. 2017a). The new measurements of the four lensed systems using X-shooter are presented in different colors.

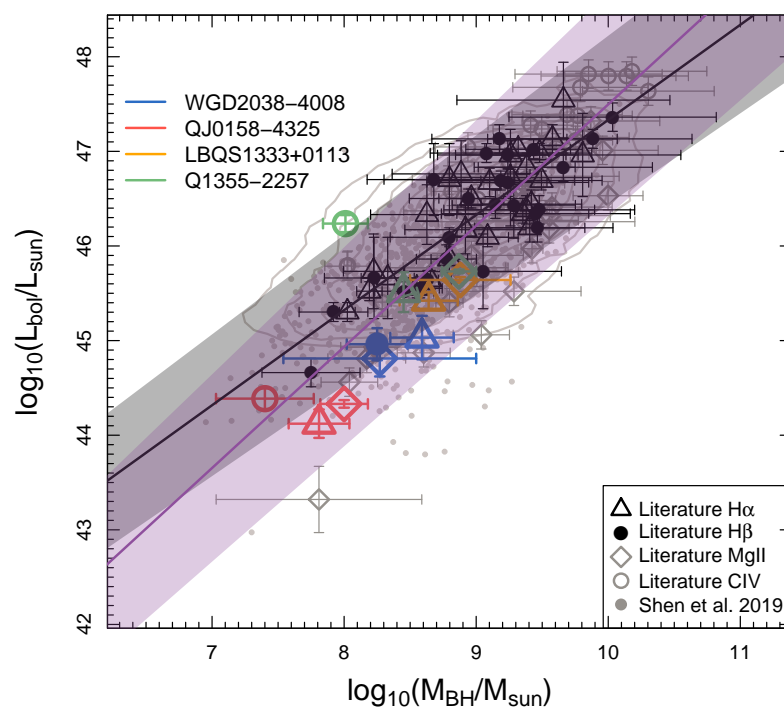


FIGURE 4.24:  $M_{BH}$  vs  $L_{bol}$  for quasars. The gray fit is the  $H\alpha$  and  $H\beta$  values that exists in the literature up to date (Peng et al. 2006b, Assef et al. 2011, Sluse et al. 2012, Ding et al. 2017a), while the purple fit adding our new Balmer estimates from the four double systems. Masses of lensed quasars are plotted from different emission lines and luminosities. The new measurements of the four lensed systems using X-shooter are presented in different colors.

### 4.3.4 Accretion disk size estimation

As the magnitude difference between the core of the emission line and the continuum changes with wavelengths, this is evidence of chromatic microlensing and we can estimate the size and temperature profile of the accretion disk following the procedure in section 3.4.1. I obtained the magnitude difference  $\Delta m = (m_B - m_A)^{\text{cont}} - (m_B - m_A)^{\text{line}}$  in three different rest frame wavelengths (Table 4.7). The wavelengths chosen for Q1355-2257 are the same as in [Rojas et al. 2020](#) for comparison purposes. Microlenses of  $1 M_\odot$  and a mass fraction in stars on 0.1 were considered for the model ([Mediavilla et al. 2009](#), [Pooley et al. 2009](#)). The size of the map is  $1000 \times 1000$  pixels<sup>2</sup> for each system. The estimations were obtained at rest frame wavelengths  $\lambda_{ref} = 1026 \text{ \AA}$  to compare with previous results obtained by [Jiménez-Vicente et al. 2014](#). The probability density function of the accretion disk size  $r_s$  and  $p$  for the three systems is shown in appendix. C and their values at  $1\sigma$  in table 4.8 ( $r_s \propto p$ ).

System	Wavelength [ $\text{\AA}$ ]	$\Delta m$ [mag]
QJ0158-4325	1550	$0.44 \pm 0.31$
	2800	$-0.30 \pm 0.39$
	3545	$-0.75 \pm 0.43$
LBQS1333+0113	1550	$-0.10 \pm 0.11$
	2800	$-0.31 \pm 0.11$
	4860	$-0.64 \pm 0.13$
Q1355-2257	4400	$0.32 \pm 0.14$
	6200	$0.23 \pm 0.15$
	7300	$0.18 \pm 0.15$

TABLE 4.7: Chromatic microlensing  $\Delta m$  for three different wavelengths for each system.

System	$r_{s-model}$ [ $\sqrt{M/M_\odot}$ light days] <sup>a</sup>	$p$	$r_s$ [light days] <sup>b</sup>
QJ0158-4325	$14.28^{+7.42}_{-4.88}$	$1.94 \pm 0.32$	$0.16^{+0.22}_{-0.11}$
LBQS1333+0113	$10.97^{+8.29}_{-4.72}$	$1.33 \pm 0.45$	$1.22^{+1.46}_{-1.01}$
Q1355-2257	$2.59^{+2.52}_{-1.28}$	$0.39 \pm 0.31$	$0.48^{+0.73}_{-0.32}$

**Notes.** <sup>(a)</sup> From the model of chromatic microlensing. <sup>(b)</sup> Average value from table 4.6.

TABLE 4.8:  $p$  and the accretion disk size from the model and from equation 3.6.

This is the first estimation of the size and temperature profile  $p$  using microlensing for the systems LBQS1333+0118 and QJ0158-4325. The estimated value of Q1355-2257 is in agreement within the errors with the one obtained by [Rojas et al. 2020](#) ( $r_s = 3.6^{+3.0}_{-1.6} \sqrt{M/M_\odot}$  lt-d). In general, our values are larger than the theoretical ( $r_s \sim 0.3 \sqrt{M/M_\odot}$  lt-d) assuming a  $p = 4/3$  and a  $M_{BH} = 1.1 \times 10^9$ ,  $L/L_E = 0.1$  and  $\eta = 0.1$  ([Sluse et al. 2012](#)). This is because the single-epoch studies on individual systems will probable overestimate or underestimate

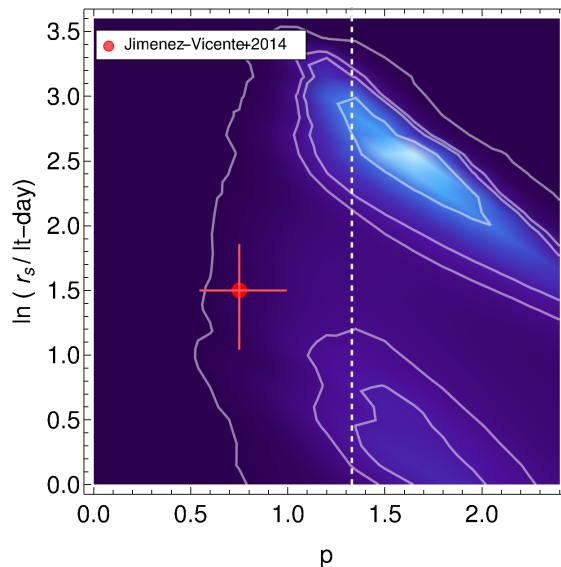


FIGURE 4.25: Combined probability function for the three systems. The accretion disk size and temperature profile from [Jiménez-Vicente et al. 2014](#) is also plotted.

the accretion disk size depending how large is the chromatic microlensing effect ([Guerras et al. 2017, 2020](#)). The solution is to combine several epochs of one system, or several systems of accretion disk sizes ([Jiménez-Vicente et al. 2015](#)). The  $p$  value of LBQS1333+0113 is in agreement within errors with the [Shakura & Sunyaev 1973](#), but for the other two systems the difference is  $\geq 2\sigma$ .

The resulting joint likelihood for the three systems is shown in Figure 4.25. We combine the measurements following the analysis made by [Jiménez-Vicente et al. 2014](#), where they combine eight systems at  $1026 \text{ \AA}$ . We obtained a  $r_s = 11.94_{-6.93}^{+16.56} \text{ lt-d}$  and  $p = 1.65 \pm 0.30$ . A secondary maximum is observed in the figure, that could be because of the complexity of microlensing in one (or more) of the systems ([Motta et al. 2012](#)). Comparing our result with the combined value of [Jiménez-Vicente et al. 2014](#) ( $r_s = 4.48_{-1.62}^{+0.72} \text{ lt-d}$  and  $p = 0.75 \pm 0.2$ ), we conclude that our  $r_s$  agrees within the error. The  $p$  value is larger in our estimation, but it agrees with the theoretical value ([Shakura & Sunyaev 1973](#)). The second single-epoch of Q1355-2257 ([Rojas et al. 2020](#)) can increase the reliability of this study along with a larger lens sample.

In addition, the accretion disk size was estimated using the  $M_{BH}$  (section 4.3.3) and equation 3.6. The average accretion disk size for the three system is shown in the third column of table 4.8. As mentioned previously by [Edelson et al. 2019](#), we found that the accretion disk size estimated by microlensing disagrees with the one estimated using  $M_{BH}$ .

### 4.3.5 Conclusions

This is the first detailed analysis that has been made for three double lensed systems to investigate the structure of an AGN using simultaneously two different methods.

X-shooter data allow us to obtain broad emission lines for each system and measure the black hole mass using CIV, MgII and H $\alpha$  broad emission lines with the single-epoch method. The monochromatic luminosity at 1450, 3000 and 5100 Å was calculated from the SED from photometric data for the systems. For the first time, the  $M_{BH}$  was estimated for QJ0158-4325. Our new measurements follow the  $M_{BH}$  vs  $L_{bol}$  ( $10^{44}$  to  $10^{46.5}$ ) relation for lensed and non-lensed AGNs and the systems lay in the low-luminosity region.

The three systems present chromatic microlensing, allowing us to estimate the accretion disk size using another technique. The resulting joint likelihood for the three systems result in an accretion disk size of  $r_s = 11.94_{-6.93}^{+16.36}$  lt-d and  $p = 1.65 \pm 0.30$ . Our  $r_s$  is in agreement with [Jiménez-Vicente et al. 2014](#), but  $p$  is larger, and we present larger values than the theoretical predicted by the standard thin accretion disk made by ([Shakura & Sunyaev 1973](#),  $r_s \sim 0.3$  lt-d assuming a  $p = 4/3$  and  $1 M_{\odot}$ ). The accretion disk size measured with the  $M_{BH}$  (equation 3.6) is larger than with chromatic microlensing, which is logical due that the single-epoch studies overestimate or underestimate the accretion disk size due to microlensing.

This paper is in preparation that will be send to an international journal in the second half of 2022.

# Chapter 5

## Conclusion

The remarkable discovery that the supermassive black hole mass correlates with the velocity dispersion, luminosity, and mass of the bulge gave a hint of a relationship between the SMBH growth and the coevolution with their host galaxies. To understand this relation we need to trace this correlations to early epochs, and measure the growth rate of the black holes and stellar bulges (Peng et al. 2006b). Unfortunately, the RM method used to measure the black hole masses is limited to low redshift sources and luminosities. The SE method offers an alternative technique to obtain the black hole mass using single epoch spectra of quasars. For low redshift quasars, SE black holes are typically estimated using  $H\alpha$  and  $H\beta$  broad emission lines, but they are shifted into the NIR at higher redshifts. Due to this, the black hole masses are estimated in the optical using  $MgII$  and  $CIV$ , even though this lines may suffer microlensing or wind flows from ejected disk material. Gravitational lensing is a great help in the investigation of the high redshift population, allowing to observe spectra for sources that would be extremely time consuming to obtain.

From the sample of lensed quasars, just 11 systems have black hole masses measured from the Balmer lines, and we wanted to increase that number. In this PhD thesis I studied the inner regions of the AGN under the gravitational lensing effect:

(1) I obtained the black hole mass in a sample of 15 lensed quasars and investigate if they follow the  $M_{BH}$  vs  $L_{bol}$  trend of AGNs. The sample has a luminosity range between  $44.1 \leq \log_{10}(L_{bol}/L_{sun}) \leq 47.6$ . Measurements using  $H\alpha$  and  $H\beta$  emission lines are in agreement with the correlation of lensed and non-lensed AGNs, while  $CIV$  lines are off the trending.

This is a known problem that CIV FWHM width could be affected by wind flows of ejected disk material. The balmer lines continue to be the most reliable  $M_{BH}$  measurements.

(2) I obtained  $M_{BH}$  in the low-luminosity population of lensed and non-lensed AGNs using X-shooter data. The first system studied was WGD2038-4008 using X-shooter instrument, in which we use our own reduction and extraction of each components. In addition to obtaining the  $M_{BH}$ , we could investigate if microlensing was affecting the broad line region or the continuum. The procedure was also made to three double lensed systems, which QJ0158-4325 (first time that  $M_{BH}$  is obtained) also is in the low-luminosity plane.

(3) In the systems where chromatic microlensing was found, the accretion disk size was estimated using a second technique. Our results do not agree with the values obtained using the  $M_{BH}$ . This was expected according to previous publications.

### 5.0.1 Future work

In addition to the two ESO proposals mentioned in this thesis, two more were accepted for the observations of gravitational lensed quasars using X-shooter. We expect to expand our sample of black hole masses and, in addition, we will increase the number of systems that present chromatic microlensing and compare the accretion disk size using both methods. With the increase in the discovery of new lensed quasars, I hope to have more interesting systems to analyze.

---

# Appendix A

## Emission lines fitting parameters

ID	Line	$\lambda$ [Å]	Gaussian component	Flux	Center	FWHM	Flux ratio
Si IV + O IV Region							
1	Si IV	1396.75	Broad	Free	Free	Free	Free
2			Narrow	Free	1	Free	Free
3	O IV]	1402.34	Broad	Free	1	Free	Free
4			Narrow	Free	2	Free	Free
C IV Region							
1	N IV]	1486.5		Free	Free	Free	
2	C IV	1548.2	Narrow	Free	Free	Free	Free
3			Broad	Free	Free	Free	Free
4	C IV	1550.77	Narrow	Free	2	2	1
5			Broad	Free	3	3	1
6	He II	1640.72	Narrow	Free	Free	Free	
7			Broad	Free	6	Free	
8	O III]	1660.8		Free	1	Free	0.29
9		1666.14		8	8	8	0.71
10	N IV	1718.75		Free	Free	Free	Free
C III Region							
1	C III]	1908.73	Narrow	Free	Free	Free	
2			Broad	Free	1	Free	
3	Si III]	1892.03	Narrow	Free	1	1	
4	Si III]		Broad	Free	3	2	
5	Al III	1854.72		Free	1	Free	1
6	Al III	1862.78		5	5	5	1
Mg II Region							

1	Mg II	2795.53	Narrow	Free	Free	Free	2
2			Broad	Free	1	Free	2
3	Mg II	2802.71	Narrow	1	1	1	1
4			Broad	2	2	2	1
5	Fe	Template		Free	Free	Free	
H $\beta$ Region							
1	H $\beta$	4861.32	Narrow	Free	Free	Free	
2			Broad	Free	Free	Free	
3			NLR	Free	4	4	
4	[O III]	5006.84		Free	Free	Free	3
5		4958.91		4	4	4	1
6	He II	4685.65		4	4	4	1
7	Fe II	Template		Free	Free	Free	
H $\alpha$ Region							
1	H $\alpha$	6562.80	Narrow	Free	Free	Free	
2			Broad	Free	Free	Free	
3			NLR	Free	Free	4	
4	[N II]	6548.06		Free	4	[O III] width	1
5		6583.39		4	4	4	3
6	[S II]	6716.47		Free	4	4	1
7		6730.85		6	6	6	1

TABLE A.1: Line regions and adopted constraints used for the line profile fitting. Table adapted from [Mejía-Restrepo et al. 2016](#) (Also seen in Table 4 of [Shang et al. 2007](#)).

# Appendix B

## X-shooter spectra

Rest-frame X-Shooter spectra for the lensed images. The different arms of the instrument are shown: UVB (green), VIS (blue), and NIR (red). The atmospheric windows are left blank for the NIR band. The wavelength is in the rest frame of the respective object and the position of the emission lines are shown as dashed lines.

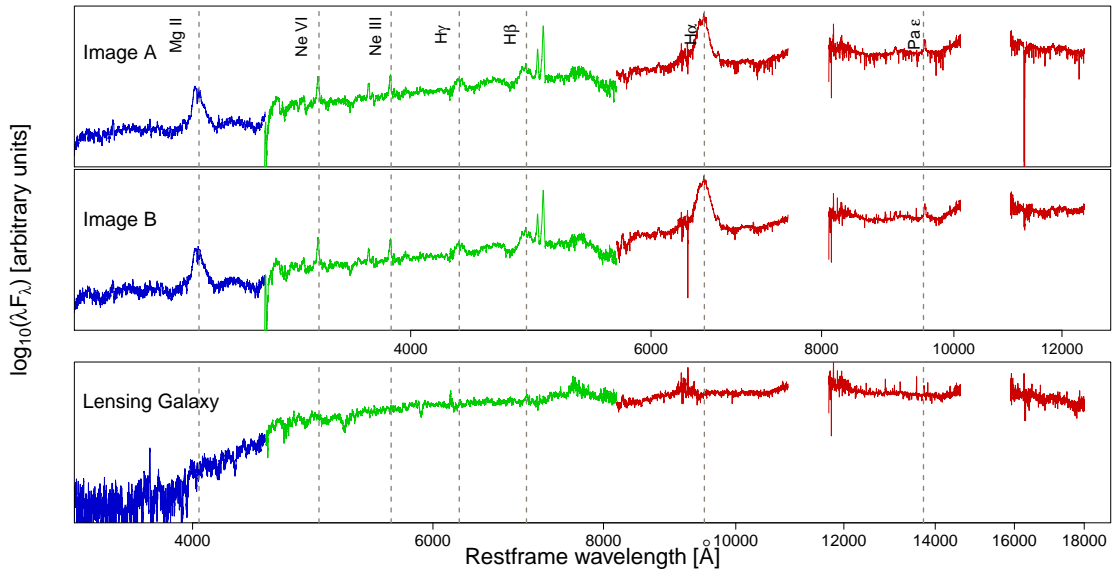


FIGURE B.1: Spectra for image A, image B, and the lensing galaxy of WGD2038-4008. The images are corrected by their respective redshifts ( $z_s = 0.777$  and  $z_l = 0.230$ ). The lensing galaxy is uncontaminated by the quasar emission.

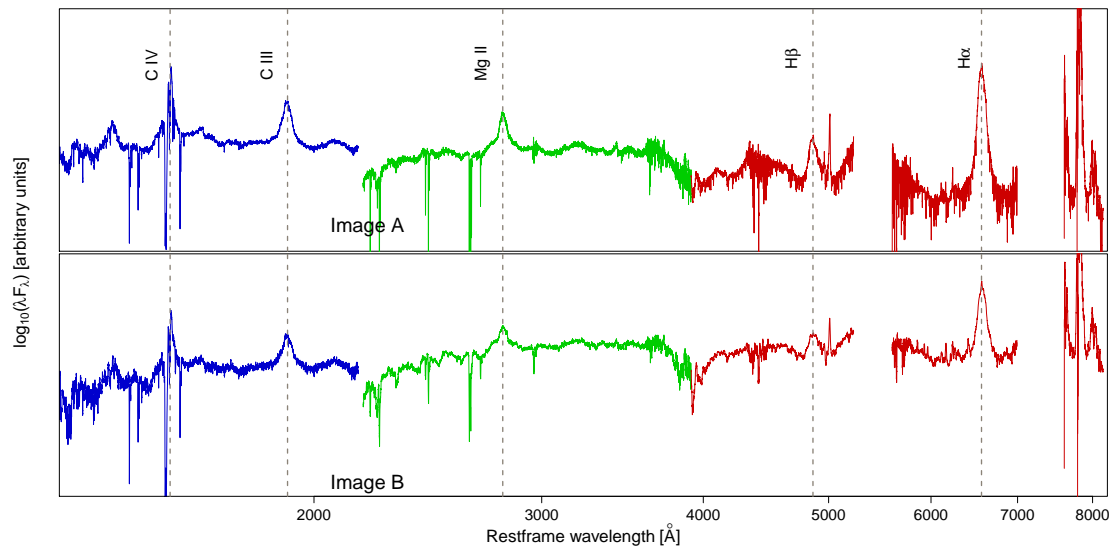


FIGURE B.2: Spectra for image A and B of LBQS1333+0113. The images are corrected by their respective redshift ( $z_s = 1.57$  and  $z_l = 0.44$ ).

# Appendix C

## Probability density functions

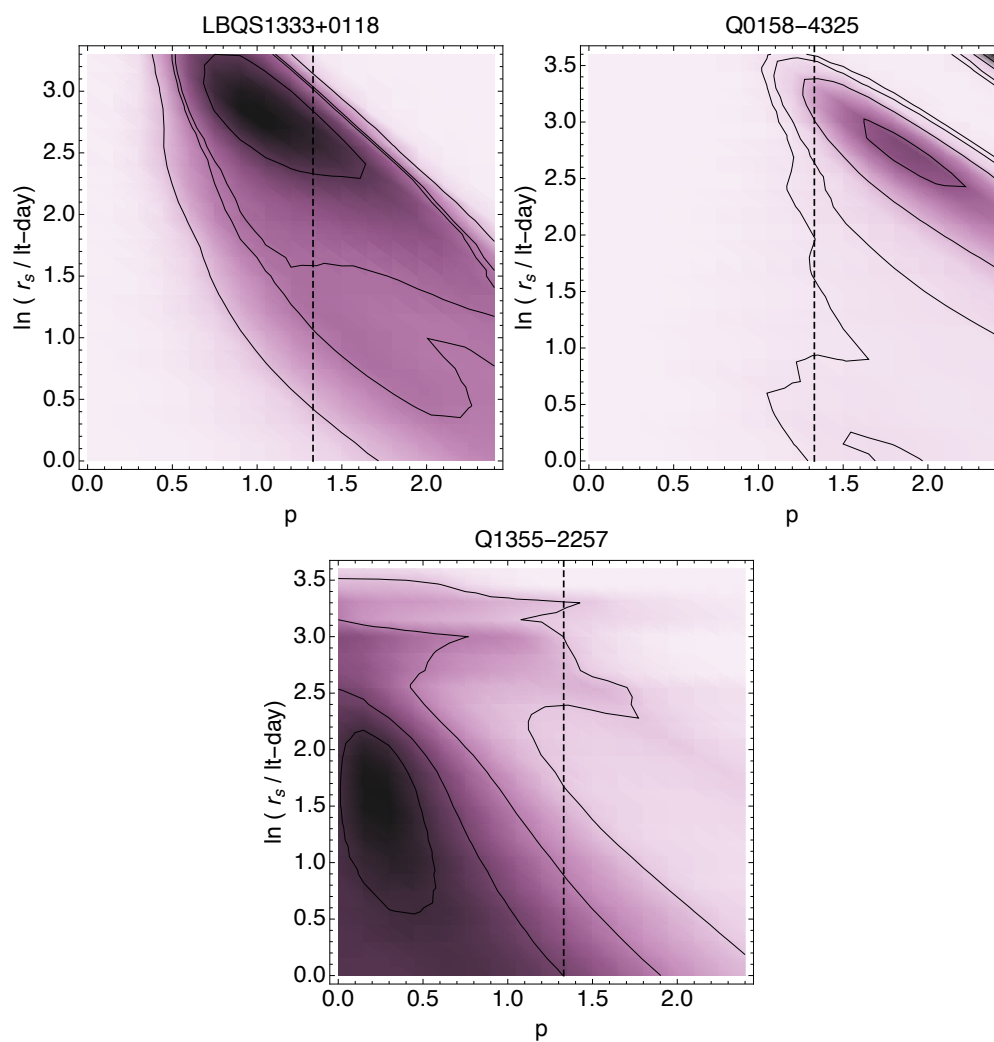


FIGURE C.1: Probability density function for the three systems. The contours of probability are  $0.5\sigma$ ,  $1.0\sigma$ ,  $1.5\sigma$  and  $2.0\sigma$  steps.

# List of Figures

1.1	Composite quasar spectrum from <a href="#">Vanden Berk et al. 2001</a> . It shows the characteristic broad and narrow emission lines of quasars. . . . .	3
1.2	Scheme of an AGN adapted from <a href="#">Urry &amp; Padovani 1995</a> . . . . .	4
1.3	Representations of the reverberation mapping. Upper left: Scheme based on the AGN model of <a href="#">Urry &amp; Padovani 1995</a> . The accretion disk emits the continuum radiation and the response in the BLR shown as emission lines. Upper right: The accretion disk is in red and the BLR is in blue. The figure shows the time delay between light which reaches us directly from the central continuum source (the red arrow) and the light which is emitted due to recombination in the BLR (the blue arrow). Lower image: Continuum and emission-line light curves for Mrk 335 from <a href="#">Peterson 2001</a> . . . . .	6
1.4	$M_{BH}$ correlation with host galaxy parameters. Left: $M_{BH}$ vs mass of the bulge from <a href="#">Kormendy &amp; Ho 2013</a> . The authors distinguish classical bulges, but they are indistinguishable from elliptical galaxies, except that they are embedded in disks ( <a href="#">Renzini 1999</a> ). Right: $M_{BH}$ vs velocity dispersion from <a href="#">Tremaine et al. 2002</a> . . . . .	8
1.5	Gravitational lensing examples. Left: Double lensed quasar QJ0158-4325 in filter i from CASTLES. Right: Modified scheme of a gravitational lensing configuration taken from <a href="#">Schneider 2006</a> . . . . .	11
1.6	Distortion of a solid angle subtended by a source from <a href="#">Schneider 2006</a> . . . . .	15
1.7	Figure from <a href="#">Narayan &amp; Bartelmann 1996</a> showing the effect that the convergence and shear have in a circular source. . . . .	16
1.8	<i>Critical</i> (left) and <i>caustic</i> (right) curves for an elliptical lens. The numbers represent the regions in the source plane that correspond to 1, 3 or 5 images, respectively (Image from <a href="#">Wambsganss 1998</a> ). . . . .	17
1.9	Strong lensing configuration for different alignments between a source and an elliptical lens. Image shows two configurations The different colors represent the source images and its respective images formed. Image from <a href="#">Zalesky &amp; Ebeling 2020</a> , credits from <a href="#">Narayan &amp; Bartelmann 1996</a> . . . . .	17
1.10	Light curves for DESJ0408-5354 presented in <a href="#">Courbin et al. 2018</a> . The variability is observed in image A and B. . . . .	19
1.11	Microlensing effect due to gravitational lensing by individual stars. The image show the macromodel that split into microimages. Figure from <a href="#">Refsdal &amp; Surdej 1994</a> . . . . .	20
1.12	R-L relation for $H\beta$ from <a href="#">Peterson 2010</a> . The luminosity is at $\lambda = 5100 \text{ \AA}$ and the BLR radius in light days. . . . .	23

1.13	CIV BEL widths showing: (Right) the blue asymmetries (blueshifts) with the line centroid displaced to the blue, which are a clear signal of outflows originating in disc winds (Coatman et al. 2016) and (left) the presence of microlensing or variability in the wing (Figure adapted from Fian et al. 2018)	23
1.14	BH mass and luminosity plane from Shen et al. 2019. The blue contours are for the SDSS-DR7 quasars and the red point the SDSS-RM sample. They use the single-epoch $M_{BH}$ .	24
2.1	Two-dimensional spectra for WGD2038-4008. <i>Left</i> : Collapsed frame along the wavelength axis after the subtraction of the sky median. The pink shaded zone represent the sky region (see text). <i>Right</i> : NIR frame after sky subtraction.	36
2.2	Final 2D NIR spectrum for WGD2038-4008 using the PCA sky extraction described in Sect. ?? (top) compared to the one using ESO pipeline reduction (bottom). Both spectra are flux calibrated and telluric corrected.	38
2.3	Gaussian fit (red line) in the collapsed 2D reduced spectrum along the wavelength axis (grey line) of the system Q1355-2257 in the NIR arm. The dashed blue line represents the two Gaussian functions for the two images of the system. No lensing galaxy is present in this case.	39
2.4	One pixel of the reduced 2D spectrum of the the Gaussian fitting in WGD2038-4008 (upper image), along with its probability function (bottom image).	40
2.5	Example of flux loss in a Gaussian Function of $\sigma = 1.6$ pixels. The red lines is the NIR slit width and in blue the flux loss due to this sigma.	41
2.6	Spectra of the three lensed quasars observed with LUCIFER instrument.	42
2.7	Spectra of the seven lensed quasars observed with MMIRS instrument.	43
3.1	rest frame wavelength vs flux SED for the system Q1017-207. The lines represent the contribution of the AGN (blue), elliptical galaxy (red) and irregular galaxy (cyan). The best fitting combination is represented by the black line.	50
3.2	Microlensing magnification maps for component A of Q1355-2257 with a size of $1000 \times 1000$ pix <sup>2</sup> . The $\kappa$ and $\gamma$ parameters for image A are 0.31 and 0.28 respectively (Sluse et al. 2012).	54
4.1	Two images of WGD2038-4008 using different telescopes. Left: DES image in filter gri from Agnello et al. 2018. Right: Image obtained from Shajib et al. 2019, which is a combination of three HST bands: F160W, F814W, and F475X.	56
4.2	MgII, H $\beta$ , and H $\alpha$ emission line region. The images are demagnified using the magnification values from the lens model.	57
4.3	Gaussian fitting of H $\alpha$ , H $\beta$ , and MgII regions for images A (left) and B (right). The red line represents the best fit, the black lines represent the different components of each region (emission and absorption), the green line represents the Fe template, and the blue line is the continuum fit to the spectra. The $1\sigma$ error of the spectra along with the residuals and their respective errors are at the bottom of the images.	58

---

4.4	Magnitude difference $m_A - m_B$ vs wavelength ( $\lambda_0$ ) between images A and B. The red squares show the integrated continuum and the black circles the emission line core without the continuum using X-shooter. Shown are the measurements obtained from the literature: HST <a href="#">Shajib et al. 2019</a> (magenta triangles), VISTA <a href="#">Lee 2019</a> (cyan diamonds), DES <a href="#">Agnello et al. 2018</a> (blue diamonds) and HST F105W/G102 <a href="#">Nierenberg et al. 2020</a> (orange square for continuum and orange triangle for a narrow emission line). The red line is the median of the continuum, the dotted red line the standard deviation, the black line the emission line core, and the blue line the literature. . . . .	59
4.5	$M_{BH}$ vs $L_{bol}$ for quasars. The masses plotted are estimated from different emission lines and monochromatic luminosity found to date ( <a href="#">Peng et al. 2006b</a> , <a href="#">Assef et al. 2011</a> , <a href="#">Sluse et al. 2012</a> , <a href="#">Ding et al. 2017a</a> ). For lensed quasars, black open diamonds correspond to the $M_{BH}$ derived from the MgII and CIV emission lines, black open triangle correspond to the $H\alpha$ emission line, and black filled triangles to the $H\beta$ emission line. For non-lensed quasars, <a href="#">Shen et al. 2019</a> data for $M_{BH}$ from SDSS are represented by the gray dots and gray contours. The average $M_{BH}$ mass estimation for WG2038-4008 is represented as blue, red, and green triangles for MgII, $H\beta$ , and $H\alpha$ emission lines. . . . .	62
4.6	HST images in filter F160W for the 11 lensed quasars. The images are obtained from CASTLES webpage in filter F160W. . . . .	67
4.7	Gaussian fitting of $H\alpha$ and $H\beta$ emission lines for the lensed quasars. The red line represents the best fit, the black lines represent the different components of each region, the green line represents the Fe template, and the blue line is the continuum fit to the spectra. The $1\sigma$ error of the spectra along with the residuals and their respective errors are at the bottom of the plots. . . . .	68
4.8	Mass-luminosity relation for AGNs. The masses are estimated from different emission lines and the monochromatic luminosity found to date for lensed quasars ( <a href="#">Peng et al. 2006b</a> , <a href="#">Greene et al. 2010</a> , <a href="#">Assef et al. 2011</a> , <a href="#">Sluse et al. 2012</a> ) is compared to those obtained for non-lensed quasar from <a href="#">Shen et al. 2019</a> . For lensed quasars, gray open diamonds correspond to the $M_{BH}$ derived from the MgII, gray circles from CIV emission lines, black open triangles correspond to the $H\alpha$ emission line, and black filled circles to the $H\beta$ emission line. For non-lensed quasars, <a href="#">Shen et al. 2019</a> data for $M_{BH}$ from SDSS are represented by the gray dots and gray contours. The orange open triangles are our new $M_{BH}$ estimation of lensed AGNs. We red open triangle, blue open diamond and green circle are the WGD2038-4008 values from <a href="#">Melo et al. 2021</a>	71
4.9	Images of the system LBQS1333+0113. Left: HST images in filter F160W obtained from CASTLES. Right: Original Subaru Suprime-Cam image in the $i$ -band from <a href="#">Oguri et al. 2004</a> taken in 2003. . . . .	75
4.10	Part of the UVB spectra of the system LBQS1333+0113 showing absorption features in CIV. . . . .	76
4.11	CIV, CIII, MgII $H\beta$ and $H\alpha$ emission line profiles for LBQS1333+0113. The images are demagnified using the magnification values $\mu_A = 3.77$ and $\mu_B = 0.87$ obtained from <a href="#">Sluse et al. 2012</a> . Notice that $H\alpha$ and MgII shows profile difference between both images. . . . .	77
4.12	$H\alpha$ profile comparison between the ESO phase 3 and my reduction and extraction of image A and B. The distortion observed in the peak is due to a poor telluric correction. . . . .	78

---

- 4.13 Images of the system Q1355-2257. Left: HST images in filter F160W obtained from CASTLES. Right: Image of three exposures taken with HST STIS from [Morgan et al. 2003](#) . . . . . 78
- 4.14 CIV, CIII, MgII  $H\beta$  and  $H\alpha$  emission line profiles for Q1355-2257. . . . . 79
- 4.15 HST image of QJ0158-4325 in filter F160W obtained from CASTLES. . . . . 80
- 4.16 CIV, CIII, MgII  $H\beta$  and  $H\alpha$  emission line profiles for QJ0158-4325. The images are demagnified using the magnification values  $\mu_A = 25.27$  and  $\mu_B = 12.31$  obtained from [Bhatiani et al. 2019](#). . . . . 80
- 4.17 Magnitude difference  $m_B - m_A$  vs  $\lambda_0$  between images A and B of LBQS1333+0113. Red squares shows the integrated continuum and the black circles the emission line core without the continuum. We include measurements obtained from [Oguri et al. 2004](#): Subaru 8.2-m telescope in i band (orange diamond), Sloan Digital Sky Survey (SDSS) in u, g, r i z bands (magenta diamonds) and Keck telescope in K band (cyan diamond). We included one value from the Hubble Space Telescope (HST) in the H band (obtained from CASTLES). The red line is the best fit for the continuum and the dashed red line the standard deviation, the black line is the median for the emission line core and the blue line for the literature. . . . . 81
- 4.18 Magnitude difference  $m_B - m_A$  vs wavelength at restframe  $\lambda_0$  between images A and B of Q1355-2257. Red squares shows the integrated continuum and the black circles the emission line core without the continuum. We include measurements obtained from the literature: HST<sup>1</sup>in filters F160W, F555W and F814W (blue diamonds); g, r, i, and z filters of the Sloan digital Sky Survey (SDSS) from [Morgan et al. 2003](#) (cyan diamonds); spectroscopic data from [Sluse et al. 2012](#) (purple square and circle for the continuum and emission line, respectively) and spectroscopic data from [Rojas et al. 2020](#) of the VLT/FORS2 (orange square and circle for the continuum and emission line, respectively). The red and black line is the fit of the continuum and emission line core, and the red and black shaded area the standard deviation, respectively. The grey dashed line is the fitting for the core of the emission line and in orange dashed line for the continuum presented in [Rojas et al. 2020](#) along with their errors as the shaded area. . . . . 83
- 4.19 Magnitude difference  $m_B - m_A$  vs  $\lambda_0$  between images A and B of QJ0158-4325. Red squares shows the integrated continuum and the black circles the emission line core. I included measurements obtained from the literature: HST ([Morgan et al. 2003](#)/CASTLES; blue diamonds), hard X-ray (cyan diamond) and soft X-ray data (magenta diamond) from CHANDRA telescope ([Chen et al. 2012](#)), VLT/FORS2 from [Faure et al. 2009](#) (green diamond) and Las Campanas Observatory (LCO) from [Morgan et al. 1999](#) (orange diamond). The Red line is the fit of the continuum and the shaded red area the standard deviation, the black line is the median for the emission line core and the blue line for the HST data. . . . . 84
- 4.20 Gaussian fitting of the broad emission lines for LBQS1333+0113 of images A and B. Red line is the best fit, black lines is the different components of each region, green line represents the Fe template and the blue line is the continuum fit of the spectra. In the bottom of the images is the 1-sigma error of the spectra along with the residuals. . . . . 87
-

4.21	Gaussian fitting of the broad emission lines for QJ0158-4325 of images A (left) and B (right). Red line is the best fit, black lines is the different components of each region, green line represents the Fe template and the blue line is the continuum fit of the spectra. In the bottom of the images is the 1-sigma error of the spectra along with the residuals. . . . .	88
4.22	Gaussian fitting of the broad emission lines for Q1355-2257 of images A and B. Red line is the best fit, black lines is the different components of each region, green line represents the Fe template and the blue line is the continuum fit of the spectra. In the bottom of the images is the 1-sigma error of the spectra along with the residuals. . . . .	89
4.23	$M_{BH}$ vs $L_{bol}$ for quasars. Masses of lensed quasars are plotted from different emission lines and luminosities that exists upto date (Peng et al. 2006b, Assef et al. 2011, Sluse et al. 2012, Ding et al. 2017a). The new measurements of the four lensed systems using X-shooter are presented in different colors. . . . .	90
4.24	$M_{BH}$ vs $L_{bol}$ for quasars. The gray fit is the $H\alpha$ and $H\beta$ values that exists in the literature up to date (Peng et al. 2006b, Assef et al. 2011, Sluse et al. 2012, Ding et al. 2017a), while the purple fit adding our new Balmer estimates from the four double quasars are plotted from different emission lines and luminosities. The new measurements of the four lensed systems using X-shooter are presented in different colors. . . . .	91
4.25	Combined probability function for the three systems. The accretion disk size and temperature profile from Jiménez-Vicente et al. 2014 is also plotted. . . . .	93
B.1	Spectra for image A, image B, and the lensing galaxy of WGD2038-4008. The images are corrected by their respective redshifts ( $z_s = 0.777$ and $z_l = 0.230$ ). The lensing galaxy is uncontaminated by the quasar emission. . . . .	99
B.2	Spectra for image A and B of LBQS1333+0113. The images are corrected by their respective redshift ( $z_s = 1.57$ and $z_l = 0.44$ ). . . . .	100
C.1	Probability density function for the three systems. The contours of probability are $0.5\sigma$ , $1.0\sigma$ , $1.5\sigma$ and $2.0\sigma$ steps. . . . .	101

---

# List of Tables

2.1	Sample of gravitational lensed quasars following the selection process described in section 2.1. The redshift, separation and magnitude information is obtained from CASTLES webpage and/or GLQ database. The measured $M_{BH}$ from the literature is shown along with the emission line used, luminosity, FWHM and reference. . . . .	28
2.1	<b>Table 2.1 Continued:</b> . . . . .	29
2.1	<b>Table 2.1 Continued:</b> . . . . .	30
2.1	<b>Table 2.1 Continued:</b> . . . . .	31
2.1	<b>Table 2.1 Continued:</b> . . . . .	32
2.1	<b>Table 2.1 Continued:</b> . . . . .	33
2.2	Summary of X-shooter observations for proposals 103.B–0566(A) and 106.21DC.001.	35
2.3	Best fit for the standard deviation parameter used in each system for the extraction of the images and lensing galaxy (if it is present). . . . .	39
2.4	Estimated percentage of the flux loss for the systems in each arm. . . . .	40
2.5	Observations of LUCIFER and MMIRS data. . . . .	43
3.1	Magnification values used for demagnifying the luminosity of each image. Errors are added if it exists in the lens model. . . . .	46
4.1	FWHM, luminosities, and $M_{BH}$ . . . . .	57
4.2	$H\alpha$ and $H\beta$ BH mass estimates of lensed quasars. . . . .	70
4.3	Magnitude difference of LBQS1333+0113. . . . .	83
4.4	Magnitude difference for Q1355-2257. . . . .	84
4.5	Magnitude difference of QJ0158-4325. . . . .	85
4.6	FWHM, luminosities, and $M_{BH}$ for the systems. . . . .	90
4.7	Chromatic microlensing $\Delta m$ for three different wavelengths for each system. . .	92
4.8	$p$ and the accretion disk size from the model and from equation 3.6. . . . .	92
A.1	Line regions and adopted constraints used for the line profile fitting. Table adapted from <a href="#">Mejía-Restrepo et al. 2016</a> (Also seen in Table 4 of <a href="#">Shang et al. 2007</a> ). . . . .	98

# Bibliography

- Abajas, C., Mediavilla, E., Muñoz, J. A., Gómez-Álvarez, P., & Gil-Merino, R. 2007, *ApJ*, 658, 748
- Abajas, C., Mediavilla, E., Muñoz, J. A., Popović, L. Č., & Oscoz, A. 2002, *ApJ*, 576, 640
- Abbott, T. M. C., Agüena, M., Alarcon, A., et al. 2022, *Phys. Rev. D*, 105, 023520
- Agnello, A., Lin, H., Kuropatkin, N., et al. 2018, *MNRAS*, 479, 4345
- Agnello, A., Treu, T., Ostrovski, F., et al. 2015, *MNRAS*, 454, 1260
- Aird, J., Coil, A. L., Georgakakis, A., et al. 2015, *MNRAS*, 451, 1892
- Anguita, T., Schechter, P. L., Kuropatkin, N., et al. 2018, *MNRAS*, 480, 5017
- Antonucci, R. 1993, *ARA&A*, 31, 473
- Antonucci, R. R. J. & Miller, J. S. 1985, *ApJ*, 297, 621
- Arévalo, P., Uttley, P., Lira, P., et al. 2009, *MNRAS*, 397, 2004
- Assef, R. J., Denney, K. D., Kochanek, C. S., et al. 2011, *ApJ*, 742, 93
- Assef, R. J., Kochanek, C. S., Brodwin, M., et al. 2010, *ApJ*, 713, 970
- Baade, W. & Minkowski, R. 1954, *ApJ*, 119, 206
- Baldwin, J. A., Phillips, M. M., & Terlevich, R. 1981, *PASP*, 93, 5
- Bartelmann, M. 2010, *Classical and Quantum Gravity*, 27, 233001
- Barth, A. J., Bennert, V. N., Canalizo, G., et al. 2015, *ApJS*, 217, 26
- Baskin, A. & Laor, A. 2005, *MNRAS*, 356, 1029

- Bate, N. F., Floyd, D. J. E., Webster, R. L., & Wyithe, J. S. B. 2008, *MNRAS*, 391, 1955
- Bate, N. F., Vernardos, G., O'Dowd, M. J., et al. 2018, *MNRAS*, 479, 4796
- Batiste, M., Bentz, M. C., Raimundo, S. I., Vestergaard, M., & Onken, C. A. 2017, *ApJ*, 838, L10
- Begelman, M. C. & Rees, M. J. 1978, *MNRAS*, 185, 847
- Bennert, V. N., Auger, M. W., Treu, T., Woo, J.-H., & Malkan, M. A. 2011, *ApJ*, 742, 107
- Bennert, V. N., Treu, T., Auger, M. W., et al. 2015, *ApJ*, 809, 20
- Bentz, M. C., Denney, K. D., Grier, C. J., et al. 2013, *ApJ*, 767, 149
- Bentz, M. C., Peterson, B. M., Netzer, H., Pogge, R. W., & Vestergaard, M. 2009, *ApJ*, 697, 160
- Bentz, M. C., Peterson, B. M., Pogge, R. W., Vestergaard, M., & Onken, C. A. 2006, *ApJ*, 644, 133
- Bhatiani, S., Dai, X., & Guerras, E. 2019, *ApJ*, 885, 77
- Birrer, S. & Amara, A. 2018, *Physics of the Dark Universe*, 22, 189
- Birrer, S., Shajib, A., Gilman, D., et al. 2021, *The Journal of Open Source Software*, 6, 3283
- Birrer, S. & Treu, T. 2021, *A&A*, 649, A61
- Birrer, S., Treu, T., Rusu, C. E., et al. 2019, *MNRAS*, 484, 4726
- Blackburne, J. A., Pooley, D., Rappaport, S., & Schechter, P. L. 2011, *ApJ*, 729, 34
- Blandford, R. D. & McKee, C. F. 1982, *ApJ*, 255, 419
- Blandford, R. D. & Rees, M. J. 1992, in *American Institute of Physics Conference Series*, Vol. 254, *Testing the AGN paradigm*, ed. S. S. Holt, S. G. Neff, & C. M. Urry, 3–19
- Bogdanov, M. B. & Cherepashchuk, A. M. 2004, *Astronomy Reports*, 48, 261
- Bolton, J. G. & Stanley, G. J. 1948, *Nature*, 161, 312
- Bongiorno, A., Maiolino, R., Brusa, M., et al. 2014, *MNRAS*, 443, 2077
- Bonvin, V., Courbin, F., Suyu, S. H., et al. 2017, *MNRAS*, 465, 4914
-

- Bonvin, V., Millon, M., Chan, J. H. H., et al. 2019, *A&A*, 629, A97
- Bower, R. G., Benson, A. J., Malbon, R., et al. 2006, *MNRAS*, 370, 645
- Braibant, L., Hutsemékers, D., Sluse, D., & Anguita, T. 2016, *A&A*, 592, A23
- Braibant, L., Hutsemékers, D., Sluse, D., Anguita, T., & García-Vergara, C. J. 2014, *A&A*, 565, L11
- Buckley-Geer, E. J., Lin, H., Rusu, C. E., et al. 2020, *MNRAS*, 498, 3241
- Bujarrabal, V., Guibert, J., & Balkowski, C. 1981, *A&A*, 104, 1
- Calderone, G., Ghisellini, G., Colpi, M., & Dotti, M. 2013, *MNRAS*, 431, 210
- Campitiello, S., Celotti, A., Ghisellini, G., & Sbarrato, T. 2019, *A&A*, 625, A23
- Campitiello, S., Celotti, A., Ghisellini, G., & Sbarrato, T. 2020, *A&A*, 640, A39
- Carroll, B. W. & Ostlie, D. A. 2006, *An introduction to modern astrophysics and cosmology*
- Chan, J. H. H., Rojas, K., Millon, M., et al. 2021, *A&A*, 647, A115
- Chang, K. & Refsdal, S. 1979, *Nature*, 282, 561
- Chartas, G., Agol, E., Eracleous, M., et al. 2002, *ApJ*, 568, 509
- Chartas, G., Eracleous, M., Agol, E., & Gallagher, S. C. 2004, *ApJ*, 606, 78
- Chartas, G., Kochanek, C. S., Dai, X., et al. 2012, *ApJ*, 757, 137
- Chartas, G., Krawczynski, H., Zalesky, L., et al. 2017, *ApJ*, 837, 26
- Chen, B., Dai, X., Kochanek, C. S., et al. 2012, *ApJ*, 755, 24
- Chen, G. C. F., Fassnacht, C. D., Suyu, S. H., et al. 2019, *MNRAS*, 490, 1743
- Chilingarian, I., Beletsky, Y., Moran, S., et al. 2015, *PASP*, 127, 406
- Cicone, C., Brusa, M., Ramos Almeida, C., et al. 2018, *Nature Astronomy*, 2, 176
- Claeskens, J.-F. & Surdej, J. 2002, *A&A Rev.*, 10, 263
- Coatman, L., Hewett, P. C., Banerji, M., & Richards, G. T. 2016, *MNRAS*, 461, 647
- Coatman, L., Hewett, P. C., Banerji, M., et al. 2017, *MNRAS*, 465, 2120
-

- Colbert, E. J. M. & Mushotzky, R. F. 1999, *ApJ*, 519, 89
- Collin, S., Boisson, C., Mouchet, M., et al. 2002, *A&A*, 388, 771
- Cornachione, M. A., Morgan, C. W., Millon, M., et al. 2020, *ApJ*, 895, 125
- Courbin, F., Bonvin, V., Buckley-Geer, E., et al. 2018, *A&A*, 609, A71
- Courbin, F., Chantry, V., Revaz, Y., et al. 2011, *A&A*, 536, A53
- Courbin, F., Saha, P., & Schechter, P. L. 2002, in *Gravitational Lensing: An Astrophysical Tool*, ed. F. Courbin & D. Minniti, Vol. 608, 1
- Croton, D. J., Springel, V., White, S. D. M., et al. 2006, *MNRAS*, 365, 11
- Dai, X., Chartas, G., Agol, E., Bautz, M. W., & Garmire, G. P. 2003, *ApJ*, 589, 100
- Dai, X., Chartas, G., Eracleous, M., & Garmire, G. P. 2004, *ApJ*, 605, 45
- Dai, X., Kochanek, C. S., Chartas, G., et al. 2010, *ApJ*, 709, 278
- Dark Energy Survey Collaboration, Abbott, T., Abdalla, F. B., et al. 2016, *MNRAS*, 460, 1270
- Davies, R., Baron, D., Shimizu, T., et al. 2020, *MNRAS*, 498, 4150
- Davies, R. I., Thomas, J., Genzel, R., et al. 2006, *ApJ*, 646, 754
- Deeming, T. J. 1964, *MNRAS*, 127, 493
- DeGraf, C., Di Matteo, T., Treu, T., et al. 2015, *MNRAS*, 454, 913
- Denney, K. D. 2012, *ApJ*, 759, 44
- Di Matteo, T., Springel, V., & Hernquist, L. 2005, *Nature*, 433, 604
- Ding, X., Liao, K., Treu, T., et al. 2017a, *MNRAS*, 465, 4634
- Ding, X., Treu, T., Birrer, S., et al. 2021, *MNRAS*, 501, 269
- Ding, X., Treu, T., Suyu, S. H., et al. 2017b, *MNRAS*, 472, 90
- D’Odorico, S. 1990, *The Messenger*, 61, 51
- Donnarumma, I., De Rosa, A., Vittorini, V., et al. 2011, *ApJ*, 736, L30
-

- Du, P., Lu, K.-X., Hu, C., et al. 2016, *ApJ*, 820, 27
- Dyson, F. W., Eddington, A. S., & Davidson, C. 1920, *Philosophical Transactions of the Royal Society of London Series A*, 220, 291
- Eddington, A. S. 1919, *The Observatory*, 42, 119
- Edelson, R., Gelbord, J., Cackett, E., et al. 2019, *ApJ*, 870, 123
- Edelson, R., Gelbord, J. M., Horne, K., et al. 2015, *ApJ*, 806, 129
- Eigenbrod, A. 2011, *Gravitational Lensing of Quasars*
- Eigenbrod, A., Courbin, F., Meylan, G., Vuissoz, C., & Magain, P. 2006, *A&A*, 451, 759
- Eigenbrod, A., Courbin, F., Vuissoz, C., et al. 2005, *A&A*, 436, 25
- Einstein, A. 1905, *Annalen der Physik*, 322, 891
- Einstein, A. 1916, *Annalen der Physik*, 354, 769
- Eulaers, E., Tewes, M., Magain, P., et al. 2013, *A&A*, 553, A121
- Event Horizon Telescope Collaboration, Akiyama, K., Alberdi, A., et al. 2019, *ApJ*, 875, L1
- Fabbiano, G. 2006, *ARA&A*, 44, 323
- Fabian, A. C. 1999, *MNRAS*, 308, L39
- Falco, E. E., Impey, C. D., Kochanek, C. S., et al. 1999, *ApJ*, 523, 617
- Falco, E. E., Kochanek, C. S., Lehár, J., et al. 2001, *Astronomical Society of the Pacific Conference Series*, Vol. 237, *The CASTLES Gravitational Lensing Tool*, ed. T. G. Brainerd & C. S. Kochanek, 25
- Falco, E. E., Shapiro, I. I., Moustakas, L. A., & Davis, M. 1997, *ApJ*, 484, 70
- Fanaroff, B. L. & Riley, J. M. 1974, *MNRAS*, 167, 31P
- Fassnacht, C. D., Blandford, R. D., Cohen, J. G., et al. 1999, *AJ*, 117, 658
- Fassnacht, C. D., Xanthopoulos, E., Koopmans, L. V. E., & Rusin, D. 2002, *ApJ*, 581, 823
- Fath, E. A. 1909, *Lick Observatory Bulletin*, 149, 71
- Faure, C., Anguita, T., Eigenbrod, A., et al. 2009, *A&A*, 496, 361
-

- 
- Fausnaugh, M. M., Grier, C. J., Bentz, M. C., et al. 2017, *ApJ*, 840, 97
- Ferrarese, L. & Ford, H. 2005, *Space Sci. Rev.*, 116, 523
- Ferrarese, L. & Merritt, D. 2000, *ApJ*, 539, L9
- Ferrarese, L., Pogge, R. W., Peterson, B. M., et al. 2001, *ApJ*, 555, L79
- Fian, C., Guerras, E., Mediavilla, E., et al. 2018, *ApJ*, 859, 50
- Fian, C., Mediavilla, E., Hanslmeier, A., et al. 2016, *ApJ*, 830, 149
- Fian, C., Mediavilla, E., Motta, V., et al. 2021, *A&A*, 653, A109
- Fine, S., Croom, S. M., Bland-Hawthorn, J., et al. 2010, *MNRAS*, 409, 591
- Francis, P. J. & Wills, B. J. 1999, in *Astronomical Society of the Pacific Conference Series*, Vol. 162, *Quasars and Cosmology*, ed. G. Ferland & J. Baldwin, 363
- Freudling, W., Romaniello, M., Bramich, D. M., et al. 2013, *A&A*, 559, A96
- Frittelli, S., Kling, T. P., & Newman, E. T. 2002, *Phys. Rev. D*, 65, 123007
- Gaia Collaboration, Prusti, T., de Bruijne, J. H. J., et al. 2016, *A&A*, 595, A1
- Gebhardt, K., Bender, R., Bower, G., et al. 2000, *ApJ*, 539, L13
- Ghisellini, G., Della Ceca, R., Volonteri, M., et al. 2010, *MNRAS*, 405, 387
- Glikman, E., Helfand, D. J., & White, R. L. 2006, *ApJ*, 640, 579
- Goad, M. R., Korista, K. T., & Ruff, A. J. 2012, *MNRAS*, 426, 3086
- Graham, A. W. 2007, *MNRAS*, 379, 711
- Greene, J. E. & Ho, L. C. 2005, *ApJ*, 630, 122
- Greene, J. E., Peng, C. Y., & Ludwig, R. R. 2010, *ApJ*, 709, 937
- Grier, C. J., Martini, P., Watson, L. C., et al. 2013, *ApJ*, 773, 90
- Grier, C. J., Shen, Y., Horne, K., et al. 2019, *ApJ*, 887, 38
- Grier, C. J., Trump, J. R., Shen, Y., et al. 2017, *ApJ*, 851, 21
- Guerras, E., Dai, X., & Mediavilla, E. 2020, *ApJ*, 896, 111
-

- Guerras, E., Dai, X., Steele, S., et al. 2017, *ApJ*, 836, 206
- Guerras, E., Mediavilla, E., Jimenez-Vicente, J., et al. 2013, *ApJ*, 764, 160
- Gültekin, K., Richstone, D. O., Gebhardt, K., et al. 2009, *ApJ*, 698, 198
- Haardt, F. & Maraschi, L. 1991, *ApJ*, 380, L51
- Haehnelt, M. G., Natarajan, P., & Rees, M. J. 1998, *MNRAS*, 300, 817
- Hainline, L. J., Morgan, C. W., MacLeod, C. L., et al. 2013, *ApJ*, 774, 69
- Hall, P. B., Hutsemékers, D., Anderson, S. F., et al. 2003, *ApJ*, 593, 189
- Hamann, F., Herbst, H., Paris, I., & Capellupo, D. 2019, *MNRAS*, 483, 1808
- Hanbury Brown, R., Jennison, R. C., & Gupta, M. K. D. 1952, *Nature*, 170, 1061
- Häring, N. & Rix, H.-W. 2004, *ApJ*, 604, L89
- Hewitt, J. N., Turner, E. L., Schneider, D. P., Burke, B. F., & Langston, G. I. 1988, *Nature*, 333, 537
- Hicks, E. K. S. & Malkan, M. A. 2008, *ApJS*, 174, 31
- Ho, L. C. 1999, *ApJ*, 516, 672
- Ho, L. C. 2008, *ARA&A*, 46, 475
- Hogg, D. W. 1999, arXiv e-prints [[arXiv]astro-ph/9905116]
- Hoormann, J. K., Martini, P., Davis, T. M., et al. 2019, *MNRAS*, 487, 3650
- Hopkins, P. F. & Hernquist, L. 2009, *ApJ*, 698, 1550
- Hopkins, P. F., Hernquist, L., Cox, T. J., & Kereš, D. 2008, *ApJS*, 175, 356
- Hopkins, P. F., Richards, G. T., & Hernquist, L. 2007, *ApJ*, 654, 731
- Hutsemékers, D. & Sluse, D. 2021, *A&A*, 654, A155
- Hutsemékers, D., Sluse, D., & Kumar, P. 2020, *A&A*, 633, A101
- Hutsemekers, D., Surdej, J., & van Drom, E. 1994, *Ap&SS*, 216, 361
- Inada, N., Oguri, M., Becker, R. H., et al. 2006, *AJ*, 131, 1934
-

- Inada, N., Oguri, M., Rusu, C. E., Kayo, I., & Morokuma, T. 2014, *AJ*, 147, 153
- Inada, N., Oguri, M., Shin, M.-S., et al. 2009, *AJ*, 137, 4118
- Irwin, M. J., Webster, R. L., Hewett, P. C., Corrigan, R. T., & Jedrzejewski, R. I. 1989, *AJ*, 98, 1989
- Jackson, N. 2008, *MNRAS*, 389, 1311
- Jiménez-Vicente, J. & Mediavilla, E. 2019, *ApJ*, 885, 75
- Jiménez-Vicente, J., Mediavilla, E., Kochanek, C. S., & Muñoz, J. A. 2015, *ApJ*, 799, 149
- Jiménez-Vicente, J., Mediavilla, E., Kochanek, C. S., et al. 2014, *ApJ*, 783, 47
- Kaspi, S., Brandt, W. N., Maoz, D., et al. 2007, *ApJ*, 659, 997
- Kaspi, S., Brandt, W. N., Maoz, D., et al. 2021, *ApJ*, 915, 129
- Kaspi, S., Maoz, D., Netzer, H., et al. 2005, *ApJ*, 629, 61
- Kaspi, S., Smith, P. S., Netzer, H., et al. 2000, *ApJ*, 533, 631
- Kausch, W., Noll, S., Smette, A., et al. 2015, *A&A*, 576, A78
- Kayo, I., Inada, N., Oguri, M., et al. 2010, *AJ*, 139, 1614
- Kayser, R., Refsdal, S., & Stabell, R. 1986, *A&A*, 166, 36
- Keeton, C. R. 2001, arXiv e-prints, astro
- Keeton, C. R., Burles, S., Schechter, P. L., & Wambsganss, J. 2006, *ApJ*, 639, 1
- Keeton, C. R. & Zabludoff, A. I. 2004, *ApJ*, 612, 660
- King, A. 2003, *ApJ*, 596, L27
- King, A. & Pounds, K. 2015, *ARA&A*, 53, 115
- Kochanek, C. S. 2004, *ApJ*, 605, 58
- Kochanek, C. S., Morgan, N. D., Falco, E. E., et al. 2006, *ApJ*, 640, 47
- Kochanek, C. S., Pahre, M. A., Falco, E. E., et al. 2001, *ApJ*, 560, 566
- Kochanek, C. S. & Schechter, P. L. 2004, in *Measuring and Modeling the Universe*, ed. W. L. Freedman, 117
-

- Koopmans, L. V. E., Garrett, M. A., Blandford, R. D., et al. 2002, *MNRAS*, 334, 39
- Kormann, R., Schneider, P., & Bartelmann, M. 1994, *A&A*, 284, 285
- Kormendy, J. & Bender, R. 2009, *ApJ*, 691, L142
- Kormendy, J. & Gebhardt, K. 2001, in *American Institute of Physics Conference Series*, Vol. 586, 20th Texas Symposium on relativistic astrophysics, ed. J. C. Wheeler & H. Martel, 363–381
- Kormendy, J. & Ho, L. C. 2013, *ARA&A*, 51, 511
- Kormendy, J. & Richstone, D. 1995, *ARA&A*, 33, 581
- Krawczynski, H. & Chartas, G. 2017, *ApJ*, 843, 118
- Krone-Martins, A., Graham, M. J., Stern, D., et al. 2019, arXiv e-prints, arXiv:1912.08977
- Laor, A. 1990, *MNRAS*, 246, 369
- Lauer, T. R., Tremaine, S., Richstone, D., & Faber, S. M. 2007, *ApJ*, 670, 249
- Lee, C.-H. 2019, *PASA*, 36, e011
- Lefor, A. T., Futamase, T., & Akhlaghi, M. 2013, *New A Rev.*, 57, 1
- Leighly, K. M. & Moore, J. R. 2004, *ApJ*, 611, 107
- Lemon, C., Auger, M. W., McMahon, R., et al. 2020, *MNRAS*, 494, 3491
- Lemon, C. A., Auger, M. W., & McMahon, R. G. 2019, *MNRAS*, 483, 4242
- Lemon, C. A., Auger, M. W., McMahon, R. G., & Ostrovski, F. 2018, *MNRAS*, 479, 5060
- Lewis, G. F. & Ibata, R. A. 2004, *MNRAS*, 348, 24
- Lira, P., Arévalo, P., Uttley, P., McHardy, I., & Breedt, E. 2011, *MNRAS*, 415, 1290
- Lira, P., Kaspi, S., Netzer, H., et al. 2018, *ApJ*, 865, 56
- Liu, G., Zakamska, N. L., Greene, J. E., Nesvadba, N. P. H., & Liu, X. 2013, *MNRAS*, 436, 2576
- Loeb, A. & Rasio, F. A. 1994, *ApJ*, 432, 52
- Lucey, J. R., Schechter, P. L., Smith, R. J., & Anguita, T. 2018, *MNRAS*, 476, 927
-

- Lynden-Bell, D. 1969, *Nature*, 223, 690
- MacLeod, C. L., Ivezić, Ž., Kochanek, C. S., et al. 2010, *ApJ*, 721, 1014
- Madau, P., Ferguson, H. C., Dickinson, M. E., et al. 1996, *MNRAS*, 283, 1388
- Magorrian, J., Tremaine, S., Richstone, D., et al. 1998, *AJ*, 115, 2285
- Malkan, M. A. 1983, *ApJ*, 268, 582
- Marconi, A., Axon, D. J., Maiolino, R., et al. 2008, *ApJ*, 678, 693
- Marconi, A. & Hunt, L. K. 2003, *ApJ*, 589, L21
- Marziani, P., del Olmo, A., Martínez-Carballo, M. A., et al. 2019, *A&A*, 627, A88
- Marziani, P., Sulentic, J. W., Plauchu-Frayn, I., & del Olmo, A. 2013, *A&A*, 555, A89
- Matsuoka, K., Silverman, J. D., Schramm, M., et al. 2013, *ApJ*, 771, 64
- Matsuoka, Y., Kawara, K., & Oyabu, S. 2008, *ApJ*, 673, 62
- Matthews, K. & Soifer, B. T. 1994, *Experimental Astronomy*, 3, 77
- Matthews, T. A., Morgan, W. W., & Schmidt, M. 1964, *ApJ*, 140, 35
- Matthews, T. A. & Sandage, A. R. 1963, *ApJ*, 138, 30
- Maza, J., Wischnjewsky, M., Antezana, R., & González, L. E. 1995, *Rev. Mexicana Astron. Astrofis.*, 31, 119
- McConnell, N. J. & Ma, C.-P. 2013, *ApJ*, 764, 184
- McGill, K. L., Woo, J.-H., Treu, T., & Malkan, M. A. 2008, *ApJ*, 673, 703
- McHardy, I. M., Connolly, S. D., Peterson, B. M., et al. 2016, *Astronomische Nachrichten*, 337, 500
- McLeod, B., Fabricant, D., Nystrom, G., et al. 2012, *PASP*, 124, 1318
- McLure, R. J. & Dunlop, J. S. 2004, *MNRAS*, 352, 1390
- McLure, R. J. & Jarvis, M. J. 2002, *MNRAS*, 337, 109
- Mediavilla, E., Jiménez-Vicente, J., Fian, C., et al. 2018, *ApJ*, 862, 104
-

- Mediavilla, E., Jiménez-vicente, J., Mejía-restrepo, J., et al. 2019, *ApJ*, 880, 96
- Mediavilla, E., Jiménez-vicente, J., Mejía-restrepo, J., et al. 2020, *ApJ*, 895, 111
- Mediavilla, E., Muñoz, J. A., Falco, E., et al. 2009, *ApJ*, 706, 1451
- Mediavilla, E., Muñoz, J. A., Kochanek, C. S., et al. 2005, *ApJ*, 619, 749
- Mediavilla, E., Muñoz, J. A., Kochanek, C. S., et al. 2011, *ApJ*, 730, 16
- Mediavilla, E., Muñoz, J. A., Lopez, P., et al. 2006, *ApJ*, 653, 942
- Mejía-Restrepo, J. E., Trakhtenbrot, B., Lira, P., & Netzer, H. 2018, *MNRAS*, 478, 1929
- Mejía-Restrepo, J. E., Trakhtenbrot, B., Lira, P., Netzer, H., & Capellupo, D. M. 2016, *MNRAS*, 460, 187
- Melo, A., Motta, V., Godoy, N., et al. 2021, *A&A*, 656, A108
- Millon, M., Courbin, F., Bonvin, V., et al. 2020a, *A&A*, 642, A193
- Millon, M., Courbin, F., Bonvin, V., et al. 2020b, *A&A*, 640, A105
- Minezaki, T., Chiba, M., Kashikawa, N., Inoue, K. T., & Kataza, H. 2009, *ApJ*, 697, 610
- Miyazaki, S., Komiyama, Y., Sekiguchi, M., et al. 2002, *PASJ*, 54, 833
- More, A., Oguri, M., Kayo, I., et al. 2016, *MNRAS*, 456, 1595
- Morgan, C. W., Hainline, L. J., Chen, B., et al. 2012, *ApJ*, 756, 52
- Morgan, C. W., Hyer, G. E., Bonvin, V., et al. 2018, *ApJ*, 869, 106
- Morgan, C. W., Kochanek, C. S., Morgan, N. D., & Falco, E. E. 2010, *ApJ*, 712, 1129
- Morgan, N. D., Dressler, A., Maza, J., Schechter, P. L., & Winn, J. N. 1999, *AJ*, 118, 1444
- Morgan, N. D., Gregg, M. D., Wisotzki, L., et al. 2003, *AJ*, 126, 696
- Mortonson, M. J., Schechter, P. L., & Wambsganss, J. 2005, *ApJ*, 628, 594
- Mosquera, A. M. & Kochanek, C. S. 2011, *ApJ*, 738, 96
- Mosquera, A. M., Kochanek, C. S., Chen, B., et al. 2013, *ApJ*, 769, 53
- Mosquera, A. M., Muñoz, J. A., & Mediavilla, E. 2009, *ApJ*, 691, 1292
-

- Mosquera, A. M., Muñoz, J. A., Mediavilla, E., & Kochanek, C. S. 2011, *ApJ*, 728, 145
- Motta, V., Mediavilla, E., Falco, E., & Muñoz, J. A. 2012, *ApJ*, 755, 82
- Motta, V., Mediavilla, E., Muñoz, J. A., et al. 2002, *ApJ*, 574, 719
- Motta, V., Mediavilla, E., Rojas, K., et al. 2017, *ApJ*, 835, 132
- Moustakas, L. A. & Metcalf, R. B. 2003, *MNRAS*, 339, 607
- Muñoz, J. A., Vives-Arias, H., Mosquera, A. M., et al. 2016, *ApJ*, 817, 155
- Nadler, E. O., Birrer, S., Gilman, D., et al. 2021, *ApJ*, 917, 7
- Narayan, R. & Bartelmann, M. 1996, arXiv e-prints, astro
- Nemiroff, R. J. 1988, *ApJ*, 335, 593
- Netzer, H. 2015, *ARA&A*, 53, 365
- Netzer, H. & Peterson, B. M. 1997, in *Astrophysics and Space Science Library*, Vol. 218, *Astronomical Time Series*, ed. D. Maoz, A. Sternberg, & E. M. Leibowitz, 85
- Netzer, H. & Trakhtenbrot, B. 2007, *ApJ*, 654, 754
- Nierenberg, A. M., Gilman, D., Treu, T., et al. 2020, *MNRAS*, 492, 5314
- Nightingale, J. W., Dye, S., & Massey, R. J. 2018, *MNRAS*, 478, 4738
- O'Dowd, M., Bate, N. F., Webster, R. L., Wayth, R., & Labrie, K. 2011, *MNRAS*, 415, 1985
- Oguri, M., Inada, N., Castander, F. J., et al. 2004, *PASJ*, 56, 399
- Oguri, M., Inada, N., Clocchiatti, A., et al. 2008a, *AJ*, 135, 520
- Oguri, M., Inada, N., Strauss, M. A., et al. 2008b, *AJ*, 135, 512
- Oguri, M., Taruya, A., Suto, Y., & Turner, E. L. 2002, *ApJ*, 568, 488
- Oknyanskij, V. L. & Horne, K. 2001, in *Astronomical Society of the Pacific Conference Series*, Vol. 224, *Probing the Physics of Active Galactic Nuclei*, ed. B. M. Peterson, R. W. Pogge, & R. S. Polidan, 149
- Onken, C. A., Valluri, M., Peterson, B. M., et al. 2007, *ApJ*, 670, 105
- Osterbrock, D. E. 1977, *ApJ*, 215, 733
-

- Ostrowski, F., McMahon, R. G., Connolly, A. J., et al. 2017, *MNRAS*, 465, 4325
- Paic, E., Vernardos, G., Sluse, D., et al. 2022, *A&A*, 659, A21
- Paraficz, D., Hjorth, J., & Elíasdóttir, Á. 2009, *A&A*, 499, 395
- Park, D., Kelly, B. C., Woo, J.-H., & Treu, T. 2012, *ApJS*, 203, 6
- Park, D., Woo, J.-H., Bennert, V. N., et al. 2015, *ApJ*, 799, 164
- Park, D., Woo, J.-H., Denney, K. D., & Shin, J. 2013, *ApJ*, 770, 87
- Peebles, P. J. E. 1993, *Principles of Physical Cosmology*
- Peng, C. Y., Impey, C. D., Ho, L. C., Barton, E. J., & Rix, H.-W. 2006a, *ApJ*, 640, 114
- Peng, C. Y., Impey, C. D., Rix, H.-W., et al. 2006b, *ApJ*, 649, 616
- Perlick, V. 2000, *Ray Optics, Fermat's Principle, and Applications to General Relativity*, Vol. 61
- Peterson, B. M. 1993, *PASP*, 105, 247
- Peterson, B. M. 2001, in *Advanced Lectures on the Starburst-AGN*, ed. I. Aretxaga, D. Kunth, & R. Mújica, 3
- Peterson, B. M. 2010, in *Co-Evolution of Central Black Holes and Galaxies*, ed. B. M. Peterson, R. S. Somerville, & T. Storchi-Bergmann, Vol. 267, 151–160
- Peterson, B. M. 2014, *Space Sci. Rev.*, 183, 253
- Peterson, B. M., Ferrarese, L., Gilbert, K. M., et al. 2004, *ApJ*, 613, 682
- Petters, A. O., Levine, H., & Wambsganss, J. 2001, *Singularity theory and gravitational lensing*
- Plotkin, R. M., Shemmer, O., Trakhtenbrot, B., et al. 2015, *ApJ*, 805, 123
- Pooley, D., Blackburne, J. A., Rappaport, S., & Schechter, P. L. 2007, *ApJ*, 661, 19
- Pooley, D., Rappaport, S., Blackburne, J., et al. 2009, *ApJ*, 697, 1892
- Popović, L. Č. & Chartas, G. 2005, *MNRAS*, 357, 135
- Popović, L. Č., Jovanović, P., Mediavilla, E., et al. 2006, *ApJ*, 637, 620
-

- Popović, L. Č., Mediavilla, E. G., Jovanović, P., & Muñoz, J. A. 2003, *A&A*, 398, 975
- Popović, L. Č., Mediavilla, E. G., & Muñoz, J. A. 2001, *A&A*, 378, 295
- Rees, M. J. 1984, *ARA&A*, 22, 471
- Refsdal, S. 1964, *MNRAS*, 128, 307
- Refsdal, S. & Surdej, J. 1994, *Reports on Progress in Physics*, 57, 117
- Renzini, A. 1999, in *The Formation of Galactic Bulges*, ed. C. M. Carollo, H. C. Ferguson, & R. F. G. Wyse, 9
- Richards, G. T., Keeton, C. R., Pindor, B., et al. 2004a, *ApJ*, 610, 679
- Richards, G. T., Keeton, C. R., Pindor, B., et al. 2004b, *ApJ*, 610, 679
- Richards, G. T., Kruczek, N. E., Gallagher, S. C., et al. 2011, *AJ*, 141, 167
- Richstone, D., Ajhar, E. A., Bender, R., et al. 1998, *Nature*, 385, A14
- Rojas, K., Motta, V., Mediavilla, E., et al. 2014, *ApJ*, 797, 61
- Rojas, K., Motta, V., Mediavilla, E., et al. 2020, *ApJ*, 890, 3
- Rusu, C. E., Oguri, M., Minowa, Y., et al. 2016, *MNRAS*, 458, 2
- Rusu, C. E., Wong, K. C., Bonvin, V., et al. 2020, *MNRAS*, 498, 1440
- Sahu, N., Graham, A. W., & Davis, B. L. 2019, *ApJ*, 876, 155
- Salpeter, E. E. 1964, *ApJ*, 140, 796
- Saturni, F. G., Trevese, D., Vagnetti, F., Perna, M., & Dadina, M. 2016, *A&A*, 587, A43
- Savić, D., Goosmann, R., Popović, L. Č., Marin, F., & Afanasiev, V. L. 2018, *A&A*, 614, A120
- Schechter, P. L., Bailyn, C. D., Barr, R., et al. 1997, *ApJ*, 475, L85
- Schechter, P. L., Morgan, N. D., Chohade, B., et al. 2017, *AJ*, 153, 219
- Schmidt, M. 1963, *Nature*, 197, 1040
- Schneider, P. 2006, *Extragalactic Astronomy and Cosmology*
-

- Schneider, P., Ehlers, J., & Falco, E. E. 1992, *Gravitational Lenses*
- Schneider, P. & Wambsganss, J. 1990, *A&A*, 237, 42
- Schneider, P. & Weiss, A. 1987, *A&A*, 171, 49
- Schulze, A. & Wisotzki, L. 2010, *A&A*, 516, A87
- Seifert, W., Appenzeller, I., Baumeister, H., et al. 2003, in *Society of Photo-Optical Instrumentation Engineers (SPIE) Conference Series*, Vol. 4841, Proc. SPIE, ed. M. Iye & A. F. M. Moorwood, 962–973
- Sergeev, S. G., Doroshenko, V. T., Golubinskiy, Y. V., Merkulova, N. I., & Sergeeva, E. A. 2005, *ApJ*, 622, 129
- Seyfert, C. K. 1943, *ApJ*, 97, 28
- Shajib, A. J., Birrer, S., Treu, T., et al. 2020, *MNRAS*, 494, 6072
- Shajib, A. J., Birrer, S., Treu, T., et al. 2019, *MNRAS*, 483, 5649
- Shakura, N. I. & Sunyaev, R. A. 1973, *A&A*, 500, 33
- Shang, Z., Wills, B. J., Wills, D., & Brotherton, M. S. 2007, *AJ*, 134, 294
- Shapiro, I. I. 1964, *Phys. Rev. Lett.*, 13, 789
- Shen, Y. 2013, *Bulletin of the Astronomical Society of India*, 41, 61
- Shen, Y., Brandt, W. N., Richards, G. T., et al. 2016, *ApJ*, 831, 7
- Shen, Y., Greene, J. E., Strauss, M. A., Richards, G. T., & Schneider, D. P. 2008, *ApJ*, 680, 169
- Shen, Y., Grier, C. J., Horne, K., et al. 2019, *ApJ*, 883, L14
- Shen, Y. & Liu, X. 2012, *ApJ*, 753, 125
- Shen, Y., Richards, G. T., Strauss, M. A., et al. 2011, *ApJS*, 194, 45
- Shields, G. A. 1978, *Nature*, 272, 706
- Silk, J. & Rees, M. J. 1998, *A&A*, 331, L1
- Simić, S. & Popović, L. Č. 2014, *Advances in Space Research*, 54, 1439
-

- Sluse, D., Claeskens, J. F., Hutsemékers, D., & Surdej, J. 2007, *A&A*, 468, 885
- Sluse, D., Hutsemékers, D., Anguita, T., Braibant, L., & Riaud, P. 2015, *A&A*, 582, A109
- Sluse, D., Hutsemékers, D., Courbin, F., Meylan, G., & Wambsganss, J. 2012, *A&A*, 544, A62
- Sluse, D., Rusu, C. E., Fassnacht, C. D., et al. 2019, *MNRAS*, 490, 613
- Sluse, D., Schmidt, R., Courbin, F., et al. 2011, *A&A*, 528, A100
- Sluse, D. & Tewes, M. 2014, *A&A*, 571, A60
- Smette, A., Sana, H., Noll, S., et al. 2015, *A&A*, 576, A77
- Sou, H., Wang, J.-X., Xie, Z.-L., Kang, W.-Y., & Cai, Z.-Y. 2022, *MNRAS*[arXiv]2203.07119
- Spilker, J. S., Marrone, D. P., Aravena, M., et al. 2016, *ApJ*, 826, 112
- Spiniello, C., Agnello, A., Sergeev, A. V., et al. 2019, *MNRAS*, 483, 3888
- Sturm, E., González-Alfonso, E., Veilleux, S., et al. 2011, *ApJ*, 733, L16
- Suganuma, M., Yoshii, Y., Kobayashi, Y., et al. 2006, *ApJ*, 639, 46
- Sulentic, J. W., Marziani, P., & Dultzin-Hacyan, D. 2000, *ARA&A*, 38, 521
- Suyu, S. H., Bonvin, V., Courbin, F., et al. 2017, *MNRAS*, 468, 2590
- Suyu, S. H., Chang, T.-C., Courbin, F., & Okumura, T. 2018, *Space Sci. Rev.*, 214, 91
- Suyu, S. H. & Halkola, A. 2010, *A&A*, 524, A94
- Suyu, S. H., Hensel, S. W., McKean, J. P., et al. 2012, *ApJ*, 750, 10
- Tessore, N., Bellagamba, F., & Metcalf, R. B. 2016, *MNRAS*, 463, 3115
- Tewes, M., Courbin, F., Meylan, G., et al. 2013, *A&A*, 556, A22
- Trakhtenbrot, B. & Netzer, H. 2012, *MNRAS*, 427, 3081
- Tremaine, S., Gebhardt, K., Bender, R., et al. 2002, *ApJ*, 574, 740
- Treu, T. 2010, *ARA&A*, 48, 87
-

- Treu, T., Agnello, A., Baumer, M. A., et al. 2018, MNRAS, 481, 1041
- Treu, T., Agnello, A., & Strides Team. 2015, in American Astronomical Society Meeting Abstracts, Vol. 225, American Astronomical Society Meeting Abstracts #225, 318.04
- Treu, T., Marshall, P. J., Cyr-Racine, F. Y., et al. 2013, arXiv e-prints, arXiv:1306.1272
- Treu, T., Woo, J.-H., Malkan, M. A., & Blandford, R. D. 2007, ApJ, 667, 117
- Trevese, D., Stirpe, G., Vagnetti, F., Zitelli, V., & Paris, D. 2006, in Astronomical Society of the Pacific Conference Series, Vol. 360, AGN Variability from X-Rays to Radio Waves, ed. C. M. Gaskell, I. M. McHardy, B. M. Peterson, & S. G. Sergeev, 201
- Ueda, Y., Akiyama, M., Ohta, K., & Miyaji, T. 2003, ApJ, 598, 886
- Urry, C. 2004, in Astronomical Society of the Pacific Conference Series, Vol. 311, AGN Physics with the Sloan Digital Sky Survey, ed. G. T. Richards & P. B. Hall, 49
- Urry, C. M. & Padovani, P. 1995, PASP, 107, 803
- Vacca, W. D., Cushing, M. C., & Rayner, J. T. 2003, PASP, 115, 389
- Vanden Berk, D. E., Richards, G. T., Bauer, A., et al. 2001, AJ, 122, 549
- Vanden Berk, D. E., Wilhite, B. C., Kron, R. G., et al. 2004, ApJ, 601, 692
- Vernet, J., Dekker, H., D'Odorico, S., et al. 2011, A&A, 536, A105
- Vestergaard, M. 2002, ApJ, 571, 733
- Vestergaard, M. 2004, ApJ, 601, 676
- Vestergaard, M. & Osmer, P. S. 2009, ApJ, 699, 800
- Vestergaard, M. & Peterson, B. M. 2006a, ApJ, 641, 689
- Vestergaard, M. & Peterson, B. M. 2006b, ApJ, 641, 689
- Volonteri, M. & Rees, M. J. 2005, ApJ, 633, 624
- Walsh, D., Carswell, R. F., & Weymann, R. J. 1979, Nature, 279, 381
- Wambsganss, J. 1998, Living Reviews in Relativity, 1, 12
-

- Wambsganss, J. 2006, in Saas-Fee Advanced Course 33: Gravitational Lensing: Strong, Weak and Micro, ed. G. Meylan, P. Jetzer, P. North, P. Schneider, C. S. Kochanek, & J. Wambsganss, 453–540
- Wambsganss, J., Bode, P., & Ostriker, J. P. 2004, *ApJ*, 606, L93
- Wambsganss, J. & Paczynski, B. 1991, *AJ*, 102, 864
- Wambsganss, J., Paczynski, B., & Schneider, P. 1990, *ApJ*, 358, L33
- Wandel, A., Peterson, B. M., & Malkan, M. A. 1999, *ApJ*, 526, 579
- Wayth, R. B., O’Dowd, M., & Webster, R. L. 2005, *MNRAS*, 359, 561
- Welsh, W., Robinson, E. L., Hill, G., et al. 2000, in American Astronomical Society Meeting Abstracts, Vol. 197, American Astronomical Society Meeting Abstracts, 39.13
- Weymann, R. J., Latham, D., Angel, J. R. P., et al. 1980, *Nature*, 285, 641
- Wilson, J. C., Henderson, C. P., Herter, T. L., et al. 2004, in Society of Photo-Optical Instrumentation Engineers (SPIE) Conference Series, Vol. 5492, Ground-based Instrumentation for Astronomy, ed. A. F. M. Moorwood & M. Iye, 1295–1305
- Woo, J.-H., Le, H. A. N., Karouzos, M., et al. 2018, *ApJ*, 859, 138
- Woo, J.-H., Schulze, A., Park, D., et al. 2013, *ApJ*, 772, 49
- Woo, J.-H., Treu, T., Barth, A. J., et al. 2010, *ApJ*, 716, 269
- Woo, J.-H., Treu, T., Malkan, M. A., & Blandford, R. D. 2008, *ApJ*, 681, 925
- Woo, J.-H., Yoon, Y., Park, S., Park, D., & Kim, S. C. 2015, *ApJ*, 801, 38
- Wright, E. L., Eisenhardt, P. R. M., Mainzer, A. K., et al. 2010, *AJ*, 140, 1868
- Xiao, T., Barth, A. J., Greene, J. E., et al. 2011, *ApJ*, 739, 28
- Yonehara, A., Hirashita, H., & Richter, P. 2008, *A&A*, 478, 95
- Yong, S. Y., King, A. L., Webster, R. L., et al. 2018, *MNRAS*, 479, 4153
- Zakamska, N. L., Hamann, F., Pâris, I., et al. 2016, *MNRAS*, 459, 3144
- Zalesky, L. & Ebeling, H. 2020, *MNRAS*, 498, 1121
- Zu, Y., Kochanek, C. S., & Peterson, B. M. 2011, *ApJ*, 735, 80
-